國 立 交 通 大 學

應 用 化 學 系

博 士 論 文

分子束多原子分子之紫外光光電子影像

Vacuum ultraviolet photoelectron imaging of polyatomic molecules in supersonic molecular beams

研 究 生：廖雪兒

指導教授：李遠鵬　教授

鈴木俊法　　教授

中 華 民 國 一 百 年 二 月

分子束多原子分子之紫外光光電子影像

Vacuum ultraviolet photoelectron imaging of polyatomic molecules in supersonic molecular beams

研 究 生：廖雪兒　　Student：Suet-Yi Liu

指導教授：李遠鵬博士　　Advisor：Yuan-Pern Lee

鈴木俊法博士　　Toshinori Suzuki

國 立 交 通 大 學

應 用 化 學 系

博 士 論 文

A Thesis

Submitted to Department of Applied Chemistry

College of Science

National Chiao-Tung University

in partial Fulfillment of the Requirements

for the Degree of Ph.D.

in

Applied Chemistry

February 2011

Hsinchu, Taiwan, Republic of China

中華民國一百年二月

Abstract

I have constructed a He(I) ultraviolet photoelectron spectrometer using a supersonic molecular beam and a two-dimensional position-sensitive detector of photoelectrons. The photoelectron imaging (PEI) spectrometer enabled measurements of photoelectron spectra and photoelectron angular distributions with an efficiency considerably higher than a conventional spectrometer using a hemispherical energy analyzer. The most crucial factor for this achievement was to overcome high susceptibility of PEI to background electrons generated by scattered He(I) radiation. I examined various designs of electrodes experimentally and computationally and identified the main source of the background photoemission as the repeller plate used for acceleration of electrons. I designed a new electrostatic lens that intercepts background photoelectrons from the repeller plate traveling toward the imaging detector. High energy resolution ($\Delta E/E$) of 0.735 % was achieved at E = 5.461 eV with He(I) radiation that has rather poor beam characteristics. The photoelectron angular anisotropies as a function of photoelectron kinetic energies are presented for jet-cooled benzene and pyridine.

The PEI spectrometer was also employed in photoionization experiments using a vacuum ultraviolet free electron laser (VUV-FEL) at SPring-8 in Japan as a light source. A time-resolved photoelectron imaging using a femtosecond ultraviolet (UV) laser as a pump pulse and the VUV-FEL as a probe pulse is presented. Ultrafast internal conversion and intersystem crossing in pyrazine in a supersonic molecular beam were clearly observed. The VUV radiation allowed us to observe the entire Franck-Condon envelope in photoionization from a transient electronic state, which was not possible in UV-DUV experiment in the laboratory.

謝誌

終於畢業了。回想十年前還在念大一的我，當時還在怕連大學也畢不了業，真沒想到今天竟然博班畢業了。從小城市的澳門跑到台灣念書，在這裡生活了七年多，從剛開始的膽膽驚驚，到現在已經把這裡當作我第二個家了。老實說，雖然在澳門念了十幾年書，但對尋求知識的態度，真的是在台灣的時候才學會。很感謝我的指導教授李遠鵬老師，他的物化課讓我開竅，也讓我從拾讀書的信心。他的實驗室也提供了最好的儀器設備以及學習環境，讓我可以打穩基礎。還有他細心的指導，訓練我的邏輯思考。更感謝他讓我在日本學習三年，讓我有機會廣闊自己的視野。另外，也要感謝口試委員王念夏老師，林志民老師和李英裕老師對論文的指導和鼓勵。

在大學跟研究生的生涯裡，很感謝實驗室的學長姊們在我實驗上的教導，有 cool cool 的鐘昭宇學長，文靜的劉靜漪學姊，親和力十足的佳燕學姊，做事很有效率的呂志偉學長，帥氣跟智慧並重，人見人愛車見車載的朱小花教授，理論計算顧問吳宇中學長，外冷內熱的陳慧芬學姊，喜歡幫人的楊勝凱學長，以及跟我一起常熬夜的 Mo Mo 等等。另外，也要感謝秘書莊媽一直以來的照顧。還要感謝實驗室裡活力十足的學弟妹跟伙伴們：愛帥愛吵愛冷笑話，但又親切又好玩的鄭大頭，好玩好笑好可愛的郁旋，傻傻的俞範，還有韓慧玲，傅龍，洋洋，姚姚，黃上臻，陳勁達，書毓，建亨等等。有你們的陪伴，讓我在實驗室每天都過得很開心。

另外也要感謝鈴木俊法老師，他在研究上給予我十足的自由度跟資源，讓我很放心的實行自己在實驗上的想法，也陪養了我的獨立思考能力。還有實驗室裡的每一位優秀的博後研究員：Kohguchi-san, Nishizawa-san, Fuji-san, Ohshimo-san, Ogi-san, Horio-san, Mizuno-san, Tang-san, Niu-san, Pei-san, Zuo-san，很感謝你們每一位在我實驗上的協助跟指導，每天午餐時段的閒聊，舒緩了我不少壓力。還有秘書 Matsumoto-san 熱心的幫忙，幫我解決了不少生活上的麻煩。在日本這三年，我體會很深，真真正正地感受到獨立生活的孤獨，還有語言不通的麻煩。不過，與此同時，這些日子也讓我成長

不少，讓我更有信心去迎接以後的挑戰。另外，很想感謝一個日本朋友，**Hosonuma-sensei**，她的熱情招待，每次都讓我很窩心，同時她也讓我接觸到很多日本的文化跟食物。

最後，要感謝我的家人無限量的支持和男朋友無限次的體諒，讓我可以無顧慮地完成我的學業。我以此論文獻給我所有親愛的親友們。

Table of contents

Chapter 3. Designing a PEI spectrometer for He(I) light source

Chapter 4. He(I) photoelectron imaging of benzene and pyridine

List of Figures

List of Tables

Chapter 1

Introduction

1.1 Ultraviolet Photoelectron Spectroscopy (UPS)

Photoelectron spectroscopy is based on Einstein's photoelectric effect.[1] When the energy of a photon (hν) exceeds the binding energy of an electron in a molecule (M), the electron will be ejected.

$$M + h\nu \rightarrow M^+ (E_{int}) + e^- \quad (1\text{-}1)$$

in which $M^+(E_{int})$ is the molecular ion with internal energy E_{int} which includes the electronic, vibrational and rotational energy. Since the mass of an electron is less than one thousandth that of the molecule, the electron carries essentially all the recoil kinetic energy between the ion and the electron. Therefore the kinetic energy of the photoelectron (PKE) is given by

$$PKE = h\nu - eBEa - E_{int} \quad (1\text{-}2)$$

where eBEa is the adiabatic electron binding energy. According to Koopmans' theorem[2], the electron binding energy is equal to the orbital energy. Thus, the photoelectron spectrum of a molecule is directly related to the molecular orbital energies within the approximation of the Koopmans' theorem.

The experimentally observed PKE distribution is called a photoelectron spectrum. For a given photon energy, various PKE are possible, since E_{int} generally has a distribution. The shape of each band, so-called the Franck-Condon envelope, provides valuable information to assign each band to a molecular orbital from which ionization occurs.[3] Let us take N_2 molecule as an example. The photoelectron spectrum of N_2 using He(I) radiation (21.22 eV) exhibits the features of ionization to three electronic states, $X^2\Sigma_g^+$, $A^2\Pi_u$ and $B^2\Sigma_u^+$, which

correspond to the ionization occurs from σ_g, π_u and σ_u molecular orbitals, respectively, as shown in Fig. 1.1. These three progressions exhibit vibrational structures with different frequencies. The vibrational frequency represents the strengths of the N–N bond in each electronic state of N_2^+. If a bonding electron is removed, the force constant of the ion becomes smaller, so that the vibrational frequency decreases. Therefore, the first band in the photoelectron spectrum of N_2 corresponds to a removal of nonbonding (weakly bonding) electron, because the vibrational frequency decreases slightly from 2345 cm^{-1} in the ground state of N_2 to 2150 cm^{-1}. Similarly, the second band corresponds to a removal of bonding electron, because the vibrational frequency decreases drastically from 2345 to 1810 cm^{-1}, and the third band corresponds to a removal of nonbonding electron (weakly anti-bonding) because the vibrational frequency due to this band increases slightly from 2345 to 2390 cm^{-1}. This criterion of the change in vibrational frequency can be applied to assign the ionized orbitals to nonbonding, bonding, and anti-bonding character, respectively. The Franck-Condon factor is given by,

$$q_{\upsilon\upsilon''} = |\int \psi_\upsilon \psi_{\upsilon''} d\tau|^2 \qquad (1\text{-}3)$$

which is the square of the overlap integral of vibrational wavefunctions between the neutral ground-state and the ion. In the photoelectron spectrum of nitrogen, the $A^2\Pi_u$ state shows a long vibrational progression while the $X^2\Sigma_g^+$ state and $B^2\Sigma_u^+$ state shows-intense origin bands. It implies that the π_u^{-1} state has a different equilibrium N-N bond length, while those of the σ_g^{-1} and σ_u^{-1} states are similar to that in the neutral ground state.

The lowest atomic and molecular orbital that can be probed with PES depends on the photon energy, as shown in Fig. 1.2. In general, ultraviolet radiation sources (with photon energy of 10–45 eV) are used to ionize electrons from the valence molecular orbitals that mainly constitute the chemical bonds, while X-ray sources (with photon energy of 200–2000 eV) are used for probing core electrons that are characteristic of the element, and chemical environment. In this thesis, I discuss ultraviolet photoelectron spectroscopy (UPS).

1.2 The Angular Distribution of Photoelectrons

Upon photoionization, the photoelectrons are not emitted equally in all directions, and their angular distributions vary when different ionic states are produced. For one photon ionization with polarized light, the photoelectron angular distribution (PAD) expected for randomly oriented atoms or molecules can be expressed by

$$I(\theta) = \frac{\sigma}{4\pi}\left[1 + \frac{\beta}{2}\left(3\cos^2\theta - 1\right)\right] \tag{1-4}$$

where σ is the total cross-section, and θ is the angle between the direction of the ejected electron and the polarization of the incident light. β is the asymmetry parameter, of which value in photoionization of an atom is given by the Cooper-Zare formula,[4]

$$\beta = \frac{l(l-1)r_{l-1}^2 + (l+1)(l+2)r_{l+1}^2 - 6l(l+1)r_{l+1}r_{l-1}\cos(\delta_{l+1} - \delta_{l-1})}{3(2l+1)\left[lr_{l-1}^2 + (l+1)r_{l+1}^2\right]} \tag{1-5}$$

where l is the orbital angular momentum of the electron before ionization, $r_{l\pm1}$ are the transition dipole matrix elements for the $l\pm1$ components of outgoing photoelectron wavefunctions, and $\delta_{l\pm1}$ denote the phases of these waves. Here β ranges from +2 ($\cos^2\theta$ distribution) to -1 ($\sin^2\theta$ distribution). For the ionization of an *s*-type electron from an atom, as in H^-, the outgoing electron wave must be a *p* wave (recall the $\Delta l = \pm1$ selection rule for an electronic transition in a hydrogen atom). Since $l = 0$ for an *s* electron, equation (1-5) yields $\beta = 2$. On the other hand, ionization from a *p* orbital creates both *s* and *d* outgoing waves that interfere with each other; therefore, the magnitude of β becomes small.

For unpolarized light, the general expression of PAD can be derived from equation (1-4). Samson and Starace[5] showed the expression of PAD for partially polarized light,

$$I(\theta) = \frac{I_x}{I_0}\frac{\sigma}{4\pi}\left[1 + \frac{\beta}{2}\left(3\cos^2\theta_x - 1\right)\right] + \frac{I_y}{I_0}\frac{\sigma}{4\pi}\left[1 + \frac{\beta}{2}\left(3\cos^2\theta_y - 1\right)\right] \tag{1-6}$$

where (I_x/I_0) and (I_y/I_0) describe the fraction of light intensity polarized along the x and y axis ($I_x + I_y = I_0$). The definitions of x, y and z axis are shown in Fig. 1.3. We define the polarization of the incident light beam as

$$p \equiv \frac{I_y - I_x}{I_x + I_y} \tag{1-7}$$

By using the geometric relation

$$cos^2\theta_x + cos^2\theta_y + cos^2\theta_z = 1 \tag{1-8}$$

the equation (1-6) can be rewritten as

$$I(\theta) = \frac{\sigma}{4\pi}\left\{1 - \frac{\beta}{4}\left[(3\cos^2\theta_z - 1) - 3p\left(\cos^2\theta_y - \cos^2\theta_x\right)\right]\right\} \tag{1-9}$$

For unpolarized light, p = 0, then

$$I(\theta_z) = \frac{\sigma}{4\pi}\left[1 + \frac{\beta}{2}\left(\frac{3}{2}sin^2\theta_z - 1\right)\right] \tag{1-10}$$

Therefore, for unpolarized light, the angle θ_z is measured from the propagation direction, rather than the polarization direction.

1.3 Conventional Ultraviolet Photoelectron Spectroscopy

Since the pioneering works by Vilesov *et al.*[6] and Tuner *et al.*[7] nearly 50 years ago, ultraviolet photoelectron spectroscopy (UPS) has been playing a central role in experimental studies of the electronic structures of molecules.

The most widely used light source in UPS is a discharge lamp using pure helium, which gives the He(I) resonance line at 58.4 nm (21.22 eV) or the He(II) resonance line at 30.38 nm (40.81 eV). This light source provided an intense and nearly monoenergetic line with high photon energy, allowing ionization from most or all valence orbitals. The gas discharge lamps may be operated with gases other than helium to produce lower photon energies. Some resonance lines are given in Table 1.1. Another useful continuum VUV source for PES is synchrotron radiation that produces a continuum radiation from VUV to X-ray with almost 100 % polarization. The intensity of synchrotron radiation can easily reach 10^{11} photons per second per Angstrom. However, it is a large-scale facility and is not readily accessible,

therefore it cannot be used as conveniently as the discharge lamp in the laboratory.

When a pulsed laser is used in PES, the time-of-flight (TOF) method is advantageous for the analysis of electron kinetic energy owing to its inherent multiplex detection capability of the electrons. Furthermore, magnetic bottle TOF spectrometer developed by Kruit and Read[8] improved significantly the collection efficiency in a standard TOF method. They utilized a diverging magnetic field to collect photoelectrons produced in a small photoionization volume and guide the electrons into a flight tube for TOF analysis. With this method a 50 % collection efficiency (acceptance angle 2π sr) of the photoelectrons was achieved. However, the drawback is that this method provides no angular resolution and it cannot be coupled with a continuous light source. In PES with a continuous light source, a hemispherical energy analyzer has been widely used to measure electron energies. This spectrometer consists of two concentric hemispheres of radius R_1 (inner hemisphere) and R_2 (outer hemisphere), as shown in Fig. 1.4. Potentials $-V_1$ and $-V_2$ are applied to the inner and outer hemispheres, respectively, with V_2 greater than V_1. The potential difference between the hemispheres defines the median equipotential surface (V_o). The electrons entering through the entrance slit with the kinetic energy $E = eV_o$ will follow the trajectory along this median equipotential surface and will be focused at the exit slit. When the electrons travel too fast, they will impinge on the outer hemisphere. In contrast, if their kinetic energy is too low, they will be attracted to the inner hemisphere. Thus only electrons of a very narrow energy region will pass through the analyzer to the detector. UPS with a high-performance hemispherical electron energy analyzer and an intense He(I) lamp using the electron cyclotron resonance has achieved a high spectral resolution of 5 meV that is limited mainly by the linewidth of the He(I) radiation.[9] For the analysis of photoelectron angular distribution (PAD), the electron signals are measured at different angles by moving either the analyzer or the light beam. The main limitation with a hemispherical analyzer is its poor collection efficiency (< 1 %) of electrons due to its small acceptance solid angle. Therefore, most ultraviolet photoelectron spectra so far have been

measured at room temperature.

1.4 Analysis of Unresolved Band

Photoelectron spectrum of polyatomic molecules typically exhibit overlapping bands of which spectral assignments are difficult. One reason for the band overlap is that most polyatomic molecules possess several electronic orbitals that are nearly degenerate in energy. Another reason is that, at room temperature, occurrence of hot bands of low-frequency vibrations made the spectra highly congested. Supersonic beam technique is a useful tool to cool down the gaseous sample and simplify the spectrum. Shirley *et al*. employed molecular beam photoelectron spectroscopy[10] (MBPES) to resolve the vibrational structure of small molecules and applied it to molecules such as ethylene (C_2H_4),[10] carbon disulfide (CS_2),[11] methyl chloride (CH_2Cl_2),[12] ketene (C_2H_2O).[13] Recently, Oku *et al*.[14] reported He(I) UPS of jet-cooled pyrazine ($C_4H_4N_2$) and demonstrated that the spectrum of jet-cooled samples exhibit much finer structures than those obtained for the vapor at room temperature. So far MBPES has been applied to only a limited number of systems. A major difficulty in MBPES is its low number density (10^{12}–10^{13} cm^{-3}) of molecules in the ionization region as compared with that in a gas cell (10^{14}–10^{15} cm^{-3}). Another experimental problem is that the conventional hemispherical energy analyzer employed by UPS has a poor electron collection efficiency. Consequently the signal has to be integrated for hours to achieve satisfactory signal to noise ratio. The pulsed-field-ionization zero-kinetic-energy photoelectron spectroscopy (PFI-ZEKE-PES)[15,16] provides another experimental method to observe photoelectron spectra of jet-cooled molecules with high resolution (≤ 1 cm^{-1}).[17,18] In PFI-ZEKE-PES, molecules are not directly ionized, but excited to the high-n ($n \geq 150$) Rydberg states just below the ionization threshold. A time-delayed pulsed field is then applied to field-ionize the molecules

and extract the Rydberg electrons. Figure 1.5 shows the schematic drawings of He(I) UPS and PFI-ZEKE. Therefore, PFI-ZEKE observes the resonances of the photon energy with the rovibronic energies of Rydberg states associated with each cation state.[19] It utilizes the fact that a Rydberg state with a high principal quantum number is structurally identical with a cationic state owing to negligible influence on the molecular geometry of the ion core. However, PFI-ZEKE cannot substitute conventional UPS because it encounters difficulties when the Rydberg states rapidly dissociate or autoionize. Oku *et al.*[14] found that the D_1 band is missing in the VUV-PFI-PE measurement of pyrazine, which they ascribed to fast electronic autoionization of high-*n* Rydberg (ZEKE) states from the D_1 ion core to the D_0 continuum.

Another method for disentangling overlapping photoelectron bands is measurements of the photoelectron angular distribution (PAD). Carlson and Anderson[20] performed He(I) UPS of benzene and found that each photoelectron band exhibits characteristic angular anisotropies (β). They used the β values to analyze the overlapping bands in the spectrum. The measurement of the photon-energy dependence of PAD is even more useful for assignments. Piancastelli *et al.*[21] measured the β parameter of a series of nitrogen-containing aromatic systems as a function of photon energy for using synchrotron radiation (SR) to distinguish the nonbonding *n* and π orbital; The assignment in the azabenzenes have not been straightforward with He(I) UPS at a fixed photon energy. Due to a low collection efficiency of hemispherical energy analyzer, it is time-consuming to observe PAD with conventional photoelectron spectrometers. For example, measurement of the angular distribution (40° to 120° in 10° increments) of 1,5-hexadiene in the full spectrum range (9.0 – 20.0 eV) using a hemispherical energy analyzer required three days.[22] Although it is anticipated that PAD can be quantified more easily using SR facility with photon densities higher than a He(I) light source, SR is not readily available in the laboratory. In addition, PES using SR is always performed at moderate resolution in the range of 0.1-0.3 eV, which does not allow for detailed vibrational analysis.

This is because the slit width of monochromator for SR is typically wide in order to achieve reasonable signal intensity.

Both MBPES and PAD are clearly useful in analyzing the unresolved bands in photoelectron spectra. However, conventional MBPES and PAD measurement suffer from a poor electron collection efficiency associated with hemispherical energy analyzer. This difficulty may be overcome by applying the photoelectron imaging (PEI) technique.

1.5 Motivation

The photoion imaging developed by Chandler and Houston,[23] and improved by Eppink and Parker[24] has been extended to photoelectron imaging (PEI). PEI spectrometer provides the ultimate collection efficiency of photoelectrons of 4π steradians and simultaneous measurement of photoelectron kinetic energy distribution (PKED) and photoelectron angular distribution (PAD).[25] It allows use of He(I) UPS to measure PAD routinely for analyzing the spectra of jet-cooled molecules, making PEI-He(I) UPS a more powerful spectroscopic method. Compare with a hemispherical energy analyzer, 2D detector using in PEI is expected to provide lower energy resolution. Nevertheless, with ongoing advances in MCP and CCD camera technology, the resolution of PEI has been improved dramatically. Ogi *et al.*[26] reported a super-resolution imaging system that provides 64 megapixel resolution (8192 × 8192 pixels) and a photoelectron kinetic energy resolution of 0.2 % at 1.696 eV (FWHM: 3.1 meV). One disadvantage of PEI compared with a hemispherical energy analyzer, is its relatively high susceptibility to background photoemission induced by scattered He(I) radiation. Base on a poor characteristic of incoherent He(I) radiation, the PEI apparatus developed for He(I) radiation is certainly applicable to photoelectron spectroscopy with coherent VUV light sources such as a free electron laser and high harmonics produced by

ultrashort pulsed lasers.

We also aim at PEI experiments using a vacuum ultraviolet free electron laser (VUV FEL). VUV FEL is an intense ultrashort laser with photon energy of 20.69–24.83 eV (60–50 nm) which is useful for pump–probe photoelectron spectroscopy to observe ultrafast electronic dynamics and the subsequent photochemical reactions involving ground-state products.[27] Owing to a lasing wavelength of the FEL at SPring-8 in Japan is 50-60 nm that coincides with the He(I) line (58.4 nm), He(I) PEI experiment also serves as a test for photoelectron imaging using VUV FEL.

1.6 Thesis Outline

As far as I know, PEI experiment combined with He(I) radiation presented in this thesis is the first attempt reported so far. The reminder of this dessertation consists of six chapters. Chapter 2 describes the principle of photoelectron imaging and the data analysis. Chapter 3 discusses the design concept and construction of our He(I)-PEI apparatus. Owing to a poor characteristic of He(I) radiation, various modifications were made to velocity mapping spectrometer. Chapter 4 presents the He(I) photoelectron image of benzene and pyridine in supersonic molecular beams to demonstrate the performance of our He(I)-PEI. Chapter 5 describes photoelectron imaging experiments using FEL including one- and two-photon ionization experiments. The time-resolved PEI of using a femtosecond UV laser and a VUV free-electron-laser with our VMI spectrometer is reported. Ultrafast internal conversion and intersystem crossing in pyrazine in a supersonic molecular beam are discussed. Chapter 6 presents a summary of this dissertation and future directions based on my study.

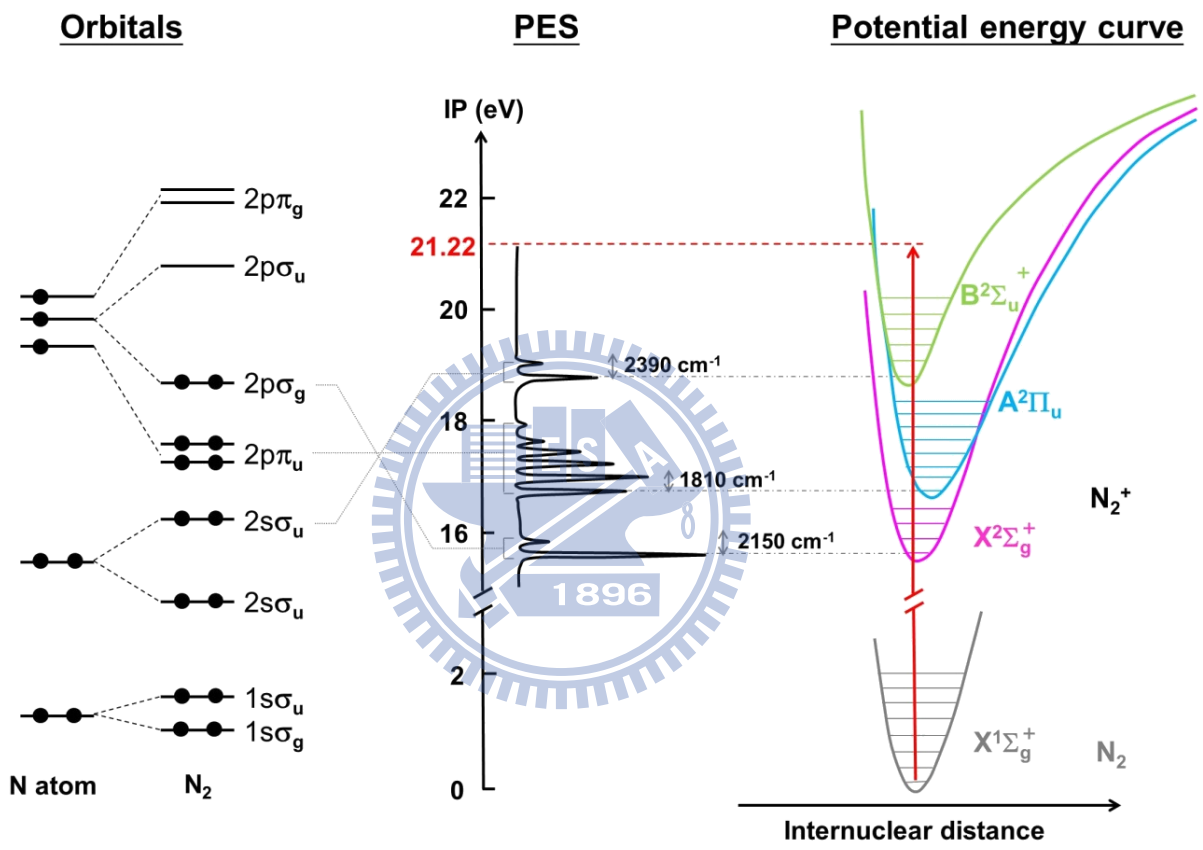

Figure 1.1 The schematic drawing of orbital, photoelectron spectrum and potential energy curve of nitrogen.

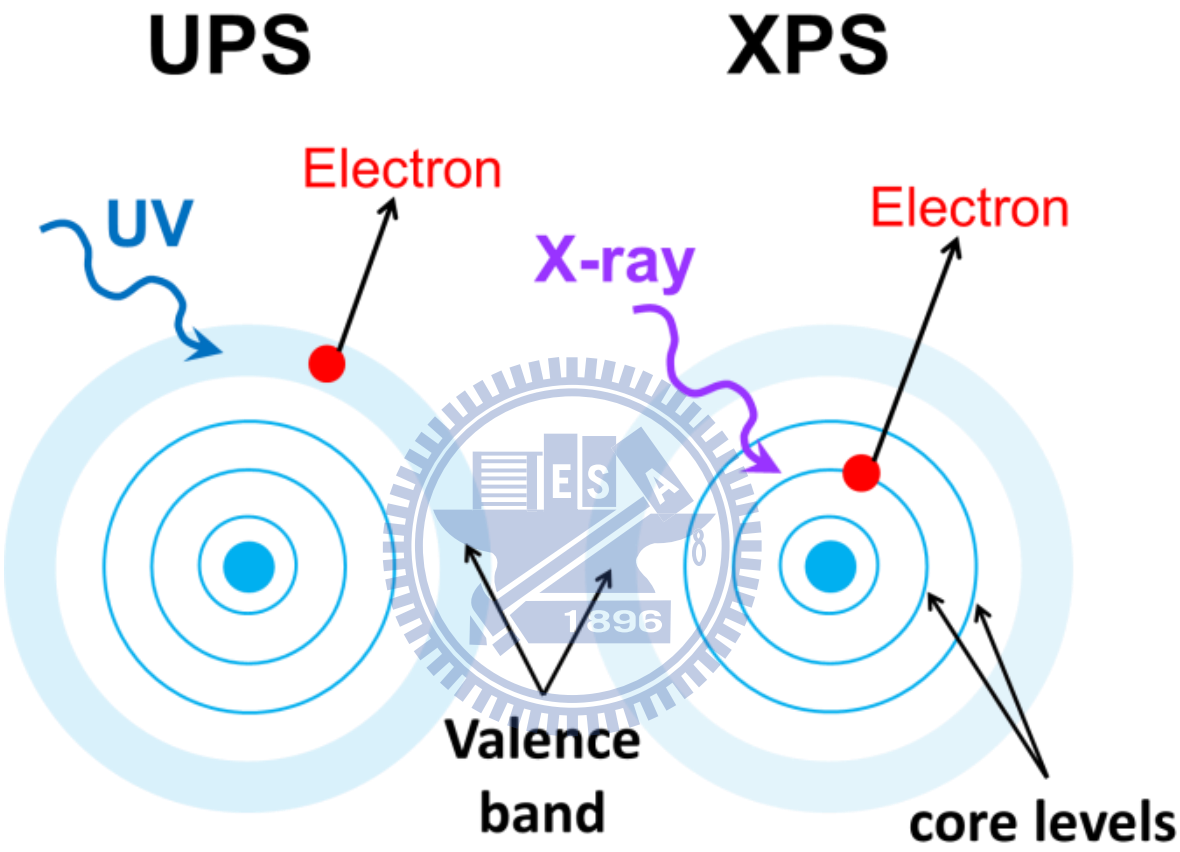

Figure 1.2 Schematic drawing of UPS and XPS.

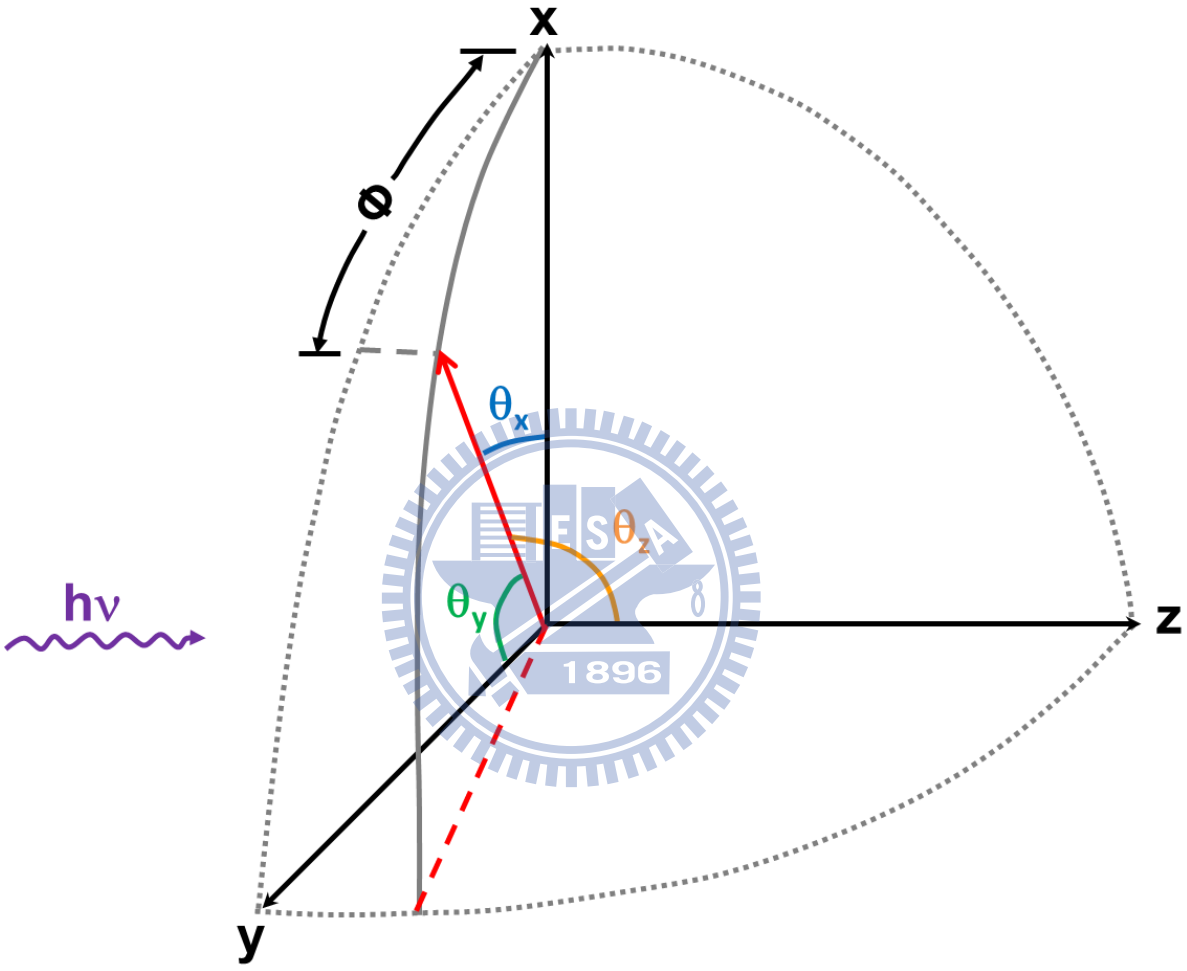

Figure 1.3 Orientation of the photoelectron with respect to the x, y and z axis. The photon hν is incident along the z axis.

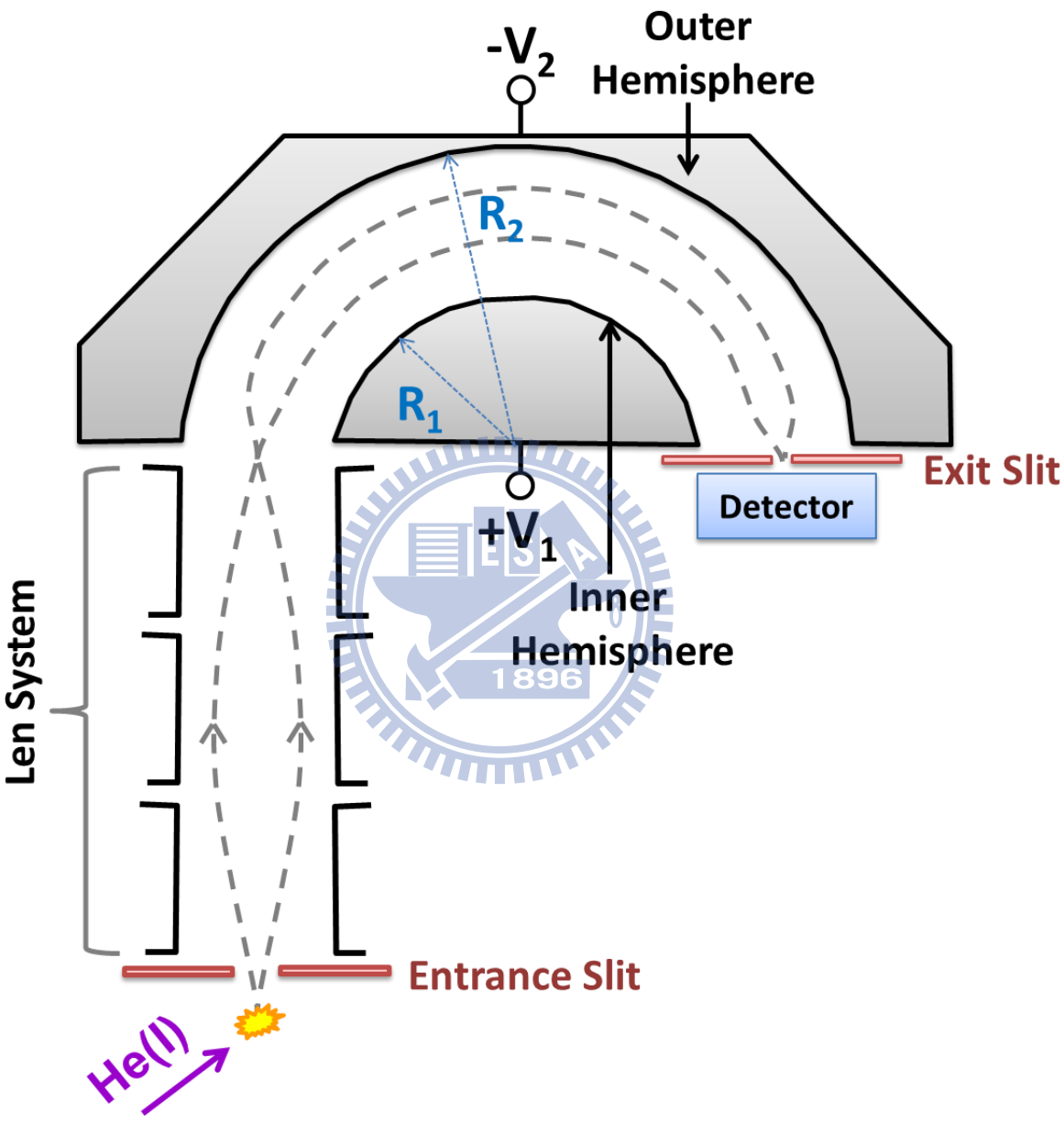

Figure 1.4 Schematic drawing of hemispherical energy analyzer.

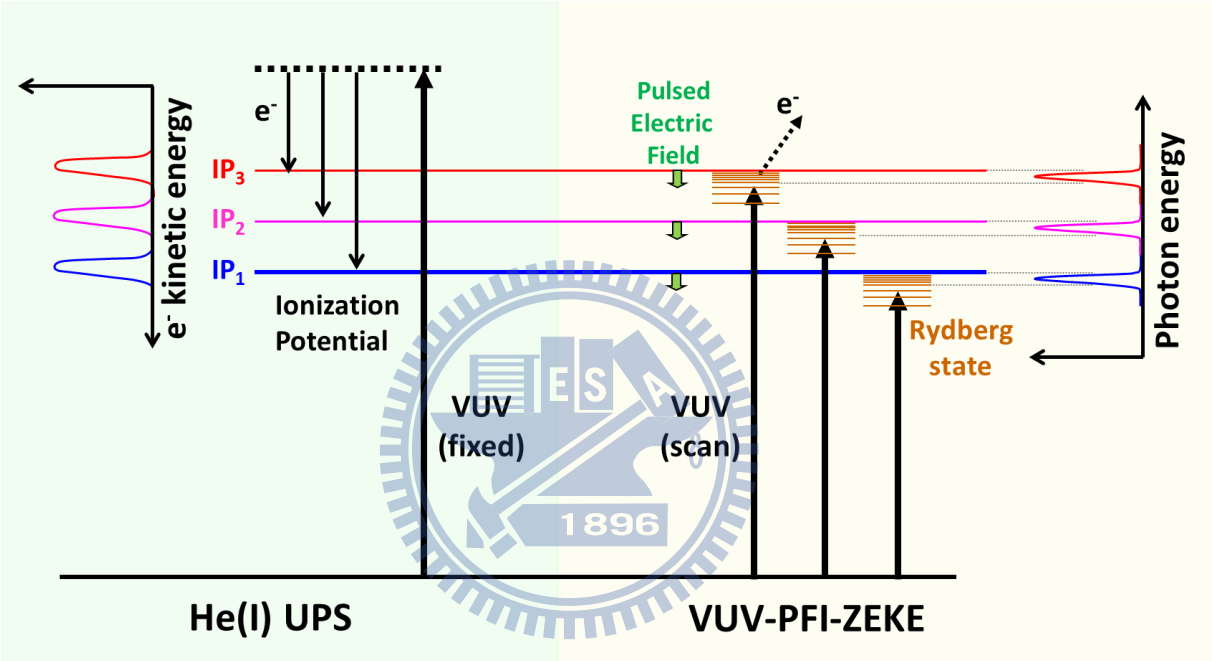

Figure 1.5 The schematic drawing of He(I) UPS using He(I) radiation (21.22 eV) and PFI-ZEKE photoelectron spectroscopy, photoelectrons are detected by a pulsed electric field.

Table 1.1 Lines from discharges in gases other than helium

VUV source	Energy [eV]	Rel. Intensity [%]	Wavelength [nm]	Satellite shift [eV]
H Lyman α	10.20	100	121.57	0
H Lyman β	12.09	10	102.57	2.67
He (I) α	21.22	100	58.43	0
He (I) β	23.09	1.2 … 1.8	53.70	1.87
He (I) γ	23.74	0.5	52.22	2.52
He (II) α	40.81	100	30.38	0
He (II) β	48.37	< 10	25.63	7.56
He (II) γ	51.02	n.a.	24.30	10.2
Ne (I) α	16.67	15	74.37	0
	16.85	100	73.62	0.18
Ne (I) β	19.69	< 1	62.97	3.02
	19.78	< 1	62.68	3.11
Ne (II) α	26.81	100	46.24	0
	26.91	100	46.07	0.1
Ne (II) β	27.69	20	44.79	0.88
	27.76	20	44.66	0.95
	27.78	20	44.63	0.97
	27.86	20	44.51	1.05
Ne (II) γ	30.45	20	40.71	3.64
	30.55	20	40.58	3.74
Ar (I)	11.62	100	106.70	0
	11.83	50	104.80	0.21
Ar (II)	13.30	30	93.22	0
	13.48	15	91.84	0.18

1.7 References

[1] Einstein, A. *Ann. Phys*. **1905**, *17*, 549.

[2] Koopmans, T. *Physica* **1933**, *1*, 104.

[3] Eland, J. H. D. *Photoelectron Spectroscopy*, Butterworth, **1974**.

[4] Cooper, J.; Zare, R. N. *J. Chem. Phys*. **1968**, *48*, 942.

[5] Samson, J. A. R.; Starace, A. *J. Phys. B, At. Mol. Opt. Phys*. **1975**, *8*, 1806.

[6] Vilesov, F. I.; Kurbatov, B. C.; Terrenin, N. *Soviet Phys. (Doklady)* **1961**, *6*, 490.

[7] Turner, D. W.; Al-Jobory, M. I. *J. Chem. Phys.* **1962**, *37*, 3007.

[8] Kruit, P.; Read, F. H. *J. Phys. E: Sci. Instrum*. **1983**, *16*, 313.

[9] Baltzer, P. *et al. Rev. Sci. Instrum*. **1993**, *64*, 2179.

[10] Pollard, J. E. *et al. Rev. Sci. Instrum*. **1981**, *52*, 1837.

[11] Wang, L. S.; Reutt, J. E.; Shirley, D. A. *J. Electron Spec. Rel. Phen.* **1988**, *48*, 167.

[12] Pradeep, T.; Shirley, D. A. *J. Electron Spec. Rel. Phen*. **1993**, *66*, 125.

[13] Niu, B.; Bai, Y.; Shirley, D. A. *J. Chem. Phys*. **1993**, *99*, 2520.

[14] Oku, M. *et al. J. Phys. Chem. A* **2008**, *112*, 2293.

[15] Jarvis, G. K. *et al. J. Chem. Phys.* **1999**, *111*, 9568.

[16] Merkt, F. *et al. J. Phys. B, At. Mol. Opt. Phys*. **1998**, *21*, 1705.

[17] Dietrich, H. J.; Muller-Dethlefs, K.; Baranov, L. Y. *Phys. Rev. Lett*. **1996**, *76*, 3530.

[18] Palm, H.; Merkt, F. *Chem. Phys. Lett*. **1997**, 270, 1.

[19] Schlag, E. W. *Zeke Spectroscopy*: Cambridge niversity Press: Cambridge, **1998**.

[20] Carlson, T. A.; Anderson, C. P. *Chem. Phys. Lett*. **1971**, *10*, 561.

[21] Piancastelli, M. N. *et al. J. Am. Chem. Soc.* **1983**, *105*, 4235.

[22] Douglas, C. *et al. Rev. Sci. Instrum*. **1977**, *48*, 926.

[23] Chandler, D. W.; Houston, P. L. *J. Chem. Phys*. **1987**, *87*, 1445.

[24] Eppink, A. T. J. B.; Parker, D. H. *Rev. Sci. Instrum*. **1997**, *68*, 3477.

[25] Suzuki, T. *Annu. Rev. Phys. Chem.* **2006**, *57*, 555.

[26] Ogi, Y. *et al. J. Phys. Chem. A* **2009**, *113*, 14536.

[27] Farmanara, P. *et al. J. Chem. Phys*. **1999**, *111*, 6264.

Chapter 2

Experimental Methods

2.1 History of photoion imaging

Photoelectron imaging (PEI) is a variant of photoion imaging that has been developed earlier. In this section, I briefly describe the historical background of photofragment imaging. The photoelectron and photoion imaging are sometimes more generally called charged particle imaging.

The first photofragment ion imaging was performed by Chandler and Houston in 1987 on photodissociation of methyl iodide (CH_3I).[1] The ion imaging apparatus is essentially the same as the Wiley-McLaren time-of-flight (TOF) mass spectrometer,[2] except that a 2D position-sensitive detector is used instead of an ion detector. The Wiley-McLaren spectrometer employs one flat electrode and two flat grids to create accerelation electric fields along the TOF axis, as shown in Fig. 2.1(a). The flat equipotential surface of the electric fields do not affect the tangential velocities of the charged particles. Therefore the arrival position of an ion with a particular mass on the detector will be proportional to the tangential velocity. However, since the arrival position varies linearly with the initial position in the ionization volume, the observed ion image is always blurred by the finite area of this volume, which limited velocity resolution. The velocity resolution was greatly improved by Eppink and Parker using the velocity map imaging (VMI) technique in 1997.[3] VMI uses open annular electrodes instead of grids to create curved equipotential surfaces that acts as an electrostatic lens. Thus, as shown in Fig 2.1(b), the lens focusses the ion trajectories with the same initial velocity to the same arrival position on the detector plane regardless of their initial position in

the ionization volume. The speed resolution was enhanced at least by a factor of 10, and diffraction of ions at the grids was eliminated. Wrede *et al.*[4] have modified the electrodes further to minimize chromatic and spherical aberrations in ion trajectories, improving the imaging resolution. In photoion/photoelectron imaging, a camera-based system and a delay line detector are commonly used as 2D position-sensitive detectors. A camera-based system consists of MCP, phosphor screen and CCD (or CMOS) camera, and only the particle arrival positions are recorded. In a delay line detector, finely spaced wires are placed behind the MCP to register both the arrival position and time. The drawback of the delayline detector is that it can handle only up to 4 to 5 hits in a response time of approximately 10 ns. Furthermore, the position (imaging) resolution is inferior to a camera-based system at this point. Considering the count rate and resolution, we use a camera-based system as a detector in the present study.

2.2 Image reconstruction

The recorded images mentioned above are the two-dimensional (2-D) projections of the three-dimensional (3-D) velocity distribution of photoelectron. Figure 2.2 shows the schematic diagram of image analysis. At the detector, the 3-D photoelectron cloud is flattened, resulting in a 2-D projection image. If the initial 3-D distribution has cylindrical symmetry, it can be reconstructed from a 2-D projection image by mathematical methods, such as inverse Abel transformation,[5] onion-peeling,[6] BASEX[7] and *p*-BASEX[8] etc., and the reconstructed 3-D distributions are generally displayed (as in this thesis) by showing the intensity cross section through the center of the initial 3-D electron cloud. In this thesis, only inverse Abel transformation and *p*-BASEX method are used for data analysis and will be described in the following section.

2.2.1 Inversion Abel Transformation

The 3-D velocity distribution of photoelectrons can be expressed in Cartesian coordinate centered on the point of photoionization as $i(x, y, z)$. Take z to be the symmetry axis (i.e. the laser polarization vector), y to be the direction of light propagation, and x to be the direction of an extraction field that accelerates the photoelectrons. Then the measured distribution on the detector as shown in Fig. 2.2(b) can be expressed as

$$p(\mathrm{y},\mathrm{z}) = \int_{-\infty}^{\infty} i(x,y,z)dx \tag{2-1}$$

At $z = z_0$, a row of the image, $f(y, z_0)$, taken along the y axis can be expressed as

$$p(\mathrm{y},z_0) = f(y) = \int_{-\infty}^{\infty} s(x,y)dx = 2\int_{0}^{\infty} s(x,y)dx \tag{2-2}$$

where $s(x, y)$ is a slice through the 3-D distribution perpendicular to the symmetry axis (z) taken at z_0. Figure 2.3 shows an example of the function $f(y)$ for a slice taken at $z = z_2$. Since $s(x, y)$ is cylindrically symmetric, equation (2-2) can be expressed in polar coordinates using

$$\mathrm{r} = \sqrt{(x^2+y^2)}$$

$$f(y) = 2\int_{x}^{\infty} \frac{s(r)r}{\sqrt{r^2-y^2}}dr \tag{2-3}$$

This is the Abel transformation, and $s(r)$ will be obtained from the measurement of $f(y)$ by the inverse Abel transform

$$s(r) = \frac{1}{\pi}\int_{r}^{\infty} \frac{df/dy}{\sqrt{y^2-r^2}}dy \tag{2-4}$$

Utilizing this derivation equation, we can recover the original distribution $s(r)$ from the experimentally measured projection $f(y)$. However, solving equation (2-4) is difficult in practice. In order to remove this difficulty, the most commonly used method for calculating the inverse Abel transform is the Fourier–Hankel method,[9] the original distribution $s(r)$ can then be transformed to

$$s(r) = 2\pi\int_{0}^{\infty} qJ_0(2\pi rq)\left[\int_{-\infty}^{\infty} f(x)\exp(-2\pi xq)\,dy\right]dq \tag{2-5}$$

where the zero-order Bessel function, J_0, is given by

$$J_0(z) = \frac{1}{2\pi} \int_0^{2\pi} \exp(-izcos\vartheta)\, d\vartheta \tag{2-6}$$

The drawback of using Fourier-Hankel algorithm to solve the inverse Abel integral is that the noise of the image is magnified and accumulates toward the center line, as shown in Fig. 2.4(b).

2.2.2 BASEX and *p*-BASEX method

Compare to inverse Abel transformation, BASEX (Basis Set Expansion) method involves simulation and fitting of a set of "basis images" to the experimental images in order to extract the parameters of interest. The experimental projection data are expanded over a set of basis functions that are analytical projections of known well-behaved functions, Gaussian-like function. The original 3-D image is then reconstructed as a linear combination of these well-behaved functions.

As mentioned in the previous section, the projection image onto the (y, z) detector plane can be described by the Abel integral (see Eq. 2-3)

$$P(y,z) = 2 \int_{|y|}^{\infty} \frac{I(r,z)r}{\sqrt{r^2 - y^2}} dr \tag{2-7}$$

In the imaging experiment, this projection function is binned on the CCD, which has a size of $N_y \times N_z$ pixels, leading to the digitized projection function **P**

$$\mathbf{P}_{ij} = 2 \int h(y - y_i, z - z_i) dydz \int_{|y|}^{\infty} \frac{rI(r,z)}{\sqrt{r^2 - y^2}} dr \tag{2-8}$$

where $h(y, z)$ defines an instrumental function. Now, consider a set of 2D function in the image space $\{f_k(r, z)\}$ (k = 0,…,K-1) and their corresponding projection basis set $\{\mathbf{G}_k\}$. They are related via equation (2-7)

$$\mathbf{G}_{kij} = 2 \int h(y - y_i, z - z_i) dydz \int_{|y|}^{\infty} \frac{rf_k(r,z)}{\sqrt{r^2 - y^2}} dr \tag{2-9}$$

If both sets ($f_k(r, z)$ and $\mathbf{G}_k$) are well-behaved under the Abel trasform, the 3-D velocity distribution $I(r, z)$ and its projection $\mathbf{P}_{ij}$ can be described as expansions in the basis set using

the same expansion coefficients (C_k)

$$I(\mathrm{r},\mathrm{z}) = \sum_{k=0}^{K-1} \mathbf{C}_k f_k(r,z) \tag{2-10}$$

$$\mathbf{P}_{ij} = \sum_{k=0}^{K-1} \mathbf{C}_k \mathbf{G}_{kij} \tag{2-11}$$

In the matrix form

$$\mathbf{P} = \mathbf{CG} \tag{2-12}$$

$$\mathbf{C} = \mathbf{G}^{-1}\mathbf{P} \tag{2-13}$$

with the coefficients vector **C** = ($\mathbf{C}_0$,…,$\mathbf{C}_{K-1}$) and the basis transformation matrix G = ($\mathbf{G}_0$,…, $\mathbf{G}_{K-1}$)^T. Noted that the basis set matrix **G** is inverted by the Tikhonov regularization method.[10] Because the basis set matrix does not depend on the data matrix, they could be computed once and used afterward for the retrieval of the expansion coefficients **C** by relatively fast matrix multiplication.

Compare to the original BASEX method which uses Cartesian basis set function, the polar modified BASEX (*p*-BASEX) transform the image from the Cartesian coordinates of the detector to polar coordinates prior to the inversion. This transformed image is then fitted with {*r*, *θ*} basis functions where the angular terms are restricted to just those Legendre polynomial functions. The advantage of operating on the image in {*r*, *θ*} space is that it minimizes the CPU time compare to in Cartesian space, and the noise is accumulated toward a central spot which is usually never used for the data analysis, as shown in Fig. 2.4(c).

2.3 Experimental setup

2.3.1 He(I) discharge lamp

He(I) radiation (21.22 eV) was generated using a commercial discharge lamp[11] (Omicron, HIS13), it can couple to a linear polarizer to generate a polarized photon source or a capillary to derive the unpolarized VUV light into the ionization chamber.

(A) He(I) with polarizer

Figure 2.5(a) shows the He(I) lamp with a continuously rotatable three-mirror linear polarizer. The polarizer consists of three gold coated mirrors with the special feature of additional focusing via a toroidal mirror,[12] the beam diameter is around 1.5 mm at the sample position, the polarization direction can be rotated 360 degree on VUV light path axis by adjusting the rotary drive (see Fig. 2.5), the maximum polarization efficiency is 88 % at the He(I) wavelength of 58.4 nm (21.22 eV). Due to the transmission of the polarizer is 4 %, photon flux was reduced from 1.0×10^{13} photons/sec to 4.0×10^{11} photons/sec if the reflectivity of the polarized is perfect. A 6 mm ϕ aperture was installed at output of the polarizer to block the external light spot, which is caused by the misalignment inside He(I) lamp.

(B) He(I) without polarizer

Figure 2.5(b) shows the He(I) lamp after removed the polarizer. In this case, 0.8-mm-inner diameter capillary was used to derive the VUV light beam into the ionization chamber and the photon source is unpolarized light. Accordingly to the manual, the beam divergence is estimated to be $\pm$ 0.8°, and the beam diameter at the sample position can be estimated by the following equation

$$\text{Beam dia.} = 0.0272 \times L + (\text{capillary inner dia.}) \quad (2\text{-}14)$$

where L is the capillary–sample distance. Without the loss of photon flux caused by a reflective polarizer and an aperture in the photon beam, the photon flux is estimated to be 1.3×10^{12} photons/sec.

2.3.2 Vacuum chamber

The research works reported in this thesis were performed in two different vacuum chambers. In the beginning, the He(I)-PEI was tested with a vacuum chamber that was originally designed for laser spectroscopy of liquid droplets in our laboratory. However, after

some experiments, we confirmed that the electrostatic lens should be redesigned but that the size of this vacuum chamber geometrically restricts the modification. Therefore, we decided to use another vacuum chamber, with a larger inner space, designed for photoelectron imaging using a vacuum ultraviolet (VUV) free electron laser. In fact, the present work aimed at development of a PEI spectrometer that can be used with a VUV free electron laser, and this chamber was available for research and development of He(I) PEI for a plenty of time, since the beam time of the VUV laser was highly limited owing to time-sharing by the users. The use of this chamber turned out to be highly successful.

(A) The old vacuum chamber for laser spectroscopy of liquid droplet

As shown in Fig. 2.6, the apparatus consists of four vacuum chambers: a molecular beam source, a buffer, an ionization and a quadrupole chamber. A continuous supersonic jet was generated by expanding a sample gas through a 25-μm-diameter orifice at 294 K in the source chamber that was evacuated by two turbo molecular pumps (2 × 2200 L/sec, BOC Edwards, F2203C). The supersonic jet was skimmed by a conical Al skimmer (2 mm ϕ) in the source chamber, and collimated by the second conical Al skimmer (5 mm ϕ) in the buffer chamber evacuated by a turbo molecular pump (350 L/sec, Leybold, TurboVAC361). The molecular beam thus generated was introduced into an ionization chamber evacuated by a 2650 L/sec turbo molecular pump (BOC Edwards, XA2703C), it travels parallel to the face of the imaging detector and intersected perpendicularly with He(I) radiation at 380 mm downstream from the nozzle. The differential pumping vacuum system provides the inside pressures of 3.1 $\times 10^{-5}$ Torr, 3.9 $\times 10^{-6}$ Torr and 3.5 $\times 10^{-8}$ Torr in the source, buffer and ionization chambers, respectively, during stagnation pressure of 0.9 MPa of Ar is operated.

Figure 2.7(a) shows a cross section of the ionization chamber. The He(I) discharge lamp with a polarizer was used. (see Sec. 2.3.1 A) The electrons generated by the photoionization of atoms or molecules in a beam were accelerated in static electric fields and projected onto a

2D position sensitive detector. The acceleration field was created using stacked circular ring electrodes and the field gradient was carefully adjusted to achieve a velocity mapping condition.[3] This electrodes stack consist of eight stainless steel rings, which are spaced by 3 mm ϕ ruby balls, and connected to each other by 1MΩ resistors, as shown in Fig. 2.7(b). The whole regions of photoionization, acceleration, and flight for photoelectrons were shielded against an external magnetic field with a permalloy tube. After photoionization, the photoelectrons are accelerated perpendicular to both the propagation directions of a molecular beam and the VUV light, and detected by the position sensitive detector, consists of a dual microchannel plate (Hamamatsu F1942-04, 25 μm ϕ pore size, 25 μm pitch length, and 77 mm ϕ effective area), a phosphor screen (Hamamatsu P43), and a CCD camera (Hamamatsu i-CCD, 25 Hz, 768 × 572 pixels). Room light is blocked from the collection zone between phosphor screen and CCD camera.

(B) A new vacuum chamber

Figure 2.8 shows the schematic of the new vacuum chamber. The apparatus consists of two vacuum chambers, a molecular beam source and an ionization chamber. We used a continuous or pulsed molecular beam depending on the experiment. In the former case, a continuous supersonic jet was generated by expanding a sample gas from a 25-μm-diameter orifice at 294 K. The jet was skimmed with a 2.0-mm-diameter skimmer and introduced into an ionization chamber, and a molecular beam is travelling parallel to the flight tube axis. The source and ionization chambers were pumped by turbomolecular pumps with pumping rates of 2000 L/s (N_2) and 820 L/s (N_2), respectively. When Ar was continuously expanded at a stagnation pressure of 1 atm, the ionization chamber pressure was ca. 7.3×10^{-8} Torr. The polarizer of He(I) was removed (see Sec. 2.3.1 B), the end of the capillary was located ~125 mm from the ionization point. Consequently, the diameter of the He(I) radiation is estimated to be 4.2 mm at the ionization point by utilizing equation (2-14) and the photon flux is 9.4 ×

10^{10} photons/s/mm^2 at 21.22 eV (58.4 nm). Electrons generated by photoionization of a sample were accelerated along the molecular beam propagation axis and projected onto a 2D position-sensitive detector. The details of the electrodes are described later (see. chapter 3). The entire regions of photoionization, acceleration, and flight of the electrons were shielded against external magnetic fields by a permalloy tube. The position-sensitive detector consists of a chevron-type (dual) microchannel plate assembly (Hamamatsu, F1942-04; pore diameter: 25 μm; diameter: 77 mm) backed by a phosphor screen (P43) and a CCD camera (Andor, iXon^{EM} DCL897; 512 × 512 pixels).

In the time-gated experiments, 10–20% sample gases seeded in He were expanded from a pulsed valve (General Valve; orifice diameter: 100 μm) with a stagnation pressure of about 0.2–0.55 atm. The front surface of the MCP assembly was maintained at the ground potential and the voltage applied to the rear side was switched between 900 and 1400 V using a high voltage pulser (DEI, GRX-3.0K-H; voltage amplitude: ±3.0 kV) to time gate the MCP synchronously with a pulsed gas nozzle. The timing of the trigger pulses for the gas nozzle, MCP, and CCD camera were controlled with a digital delay generator (Stanford Research Systems, DG535)

2.4 Data analysis

2.4.1 Image center calibration

In general, the center of the recorded image is offset in the frame of the camera. Therefore, before the reconstruction of the full 3D distribution, the center of the recorded image must be found. This is first checked by eye or by overlaying a circle on the raw image to determine the center pixel. After an initial center is found, the pixels surrounding this center are also utilized as a center to reconstruct the full 3D distribution. Consequently, the corresponding radial distributions could be obtained from the angle integration of their 2D

slice images. Because a few pixels deviation from the real center is enough to degrade the reconstructions severely, the accurate center pixel is found until the narrowest radial distribution is achieved.

2.4.2 Calibration of photoelectron kinetic energy (PKE) distribution

After a reconstruction of the full 3D distribution, a slice image through the center of the 3D distribution is obtained, and the radial distribution of 2D slice image is the angle integrated intensity as a function of pixel. As mentioned before, in velocity mapping condition, the radius of the image *R* is directly proportional to the expansion speed $\upsilon_{\perp}$, which is in the direction perpendicular to the flight tube axis, and can be simply described by

$$R = N\upsilon_{\perp}t$$
$$= \frac{2}{m}Nt\sqrt{eKE} \quad (2\text{-}15)$$

where *t*, *eKE* and *N* are the time-of-flight, photoelectron kinetic energy and the magnification factor, respectively. Judging from equation (2-15), the radial distribution of 2D slice image represents the velocity distribution, and the proportionality constant between the velocity and *eKE* can be found by plotting the *eKE* vs. R^2 for a known atomic transition measured in the photoelectron spectrometer, therefore the plot can be converted from a pixel scale to an eKE scale. Consequently, the electron binding energy (eBE) scale is converted by subtraction of the electron kinetic energy from the photon energy [eg. 21.22 eV for He(I)]

$$eBE = h\nu - eKE \quad (2\text{-}16)$$

In the time of flight direction, the electrostatic field (qV_R) accelerates the photoelectrons to achieve the velocity $\upsilon_{\parallel}$ along to the flight tube axis, and $\upsilon_{\parallel}$ is inversely proportional to the time-of-flight (*t*)

$$t \propto \frac{1}{\upsilon_{\parallel}} \quad (2\text{-}17)$$

$$\frac{1}{2}m{\upsilon_{\parallel}}^2 = qV_R \quad (2\text{-}18)$$

Therefore

$$t \propto \sqrt{m/(qV_R)} \tag{2-19}$$

Compare to equation (2-15)

$$R \propto \sqrt{eKE/(qV_R)} \tag{2-20}$$

where m, q and V_R are the mass of the electron, the charge of the electron and the repeller voltage, respectively. As shown in equation (2-20), the repeller voltage determines the image size on the detector. Therefore a new calibration is needed while the pixel energy scale is different at different repeller voltage.

2.4.3 Photoelectron angular distribution (PAD)

Figure 2.9 shows an example of photoelectron image of Kr obtained for free electron laser (Fig. 2.9 case A) and He(I) (Fig. 2.9 case B). As mentioned in chapter 1, for one-photon ionization with polarized light, a PAD is expressed by equation (1-4) and cylindrically symmetric about the polarization axis of light, as shown in Fig. 2.9 (A). The angle (θ) is measured between the polarization axis of light and the outgoing photoelectron velocity. Therefore, positive and negative β corresponds to the preferential ejection of electrons parallel and perpendicular to the ionization laser polarization. With unpolarized light, a PAD is expressed by equation (1-10) and cylindrically symmetric about the light propagation direction, as shown in Fig. 2.9 (B). In this case, the angle (θ') is measured between the light propagation direction and the outgoing photoelectron velocity. Positive and negative β corresponds to the preferential ejection of electrons perpendicular and parallel to the light propagation direction. As shown in fig. 2.9, after the inverse Abel transform, the slice image can be transform to polar plot. Then, the photoelectron angular distribution (PAD) for a specific velocity can be obtained by integration over the selected radial region (for example, the yellow dotted rectangle in Fig. 2.9) and the anisotropy parameter is analyzed using

equation (1-4) or equation (1-10) for polarized or unpolarized light, respectively.

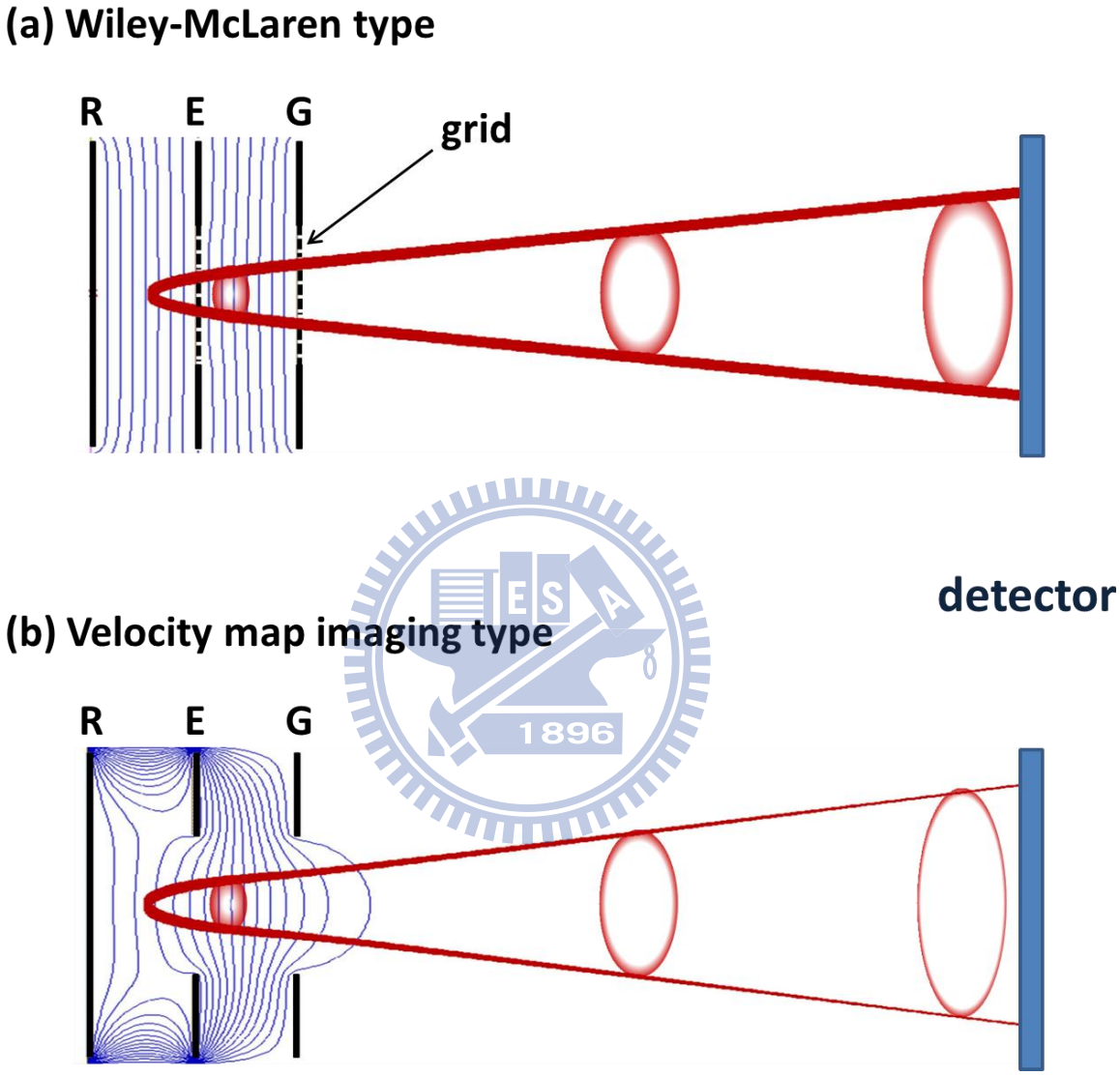

Figure 2.1 (a) W-M type electrode consists of one flat plate and two flat grids. (b) Velocity mapping type electrodes are the W-M type electrodes with annular holes instead of grids.

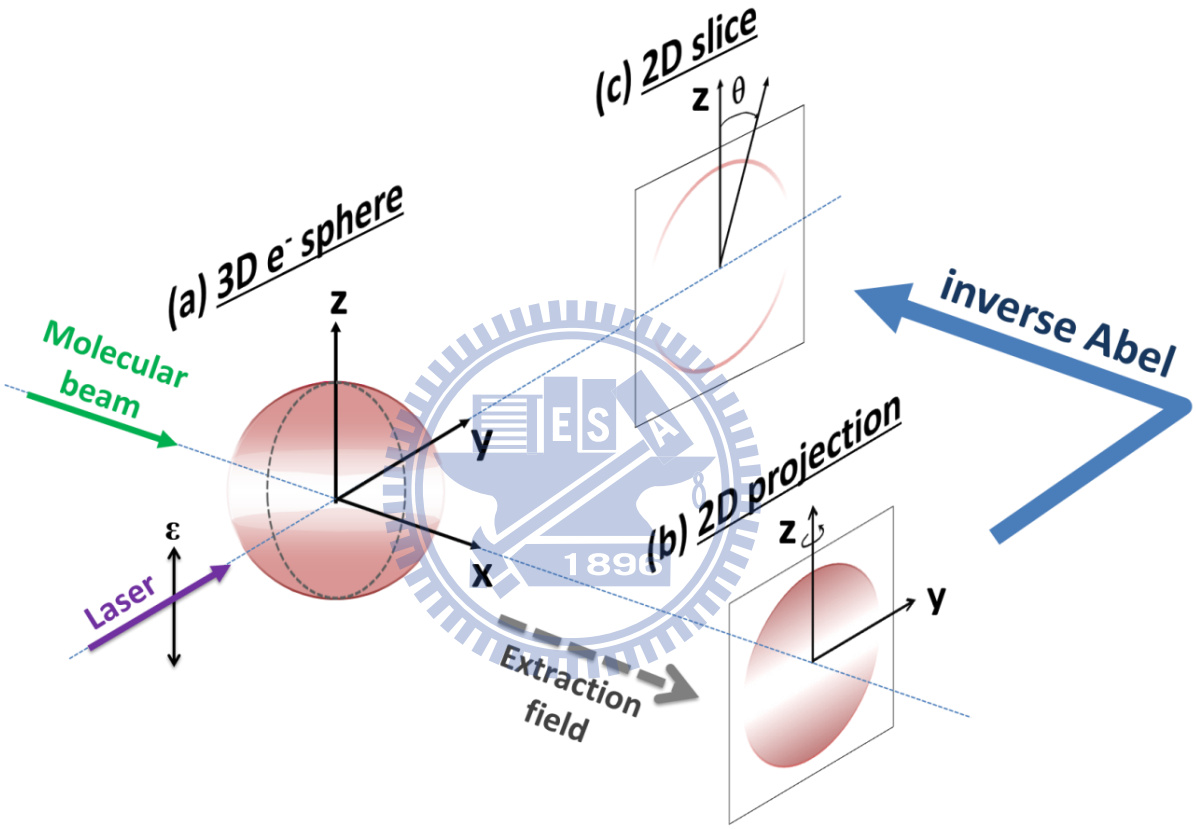

Figure 2.2 The schematic diagram of image analysis.

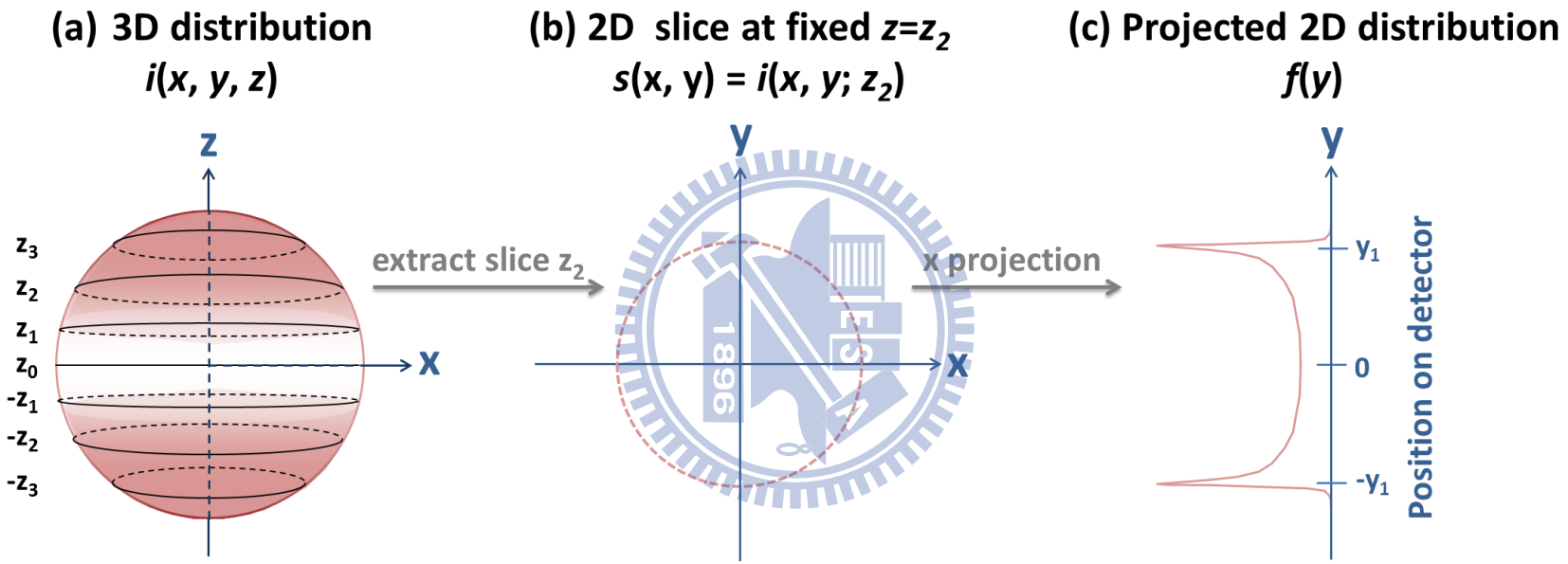

Figure 2.3 (a) Slice pattern of 3D distribution through fixed z in xy-plane. (b) 3D slice image at z_2. (c) The projection of (b) maps the electrons onto a line on the detector.

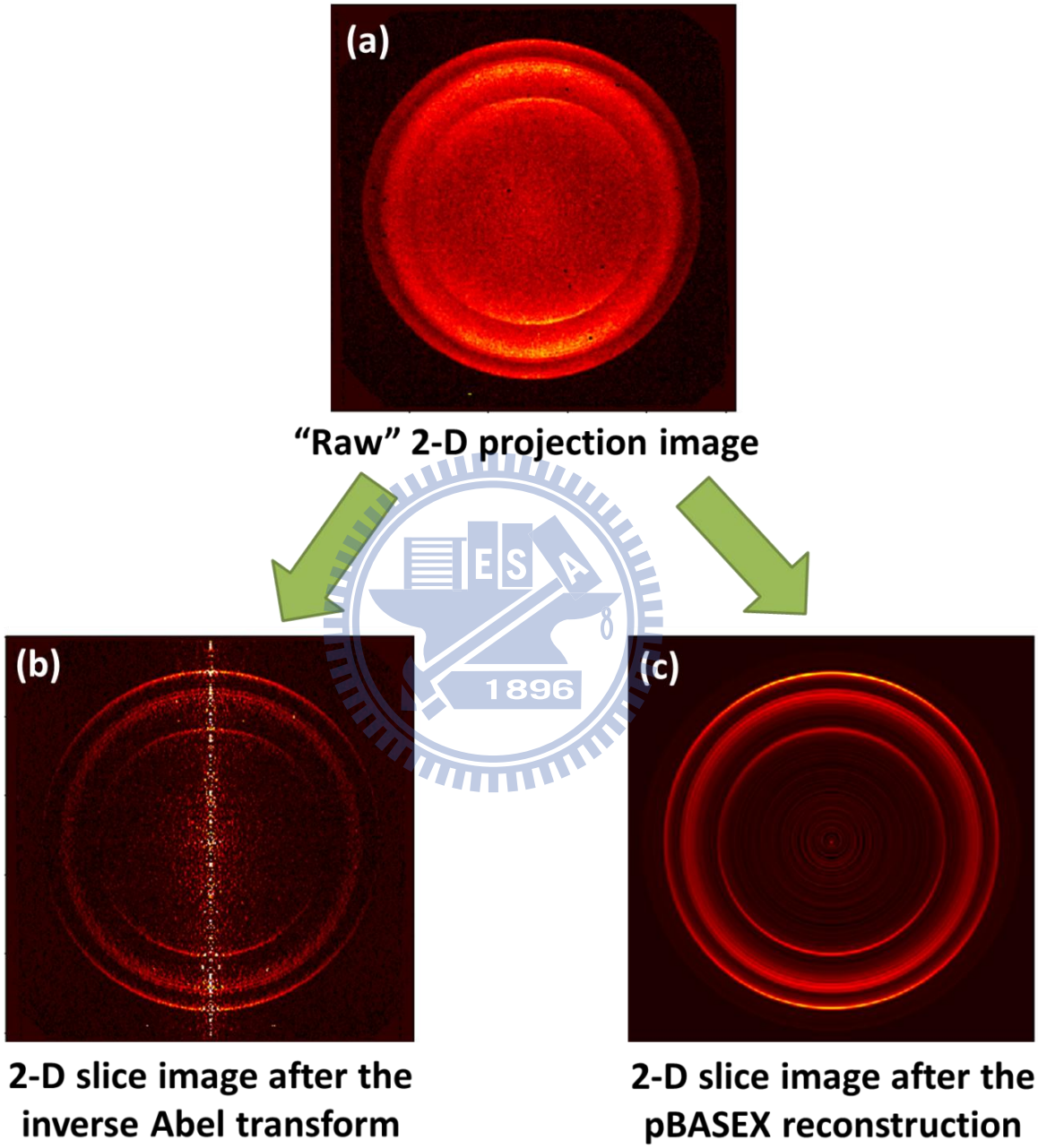

Figure 2.4 (a) The raw projection image of N_2. (b) The 3D slice image after inverse Abel transformation. (c) The 3D slice image after *p*-BASEX reconstruction.

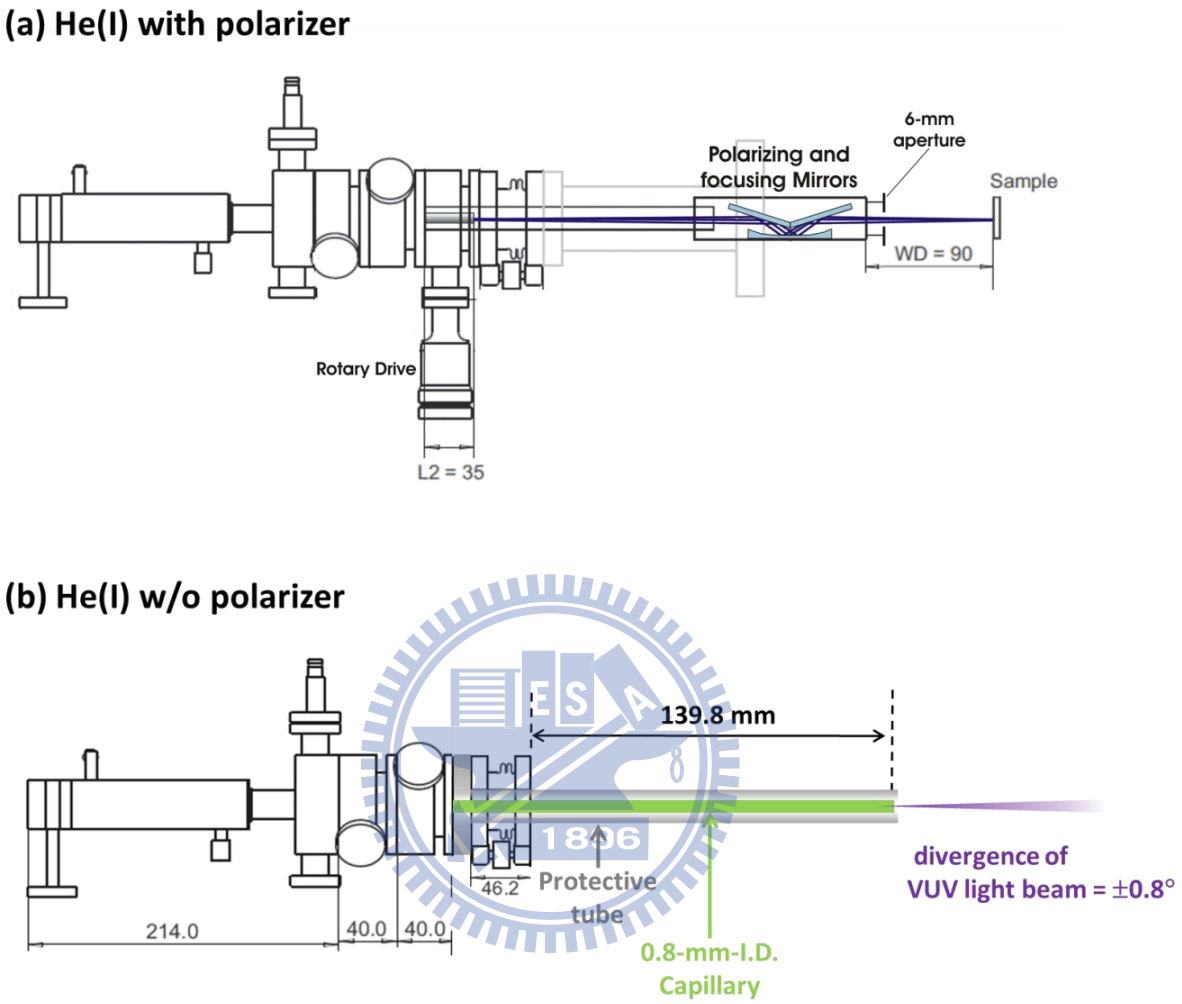

Figure 2.5 The schematic drawing of He(I) discharge lamp: (a) with a linear polarizer; (b) the linear polarizer was replaced by 0.8mm-diameter capillary.

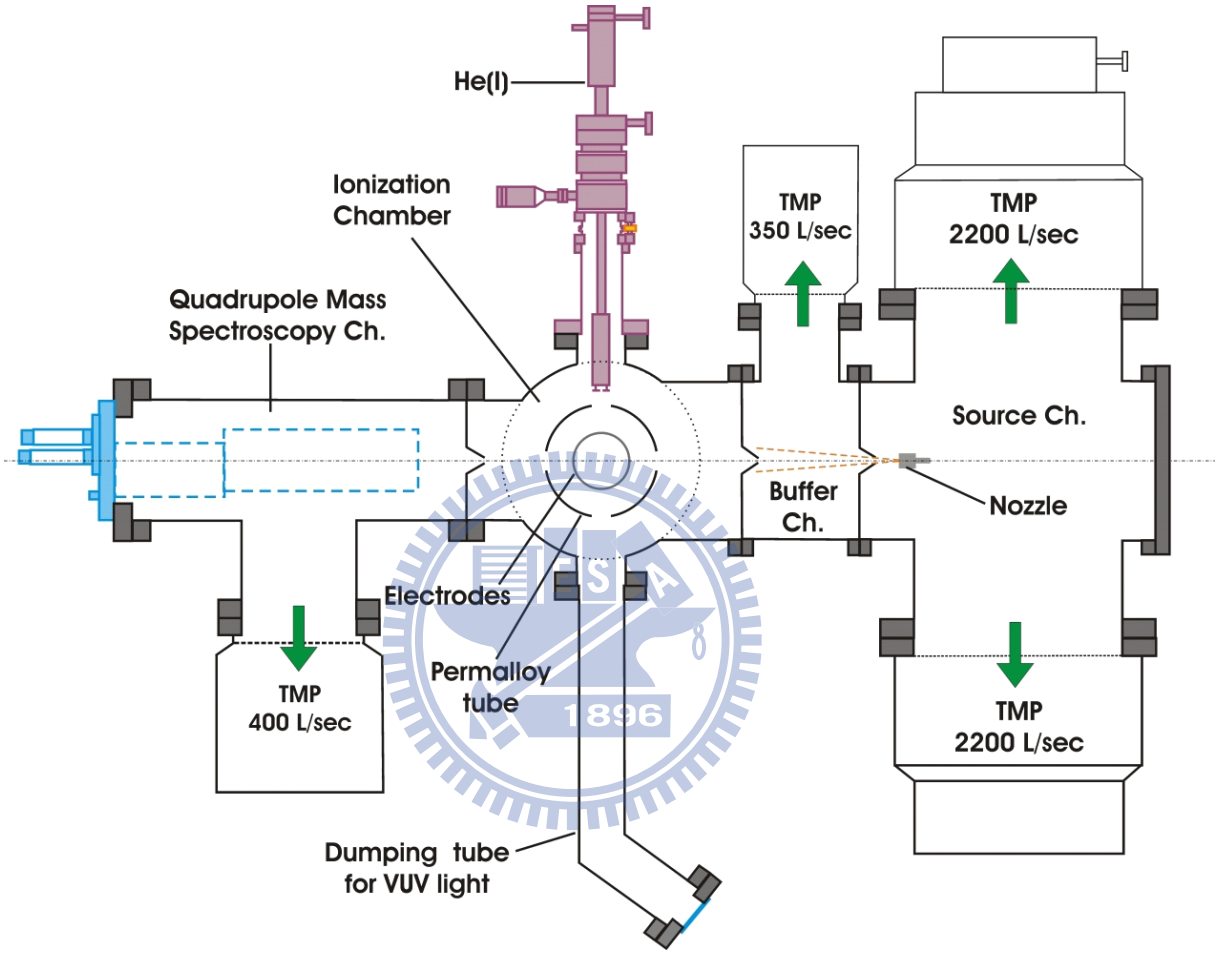

Figure 2.6 The schematic drawing of the entire vacuum chamber which is originally designed for droplet experiment.

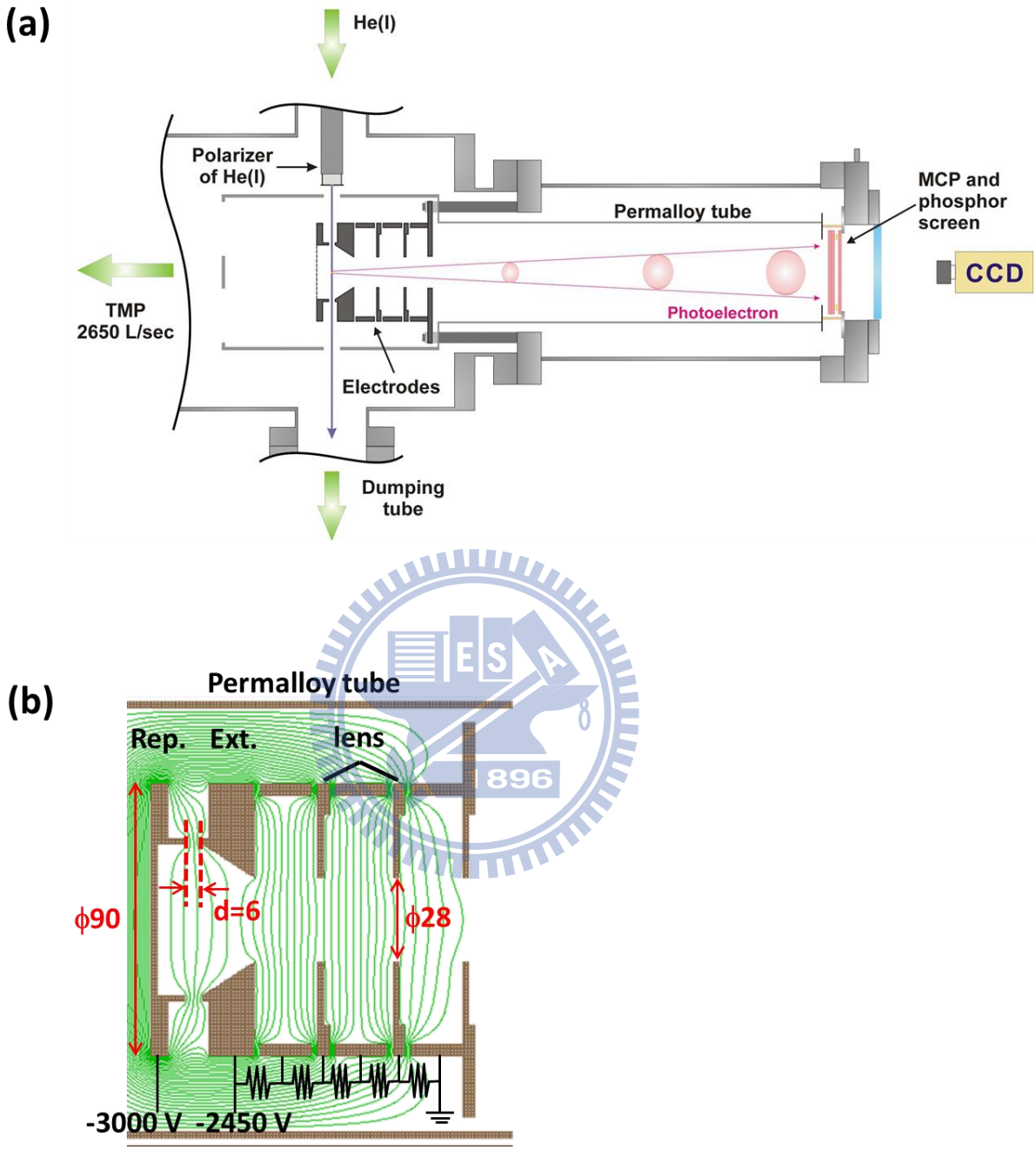

Figure 2.7 (a) The cross-sectional view of the ionization chamber and the imaging system. (b) The cross-sectional view and field lines for the electrostatic lens system. The electrode gap between repeller and extractor electrode is denoted as d. In the original design, d = 6 mm.

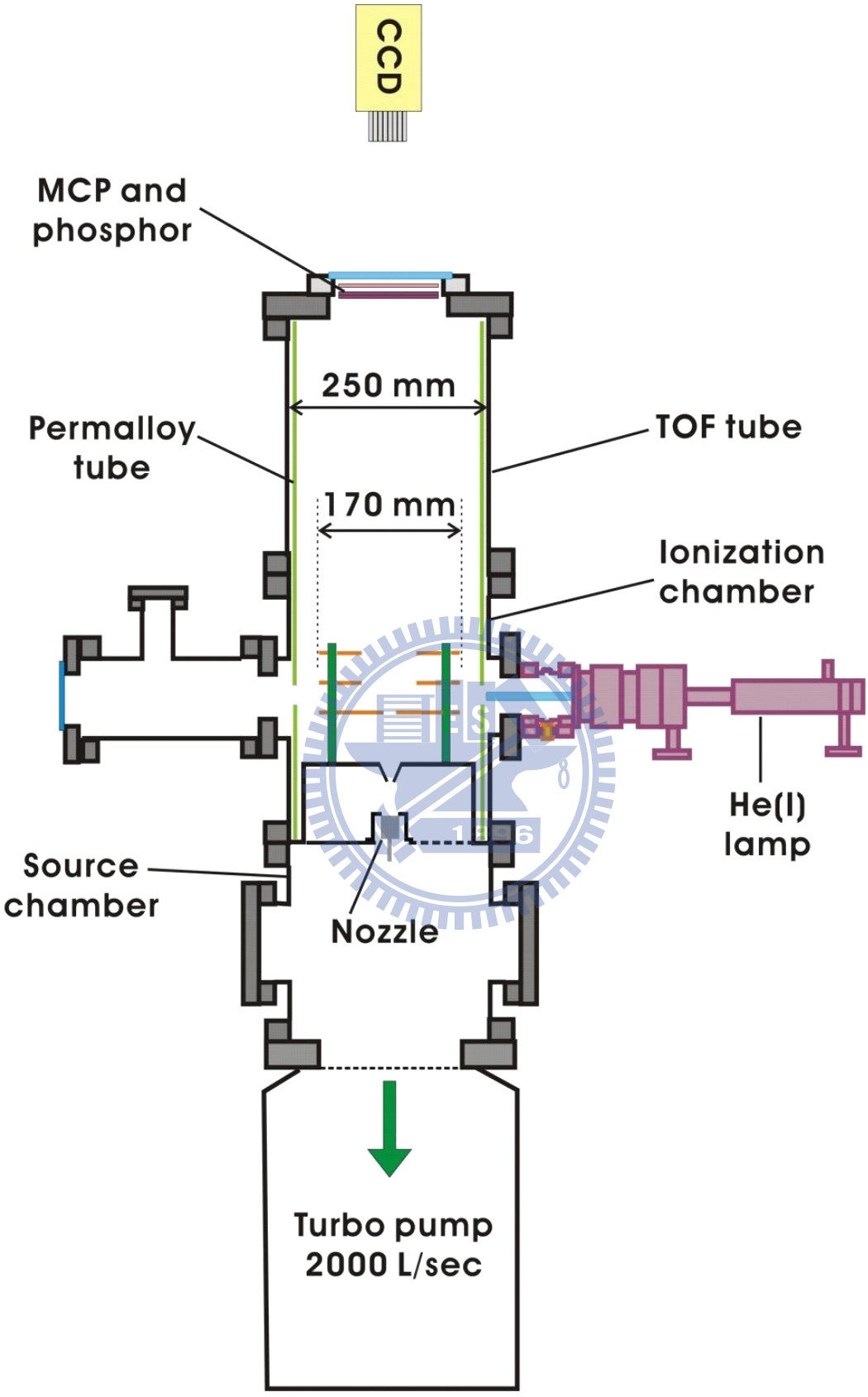

Figure 2.8 The schematic view of the new vacuum chamber.

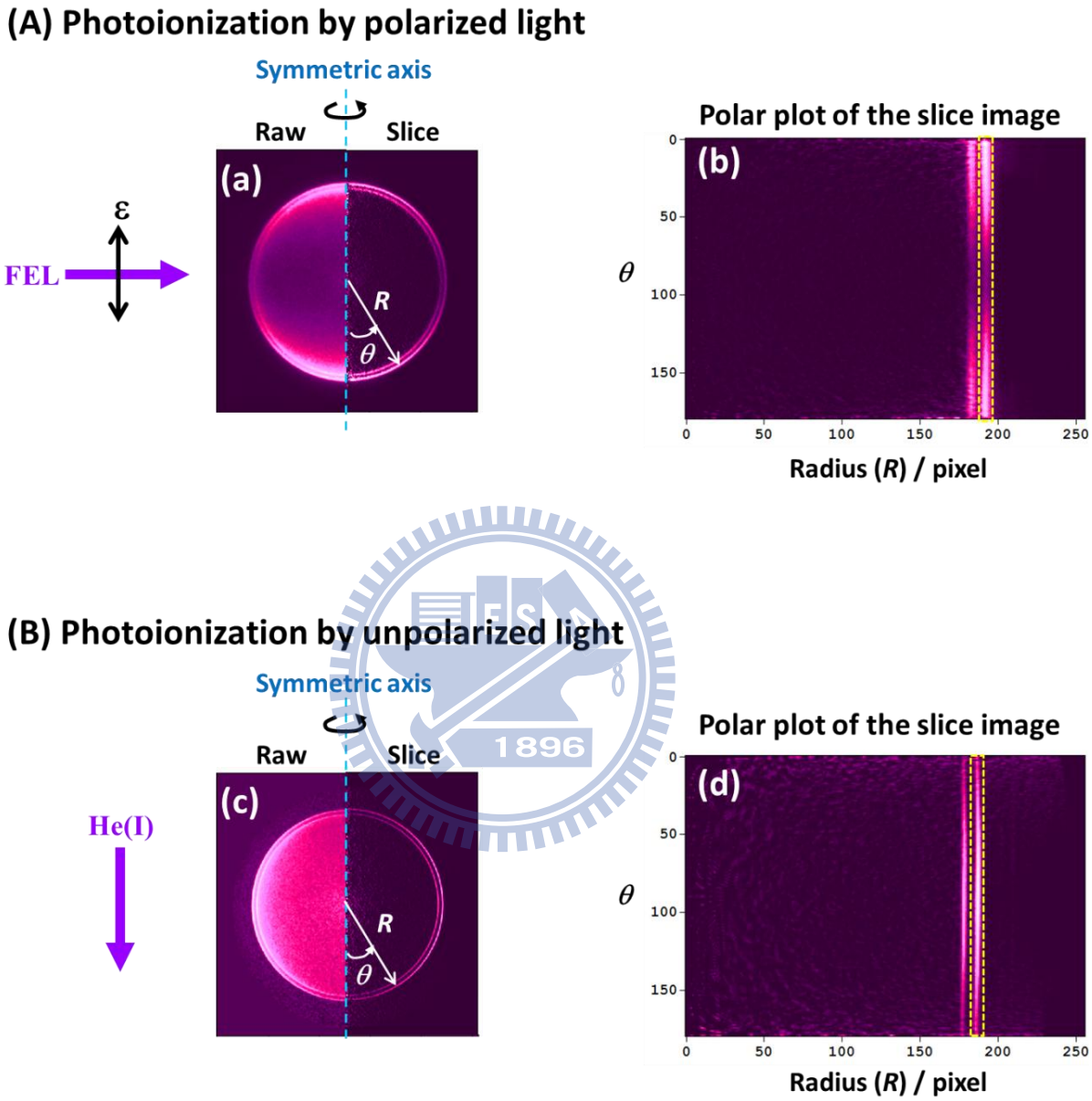

Figure 2.9 (a) and (c) are the PEI of Kr obtained for free electron laser and He(I), respectively: the left half is the raw image and the right half is the slice image obtained by taking the inverse Abel transform. (b) and (d) are the polar plots of slice images obtained from (a) and (c), respectively.

2.5 References

[1] Chandler, D. W.; Houston, P. L. *J. Chem. Phys.* **1987**, *87*, 1445.

[2] Wiley, W. C. and McLaren, I. H.; *Rev. Sci. Instrum.* **1955**, *26*, 1150.

[3] Eppink, A. T. J. B. and Parker, D. H. *Rev. Sci. Instrum*. **1997**, *68*, 3477.

[4] Wrede, E. *et al. J. Chem. Phys.* **2001**, *114*, 2629.

[5] Bordas, C.; Paulig, f.; Helm, H.; Huestis, D. L. *Rev. Sci. Instrum*. **1996**, *67*, 2257.

[6] Manzhos, S. and Loock, H.-P. *Comput. Phys. Commun*. **2003**, *154*, 76.

[7] Dribinski, V. et al. *Rev. Sci. Instrum*. **2002**, *73*, 2634.

[8] Garcia, G. A.; Nahon, L.; Powis, I. *Rev. Sci. Instrum*. **2004**, *75*, 4989.

[9] Smith, L. M.; Keefer, D. R.; Sudharsanan, S. I. *J. Quant. Spectrosc. Radiat. Transf*. **1988**, *39*, 367.

[10] Tikhonov, A. N. *Sov. Math. Dokl*. **1963**, *4*, 1035.

[11] Schönhense, G.; Heinzmann, U. *J. Phys. E: Sci. Instrum.*, **1983**, *16*, 74.

[12] Hancock, W. H.; and Samson, J. A. R. *J. Electron. Spectrosc. Relat. Phenom*. **1976**, *9*, 211.

Chapter 3

Designing a Photoelectron Imaging Spectrometer for He(I) Light Source

Photoelectron imaging (PEI) has been performed on a number of molecular systems using nanosecond and femtosecond lasers. However, since He(I) radiation generated by a discharge lamp has much poorer beam characteristics than these coherent laser radiation, successful PEI experiments with He(I) radiation requires redesigning of the apparatus. The major problem of He(I) radiation is that it has a large divergence angle and cannot be focused as tightly as laser beams. This causes two practical problems. One is background photoemission from the apparatus caused by scattered light. The other is a large ionization volume that limits the electron energy resolution of PEI.

In this chapter, I describe the procedures taken to identify the source of background photoemission and to improve the performance of the apparatus. A new design of electron acceleration electrodes successfully reduces background photoemission and achieve sufficiently high electron energy resolution for He(I) PEI.

3.1 He(I) PEI experiment using an old vacuum chamber

In the initial stage of this work, I have used the apparatus originally designed for laser spectroscopy of liquid droplets. The schematic view of the experimental setup is shown in Fig. 2.6 and 2.7. A light source was the He(I) discharge lamp equipped with a rotatable

three-mirror polarizer (see Fig. 2.5a).

3.1.1 Reduction of background noise

Figure 3.1(a) shows the first photoelectron image of Ar measured with He(I) radiation. The outer rings seen in the raw image are photoionization signal of Ar, while the inner part of the image exhibits a background photoemission signal that was observed even without a molecular beam. The background has never occurred in photoelectron imaging (PEI) with a well-collimated laser beam. The background signal disappeared when the acceleration electric field was turned off, which indicated that background signal is not carried by photons but the photoelectrons from the apparatus. In order to reduce the scattered light inside the chamber, graphite powder (Areodag) was painted on the entire inner surface of the ionization chamber and the PEI electrodes. A He(I) beam dumper was also attached to the ionization chamber to minimize the back reflection of He(I) radiation from its exit port (see Fig. 2.6). However, the background was not eliminated by those modifications.

On the other hand, I found that the background signal decreased by reducing the diameter of the He(I) radiation (see Fig. 2.5a). Figure 3.1 shows the photoelectron images of Ar for different aperture diameters (a) 6 mm and (b) 2 mm of the He(I) lamp. The result clearly indicates that He(I) radiation illuminates some vacuum components adjacent to its light path, causing background photoemission. Thus, we suspected that the acceleration electrodes of electrons are the source of the background.

To reduce the background, I have enlarged the gap between the electrodes to allow the He(I) radiation passes through without scattering. Figures 3.2(a)–(c) show the photoelectron images of Kr measured with the electrode gaps (denoted as d in Fig. 2.7b) of 6, 9 and 12 mm, respectively. In Figs. 3.2 (b) and (c), the aperture diameter of He(I) was also reduced from 2 to 1.3 mm. In order to estimate the diameter of the He(I) radiation in the ionization chamber, I introduced the emission from a high intensity halogen lamp along the same path with the He(I)

radiation. The diameter (FWHM) of the photon beam was 3.0 and 2.5 mm at the exit side of the electron acceleration lens for the aperture sizes 2 and 1.3 mm for the photon beam, respectively. Therefore, Fig. 3.2 (c) indicates that the electrode gap should be 5 times larger than the estimated VUV beam diameter to suppress the background photoemission. This means that a considerable intensity of a halo exists around the VUV beam. The results clearly show that the broad background feature in the center gradually diminishes when increasing the electrode gap.

3.1.2 He(I) photoelectron images of supersonic beams of Ar, Kr and N_2

(A) Determination of polarization degree of He(I) radiation

The polarization degree of He(I) radiation has to be determined for the analysis of photoelectron angular distribution. Since the gold-coated mirror surfaces in the polarizer may be contaminated and/or degraded, it is possible that the polarization degree may vary with time. We measured photoelectron images of rare gases and analyzed the images and determined the polarization degree as to reproduce the anisotropy parameter β reported in the literature. Figure 3.3 shows the difference between the literature value (1.24)[1] for Kr ($^2P_{3/2}$) and the value extracted from *p*-BASEX analysis of our image by assuming different polarization degrees of light. The best agreement was obtained at the polarization degree of 74%.

(B) Examination of cluster formation in supersonic beams

The images of Kr and Ar presented above were obtained at a stagnation pressure of 2.2 MPa for supersonic jet expansion. The high stagnation pressure was used to compensate considerable dilution of the gas density at the ionization point that is far (380 mm) from the nozzle. Since these rare gas atoms may form clusters and exhibit different anisotropy parameters from that of free atoms, the pressure dependence of photoelectron images was

investigated. Clusters can be identified from smaller ionization energies than that of free atoms, because the ionized atom is stabilized by solvation in the clusters.[2] However, as shown in Fig. 3.4, the PKEDs in the He(I) photoionization of Ar are almost unchanged for different stagnation pressures of 0.4, 1.1, and 2.2 MPa, and the angular anisotropy parameters determined for the main peak in PKED were 0.93, 0.92 and 0.94, respectively. Thus, the cluster formation in our supersonic beam had negligible influence on the determination of the polarization degree of the He(I) radiation.

(C) Results

The images presented in the previous section were recorded by integrating the signal intensity from the CCD chip without any image processing. In this simple integration mode, an image of the light spot due to electron appears much larger than one pixel size of a CCD and degredes the energy resolution of PEI. The center-of-gravity (COG) calculation of each light enhances the resolution. Figure 3.5 shows photoelectron images observed by He(I) photoionization of supersonic beams of Ar, Kr and N_2 with COG calculations. In COG calculations, if the light spots overlap each other in an image frame, COG of light spots and their number of hits are miscalculated; therefore, COG calculation must be performed at sufficiently low signal count levels. In this particular experiment to obtain Fig. 3.5, the background photoelectron signal was strong, and we lowered the gain of MCP to achieve the optimum condition for COG calculations. Consequently, each of the integration time of the signal and the background images were 4.5 hours, 5.5 hours and 17.7 hours for Ar, Kr and N_2, respectively.

Figure 3.6 shows the PKEDs of Ar and Kr extracted from these images. The spin-orbit splitting of Kr (0.665 eV) is clearly resolved: the best-fit Gaussian function had the FWHM of 0.248 eV at 7.22 eV, which corresponds to an energy resolution ($\Delta E/E$) of 3.4 %. This resolution is insufficient to resolve the fine structure splitting of Ar (0.178 eV). Figure 3.7(a)

shows the PKEDs of N_2, in which three bands, corresponding to the X, A, and B states of the cation, are identified. The expanded view of the A band is shown in Fig. 3.7(b). The spectral feature agrees well with the literature.[3] The anisotropy parameters of Ar, Kr are analyzed using equation (1-4) and compared with the literature values in Table 3.1 and 3.2, respectively. The anisotropy parameters are in agreement with the literatures.

3.2 He(I) PEI experiment using a new vacuum chamber

The schematic view of the new experimental setup is shown in Fig. 2.8. The linear polarizer of He(I) discharged lamp was replaced with a 0.8-mm-diameter capillary to increase the photon flux (see Fig. 2.5b).

3.2.1 Testing three electrode design by Eppink and Parker

As described in the earlier sections of this chapter, the electrode gap should be as large as possible to allow the VUV radiation to pass through without scattering. Furthermore, the previous electrostatic lens design following Wrede *et al*. seemed rather complicated. Therefore, we tested the conventional three-electrode design by Epping and Parker,[4] which is widely used in charged particle imaging. The advantage of the Wrede design over the Eppink/Parker design was reduced chromatic and spherical aberrations. The Eppink/Paker design consisted of a repeller, extractor and ground electrode. The repeller voltage V_{rep} primarily determines the image size on the detector and is usually set to maximize the radius of the image. The extractor voltage V_{ext} is carefully adjusted to focus electrons with the same initial velocity vector onto the same point on the imaging detector, as shown in Fig. 3.8 (a). If all photoelectrons are created at a point, high-imaging resolution is easily achieved. However, in reality, they are produced within a finite volume defined by the overlap of the molecular and photon beams. The shape of the electron source is approximately cylindrical, as depicted

in Fig 3.8 (b). In the case of He(I) experiment, the molecular beam (x-axis) and VUV light beam (y-axis) were respectively 8.5 and 4.2 mm in diameter at the interaction region. Since the diameter of VUV beam and molecular beam are different, the shape of the ionization region is asymmetric. This asymmetry results in slightly different focusing for the parallel (y-axis) and perpendicular (z-axis) direction with respect to the VUV beam axis in the imaging plane; the υ_y resolution is altered by the width of the molecular beam. Notice that the velocity resolution is defined as $\Delta R/R$, where R is the radius of the image and ΔR is the width of the distribution. In order to achieve the highest resolution possible, while minimizing the difference between the υ_y and υ_z resolution, we ran electron trajectory calculations on a personal computer with the SIMION 3D software package (Scientific Instrument Services). We assumed the outer diameter of electrodes to the maximum possible value (170 mm). Figure 3.9 shows the velocity resolution ($\Delta\upsilon/\upsilon$) in two directions (υ_y, υ_z) and their difference as a function of the electrode gap. We found a larger gap provides a higher resolution in both directions, and the resolution difference was minimized with the spacing of 39 mm and the outer diameter of 170 mm. The inner diameter of the electrode was optimized to be 60 mm for the fixed electrode spacing of 39 mm, as shown in Fig. 3.10.

The dimensions of the optimized electrostatic lens are shown in Fig. 3.11. The electrodes are 0.5-mm-thick stainless steel plates of 170 mm in diameter mounted with 39-mm-length insulator spacer (polyimide-CEPLA). The inner holes in the extractor and the ground electrode are 60 mm, and the repeller electrode contains a small hole (5 mm dia.) for propagation of the molecular beam. Figure 3.12 shows the velocity resolution as a function of V_{ext}/V_{rep} calculated for He(I) and FEL experiment. The molecular beam diameter was estimated to be 5.8 mm, and the diameter of He(I) and FEL were respectively 4.2 and 0.1 mm in diameter. At the optimal ratios of V_{ext}/V_{rep}, the best velocity resolutions of υ_y and υ_z are 2.7 % and 2.2 % for He(I) case; 0.06 % and 0.01 % for FEL case. The broad focusing curve and poor resolution in He(I) PEI is attributed to its large ionization volume.

Figure 3.13 (a)-(c) shows the photoelectron images of Ar measured with the three-electrode design. A repeller electrode had punching holes, and the overall open area was 20 %. The background signal was quite high, and the background component could not be eliminated by subtraction of the background image from the signal image (see Fig. 3.13(c)). The shape of the background signal is symmetric and did not change with the repeller voltage, which implied that those photoelectrons do not have the velocity components in the imaging plane. Therefore, the background photoemission must be arising from the repeller plate. We replaced the repeller with a mesh (open area = 88 %) and succeeded in reducing the background signal level. The mesh reduced the cross-section of the electrode by one order of magnitude compared with a solid plate, which suppresses background photoemission from this electrode; however, the background feature could never be eliminated by subtraction of the background image from the signal image, as shown in Fig. 3.13 (d)-(f).

3.2.2 A new electrostatic lens

Based on the experimental results presented above, I designed new electrodes. The basic features of this new design are summarized as follows.

1. The repller is made with mesh and placed away from the ionization region.

2. A small retardation field is added to prevent photoelectrons from the mesh transmitted to the acceleration region.

3. Electrons are gradually accelerated in a long distance to achieve high energy resolution.

The dimensions of the electrostatic lens system (outer diameter, inner diameter, and spacing of the electrodes) were optimized by running electron trajectory calculations with the SIMION 3D software. Figure 3.14 shows the final design of the new lens system. A stack of 8 circular electrodes is rigidly held by insulating supports, and the position of each electrode

plate was fixed by four sets of insulator screws and nuts. The electrode No. 1 is made with a high-transmission (90 %) mesh (70 wires/inch) with a 6-mm-diameter hole in the center for the molecular beam to pass through. The negative voltage of this electrode is set slightly smaller in magnitude than that of the electrodes No. 2 and 3 (see Fig. 3.14). This retardation field prevents photoelectrons produced by stray light of VUV radiation from being transmitted towards the detector. Figure 3.15 shows simulated electron trajectories emitted from the mesh electrode started from six different starting positions spaced 10 mm apart with 5 different ejection angles spaced by 45° (red, blue and orange curve). In order to enhance the visibility of the trajectories, the kinetic energy of each electron was set to 200 eV. In Fig. 3.14, the role of the electrode No. 1 is to shield the system from the ground potential of the bulkhead of the molecular beam source. The electrode No. 2 is held at the same voltage as the electrode No. 3 to avoid the field distortion caused by the large central hole in the electrode No. 3. We refer the electrodes Nos. 3 and 4 as a repeller and an extractor, respectively. Voltages were independently applied to electrodes Nos. 1 to 4 using a computer-controlled multi-port power supply (MBS, A-1 Electronics; ±12 kV max), whereas the other electrode voltages were passively regulated by a register (22 MΩ) chain placed outside the vacuum chamber. The gradual change in the voltages applied to electrodes 4-8 achieved energy resolution ($\Delta E/E$) higher than 1% even for a large ionization volume (several millimeters in length of each side of cylinder). The entire assembly can withstand voltages up to 12 kV.

3.2.3 Molecular beam diameter and velocity resolution

The difference in diameter between molecular beam and VUV beam leads to different resolution in υ_y and υ_z. As the diameter of VUV beam (4.3 mm) could not be altered easily, the molecular beam diameter was reduced. Figure 3.16 shows the simulated υ_y and υ_z velocity resolutions as a function of the ratio between the molecular beam and the VUV beam diameters. When the molecular beam diameter is larger than VUV beam diameter (skimmer

diameter > 1 mm), the cylindrical symmetry axis is along the VUV beam propagation axis (y-axis), as indicated in Fig. 3.16. On the other hand, when the molecular beam diameter is smaller than the VUV beam diameter (skimmer diameter < 1 mm), the cylindrical symmetry axis is along the molecular beam propagation axis (x-axis) that is perpendicular to the MCP surface. As anticipated, when the molecular beams is smaller than the VUV beam in diameter, the υ_y and υ_z resolution are essentially the same. In the actual experiment, I used the 0.8-mm diameter skimmer and created the molecular beam diameter of 3.4 mm at the ionization region. Figure 3.17 shows the velocity resolution simulated as a function of V_{ext}/V_{rep} for both He(I) and FEL. In He(I) case, at the optimal ratios of V_{ext}/V_{rep}, the velocity resolutions of 0.25 % in y-axis and 0.24 % in z-axis are achieved. In FEL case, the diameter of a focused laser beam of ~ 0.1 mm provides the best speed resolution of 0.04 % in y-axis and 0.019 % in z-axis.

3.2.4 Distortion of the photoelectron image

The photoelectron image of Ar measured with this new set of electrodes is shown in Fig. 3.18. Comparing with Fig. 3.13, the background signal was suppressed considerably, and it could be removed completely by subtracting a background photoelectron image. However, the image in Fig. 3.18 is slightly distorted. First I have suspected imperfect alignment of electrode stack; for example, electrode plates are not parallel to each other. I have realigned the electrode stack several times, and I replaced the components with those of higher precision; however, the image was still distorted, as shown in Fig. 3.19(d). During this process, I found that the way of the distortion changed every time I opened the chamber, which strongly suggested that distortion was caused by charging of the insulators.

In order to examine the effect of insulator charging on PEI, 3-D trajectory calculation of electrons was performed. Figure 3.20 (a) shows the 3-D configuration of the lens with a charged insulator placed between the repeller and the extractor electrode plate. In the

simulation, I considered only the electrons with the initial velocities parallel to the detector plane. Figure 3.20 (b) shows the simulated images on the MCP detector (X-Y plane) expected for the following three conditions: (i) no charged insulator; (ii) an insulator at a negative potential of -3424 V (same as V_{ext}); (iii) an insulator at a negative voltage of -2000 V. The result shows that a charged object can cause distortion in a similar way with the observed one. With a larger voltage difference between the insulator and extractor electrode, larger distortion occurred. Similar distortion was observed when the charged insulator was placed between the electrode Nos. 6 and 7, as shown in Fig. 3.21. The distortion was negligible when a charged object was placed between the electrodes Nos. 1 and 3. Thus, I concluded that the observed distortion was caused by charging of the insulators.

3.2.5 The final design of electrostatic lens

The final design and dimensions of the electrodes are shown in Figure 3.22. The stack consists of 12 circular electrodes. All elements except the first two electrodes are thick rings spaced with 3-mm-diameter ruby balls, and they hide the insulating supports from stray light and electrons. Electrodes 3 to 5 were referred as the repeller, light port, and extractor, respectively. Two 40 × 35 mm square holes in the light port allow incoherent He(I) radiation to propagate with minimal scattering. The negative voltage of electrode No. 1 is set slightly lower in magnitude than that of the electrodes No. 2 and 3, and the electrode No. 2 is held at the same voltage as No. 3. Voltages were independently applied to electrodes 1 to 5 and other voltages were regulated by a register chain. As shown in Figure 3.23, the best speed resolution was 0.36 % in both directions in the imaging plane. Using trajectory calculations, I examined the effect of the number of electrodes in the acceleration region on the resolution. The geometry of the lenses was slightly simplified by removing the port electrode, as shown in Fig. 3.24 (a). Without the port electrode, the velocity resolution was slightly improved from 0.36 % to 0.25 %. As shown in Fig. 3.24 (b), the velocity resolution was generally higher at a

larger number of electrodes; however, it was practically saturated at 7 electrodes. Here we count the number of electrodes behind the extractor (lens No. 5): for instance, the electrodes shown in Fig. 3.22 are 12 in total but the number of electrodes behind the extractor is 7 (No. 6–12). Figure 3.25 shows the photoelectron image of Ar with a new lens set, which exhibits no distortion.

3.2.6 Chromatic aberration

In the above discussion, we optimized the electrode voltages (V_{port}/V_{rep} and V_{ext}/V_{rep}) to achieve the best energy resolution for a certain electron kinetic energy. However, the electron lens generally has some finite chromatic aberration in that the electrons with different initial kinetic energies receive different focusing by the lens. Then, the energy resolution is determined not only by the spatial resolution of the imaging system but also the chromatic aberration of the lens. Notice that chromatic aberration of an electrostatic lens can only be minimized and not eliminated.[5] I found that the soft focusing in the acceleration region can alleviate chromatic aberration. I have checked chromatic aberration of our newly designed electrode (see Fig. 3.22) with various number of lens electrode behind the extractor. Similar to the previous section, the port electrode was removed to simplify the voltage optimization procedure (see Fig. 3.24 a). Figure 3.26 compares the calculated energy resolution (ΔE) as a function of the electron kinetic energy (eKE) for our newly designed electrode with different number of lens electrodes. In all cases, the focusing conditions were optimized for a repeller voltage of -4000 V and eKE of 5.461 eV. Electrons were ejected from the region of ionization volume (3.4 o.d. × 4.2 mm) with the angles of 90° with respect to the flight axis. The figure shows that chromatic aberration reduces as more lens electrodes are employed. Similar calculation with the conventional three-electrode design (see Fig. 3.11) is also shown in Fig. 3.26 (open green triangle), the result of conventional three-electrode approaches to the result of newly designed electrode with two lens electrode which is difficult to focus electrons with

high eKE. It clearly demonstrates the advantage of our design over the three electrodes.

3.2.7 He(I) PEI of rare gases with a new lens set

(A) Velocity resolution

The performance of our electrostatic lens was examined by He(I) PEI of Kr using a CCD camera (512 × 512 pixels) without COG calculations. PKED observed at the optimal ratios of V_{port}/V_{rep} and V_{ext}/V_{rep} is shown in Fig. 3.27. The spin-orbit splitting of Kr (0.665 eV) is clearly resolved. As shown in the inset, the least-squares fit using a Gaussian function indicated the full width at half maximum (FWHM) of 210 meV at 7.22 eV, corresponding to the energy resolution $\Delta E/E$ (= $2\Delta\upsilon/\upsilon$) of 2.9 %. Figure 3.28 shows the energy resolution determined by PEI of Kr as a function of V_{ext}/V_{rep} with V_{rep} = -5000 and V_{port} = -4319 V; the optimum voltage of V_{port} was determined experimentally. It is seen that the resolution varies only gradually with V_{ext}/V_{rep} within the range of ca. 30 V about the best point. This contradicts with a much sharper dependence on the voltage predicted theoretically, and it is attributed to insufficient imaging resolution. In order to evaluate the energy resolution more precisely, we used a super-resolution imaging system using a 4M-pixel CCD camera (2048 × 2048 pixels)[6]. The subpixel centroiding calculations down to a quarter pixel size achieved an effective imaging resolution of 4096 × 4096 pixels. The inset of Fig. 3.28 shows the energy resolution evaluated by PEI of Ar at fixed V_{rep} of -4000 V and V_{port} of -3464.8 V, respectively: the optimum V_{port} was determined experimentally. The energy resolution varied much more sensitively with V_{ext} in this case, and the resolution clearly degraded on both sides of the best point. The best voltage ratios were V_{port}/V_{rep} = 0.8662 and V_{ext}/V_{rep} = 0.8557, with which we obtained the energy resolution ($\Delta E/E$) of 0.735 % at 5.461 eV (FWHM: 40 meV) in excellent agreement with the trajectory calculations. The fine structure splitting of Ar was resolved, as shown in Fig. 3.29. The signal count level of He(I) PEI was very high, and I intentionally reduced the gain of MCP to perform COG calculations.

(B) Photoelectron angular distribution

The photoelectron angular anisotropy was evaluated independently for the four quadrants of one image, as shown in Fig. 3.30. For each quadrant, the anisotropy parameters (β) were determined for the $^2P_{3/2}$ and $^2P_{1/2}$ final states as shown in Fig. 3.30. The average of β determined from the four quadrants are 1.26 ± 0.04 and 1.22 ± 0.08 for $^2P_{3/2}$ and $^2P_{1/2}$, respectively, in which the errors are the standard deviations. We also determined β from a symmetrized image and obtained 1.24 ± 0.01 and 1.21 ± 0.01 for $^2P_{3/2}$ and $^2P_{1/2}$, respectively. The larger errors in the former approach result from non-uniform sensitivity of the imaging detector. The β determined by both methods are in good agreement with the literature value (1.24 and 1.21 for $^2P_{3/2}$ and $^2P_{1/2}$),1 which indicates that symmetrization of the raw image prior to analysis does not affect the anisotropy.

3.3 Conclusion

From experimental and computational examination of various designs of the acceleration electrodes, the following conclusions were drawn.

1. The major source of background electrons is the photoemission from the repeller plate. Therefore, the repeller plate should be placed away from the ionization region and a small retardation field may be applied to prevent photoelectrons emitted from the repeller to be transmitted to the acceleration region.
2. All insulators should be shielded to avoid charging.
3. Energy resolution ($\Delta E/E$) of higher than 1 % is obtainable even for a large ionization volume (i.e. of the order of millimeters). The acceleration electric field strength should be weak.

4. The resolution of an imaging system should be sufficiently high. In our case, a super-resolution (4096 ×4096 pixels) imaging system was needed to fully exploit the performance of our charged particle optics. The best energy resolution was 0.735 % at 5.461 eV (FWHM: 40 meV).

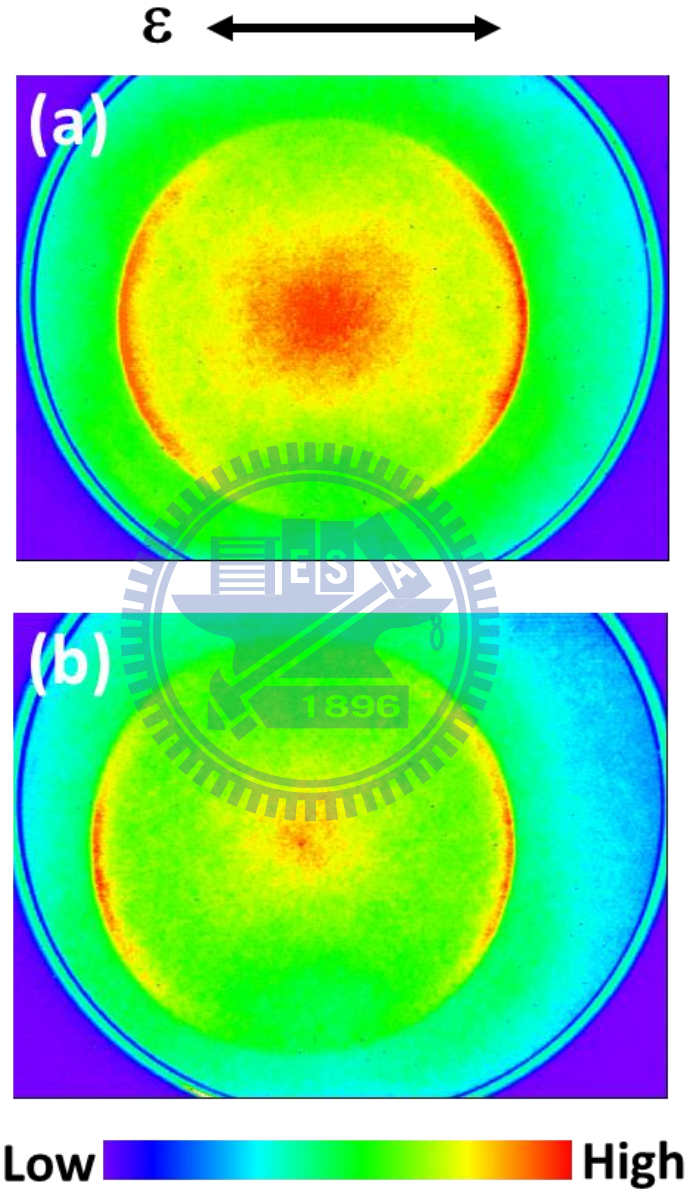

Figure 3.1 Photoelectron images observed by He(I) photoionization of a supersonic beam of Ar: (a) ϕ 6 mm aperture of He(I) light source was used. (b) ϕ 2 mm aperture of He(I) light source was used.

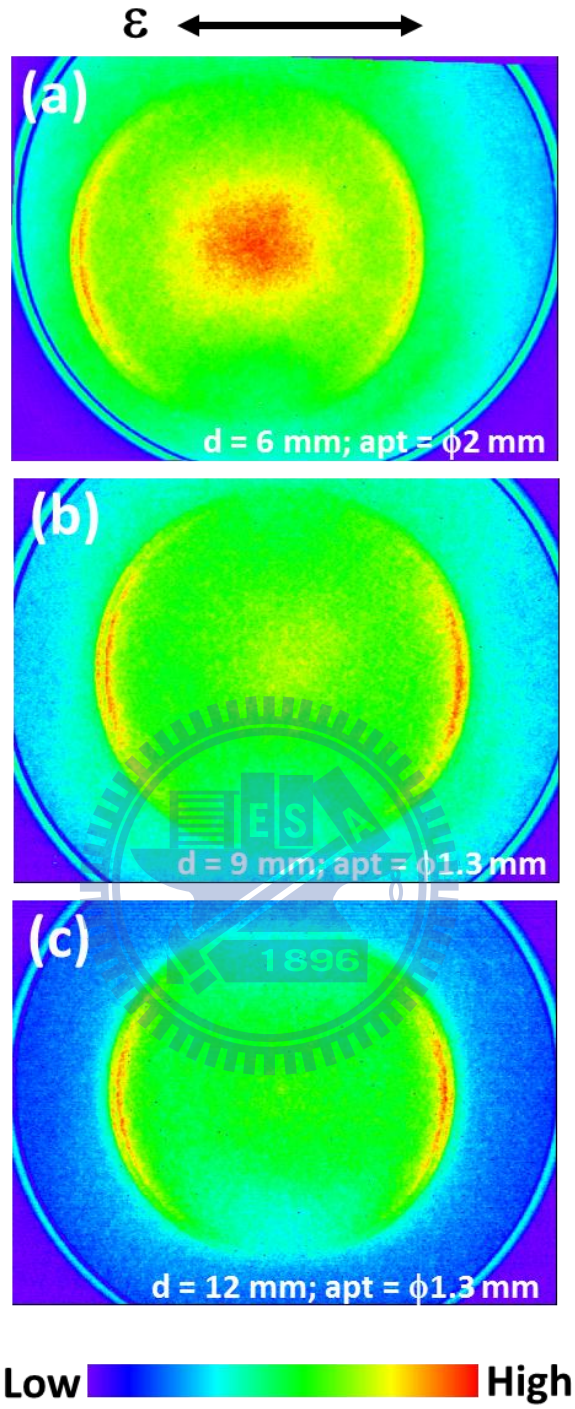

Figure 3.2 (a)-(c) Intensity-integrated raw photoelectron images of Kr at a stagnation pressure of 2.2 MPa at different electrode gap distance of 6 mm, 9 mm and 12 mm. (d denotes the electrode gap distance, apt denotes the aperture diameter of He(I) light source). ε denotes the directions of the polarization vectors of the VUV beam.

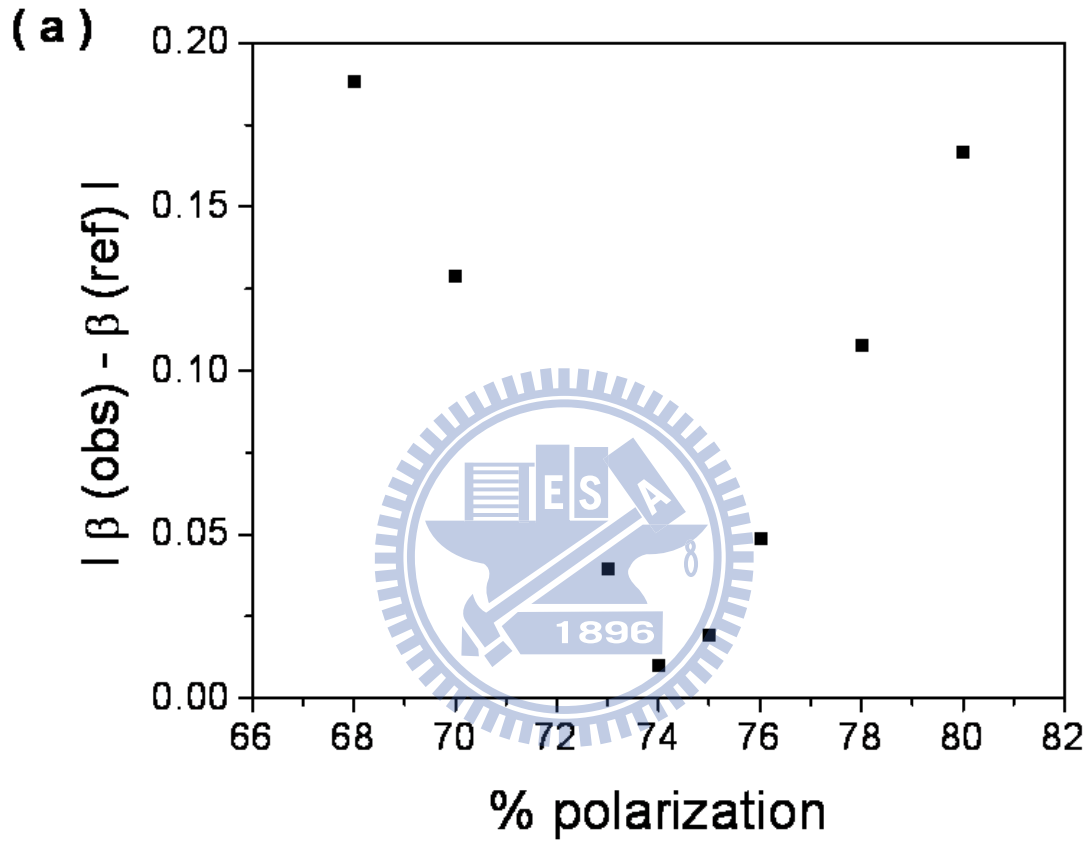

Figure 3.3 Difference between the anisotropy parameter β calculated for Kr ($^2P_{3/2}$) by assuming different polarization degrees of light and the literature value 1.24.[ref. 1] The polarization degree of 74 % provides the best agreement.

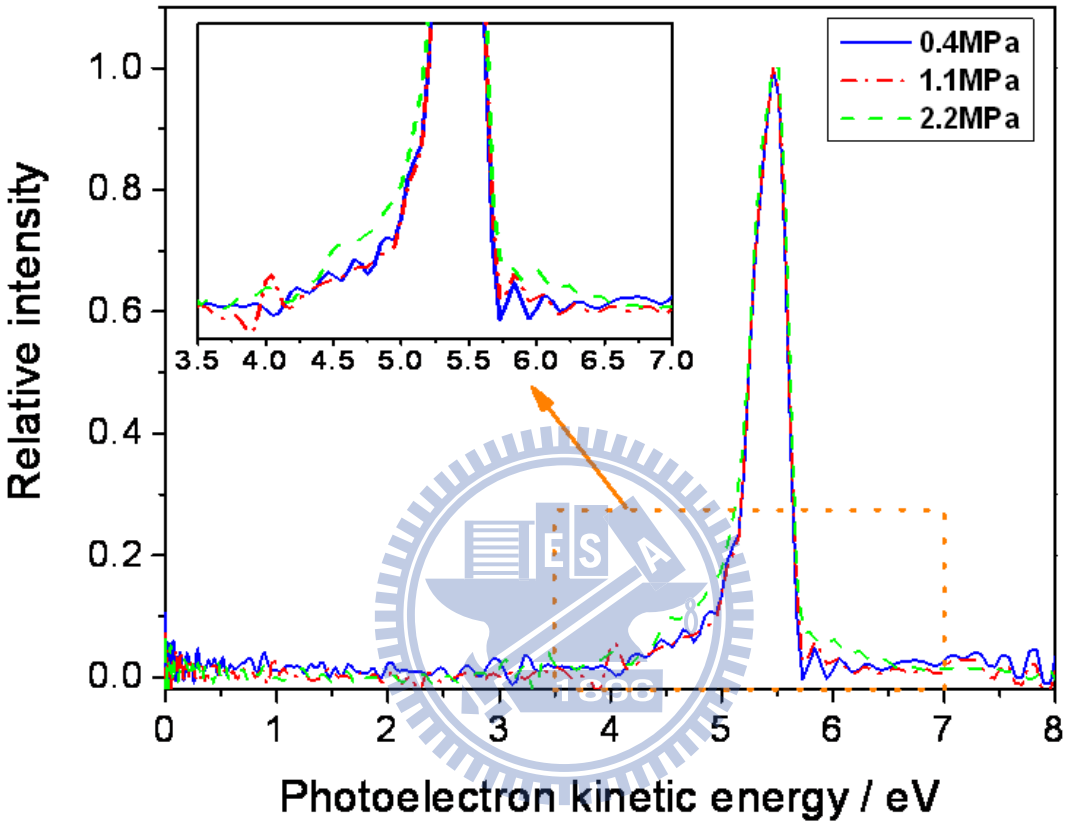

Figure 3.4 Photoelectron kinetic energy distributions in He(I) photoionization of supersonic beams of Ar generated at different stagnation pressures of 0.4 (solid), 1.1 (dash dot), and 2.2 (dash) MPa.

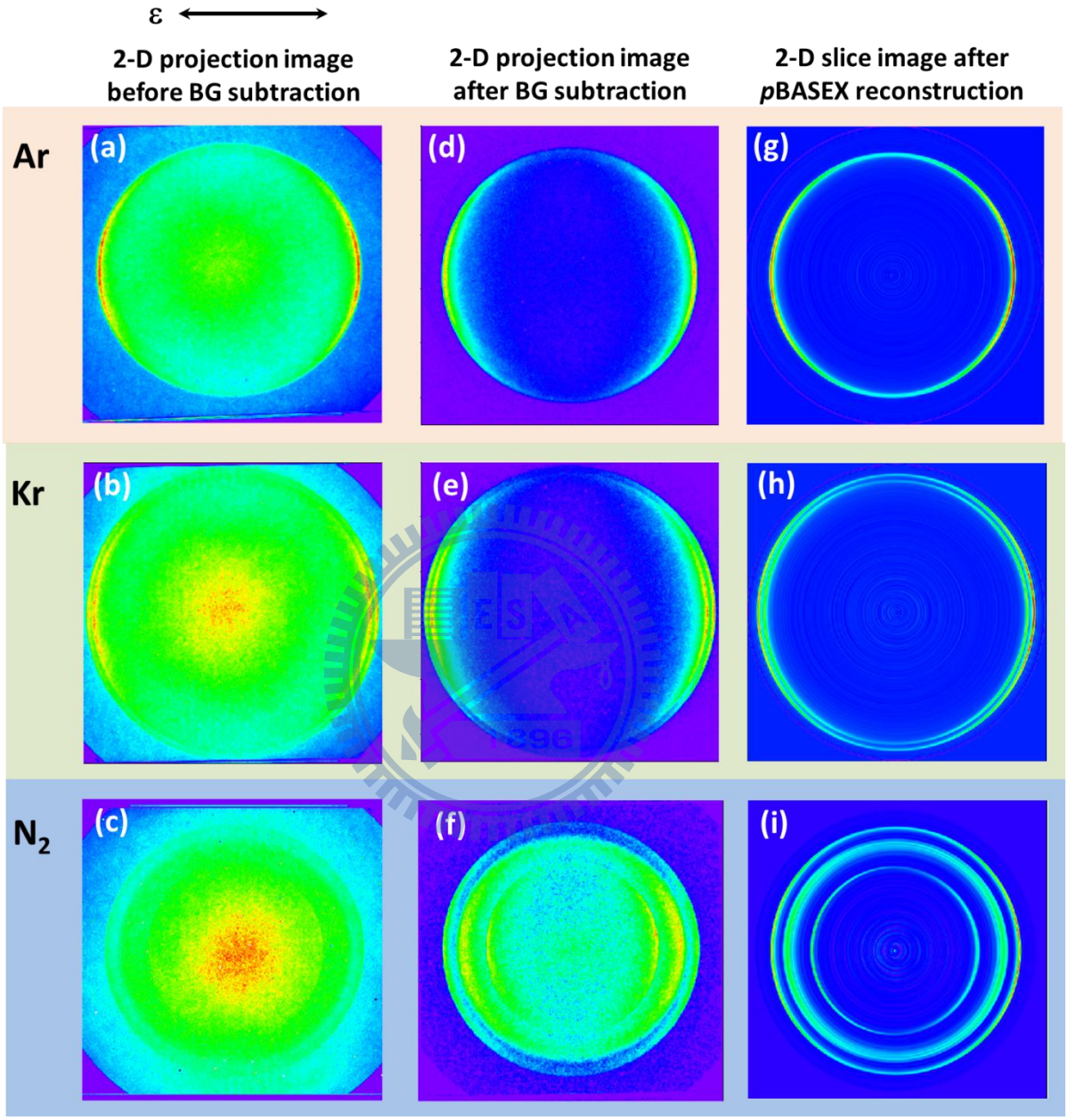

Figure 3.5 (a)–(c) Intensity-integrated raw photoelectron images observed by He(I) photoionization of a supersonic beam of pure Ar, Kr and N_2, respectively. (d)–(f) Photoelectron images of Ar, Kr and N_2 after background subtraction. (g)–(i) 2D slice images of Ar, Kr and N2 obtained with the modified *p*-BASEX reconstruction. ε denotes the directions of the polarization vectors of the VUV beam.

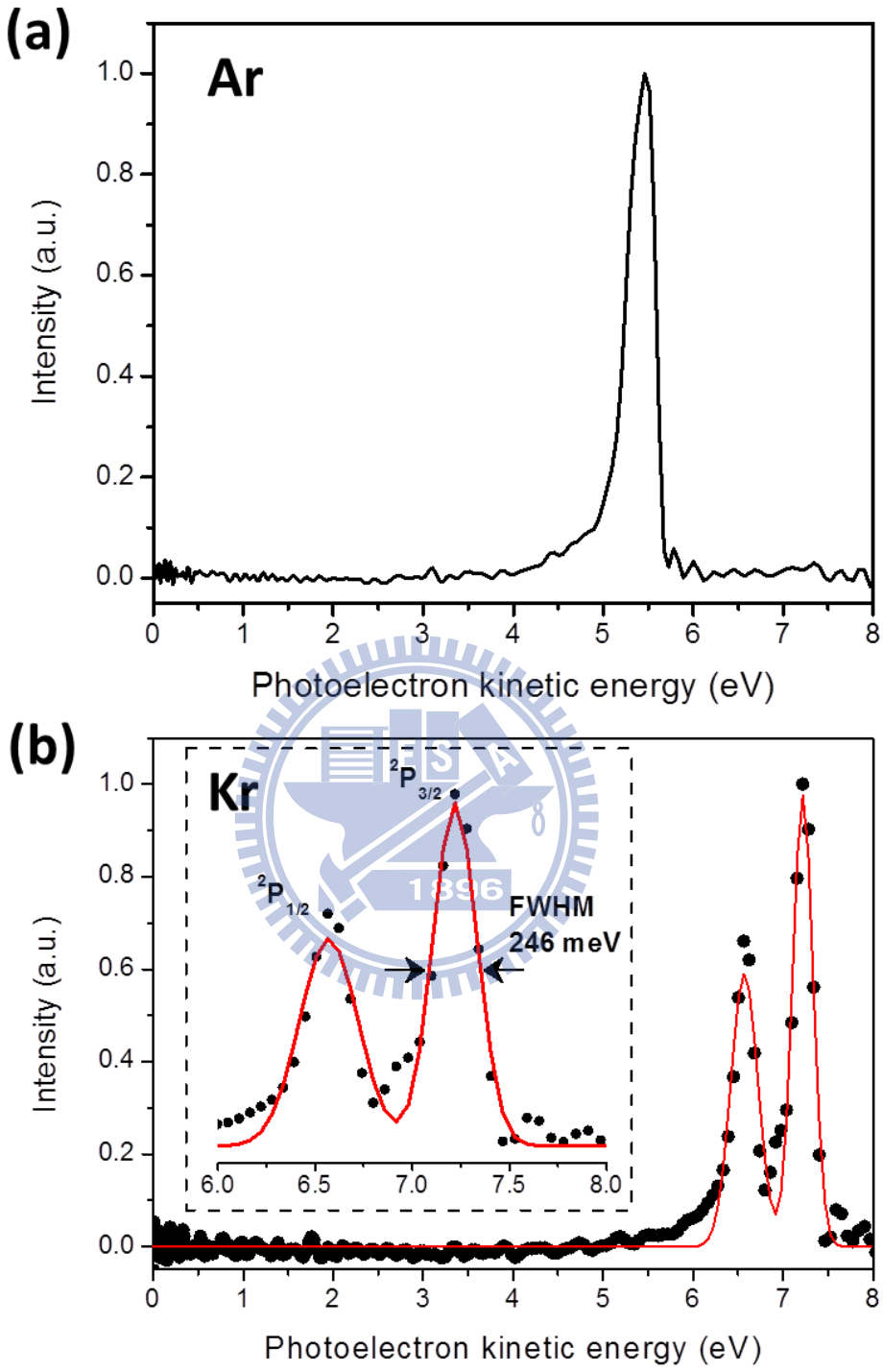

Figure 3.6 (a) Photoelectron kinetic energy distribution in He(I) photoionization of supersonic beams of Ar. (b) Photoelectron kinetic energy distribution in He(I) photoionization of supersonic beams of Kr. The inset shows an expanded view in the PKE region between 6.0 and 8.0 eV. The solid red line indicates the best-fit Gaussian to the observed data; it has a FWHM of 246 meV at 7.22 eV.

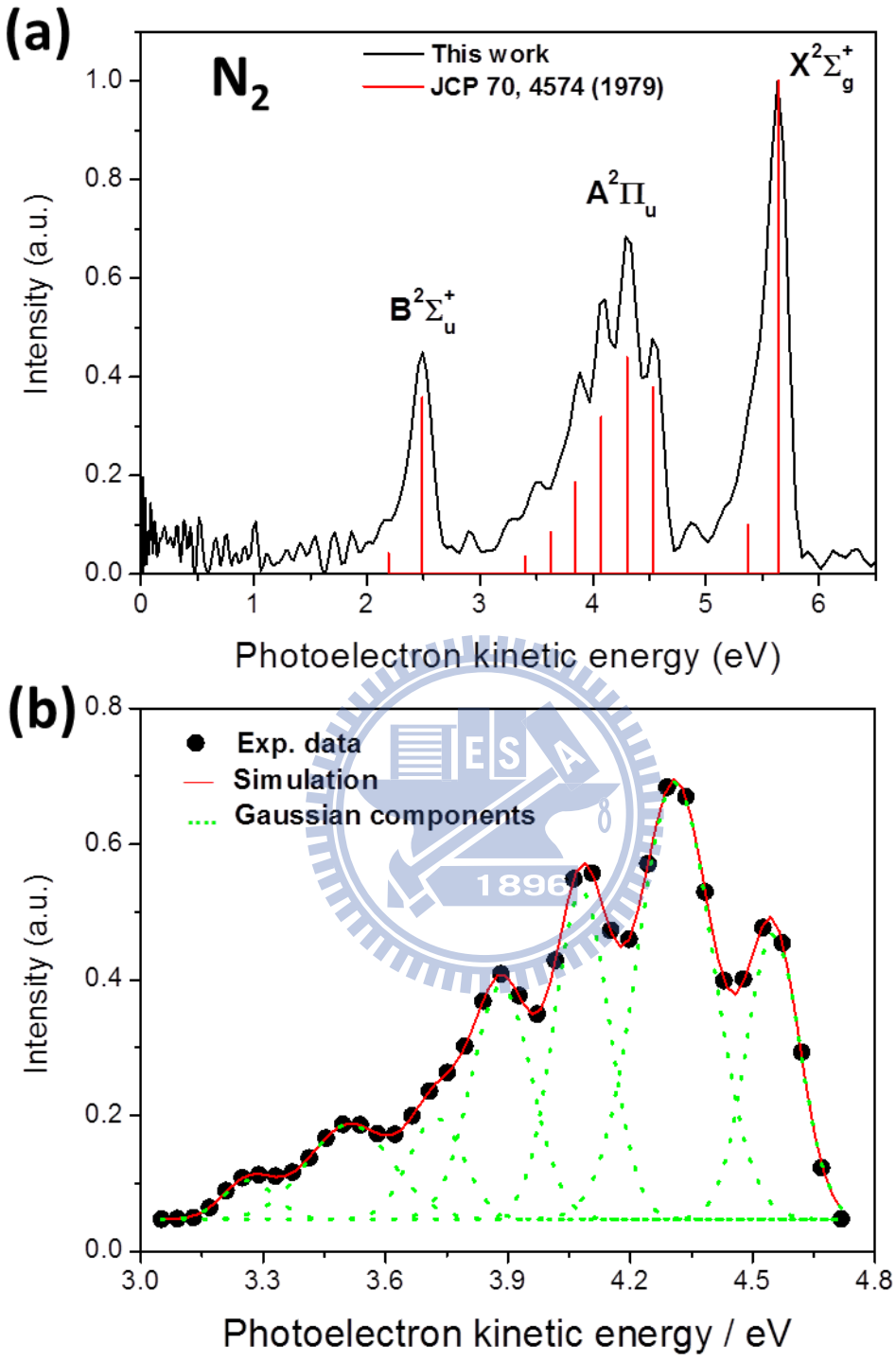

Figure 3.7 (a) Photoelectron kinetic energy distribution in He(I) photoionization of supersonic beams of N_2. The spectral feature agrees reasonable well with the literature [Ref. 3]. (b) Expanded view of He(I) photoelectron spectrum of N_2 in the A band region. The solid red and dotted green lines show the overall distribution and individual Gaussian components obtained by least-squares fitting.

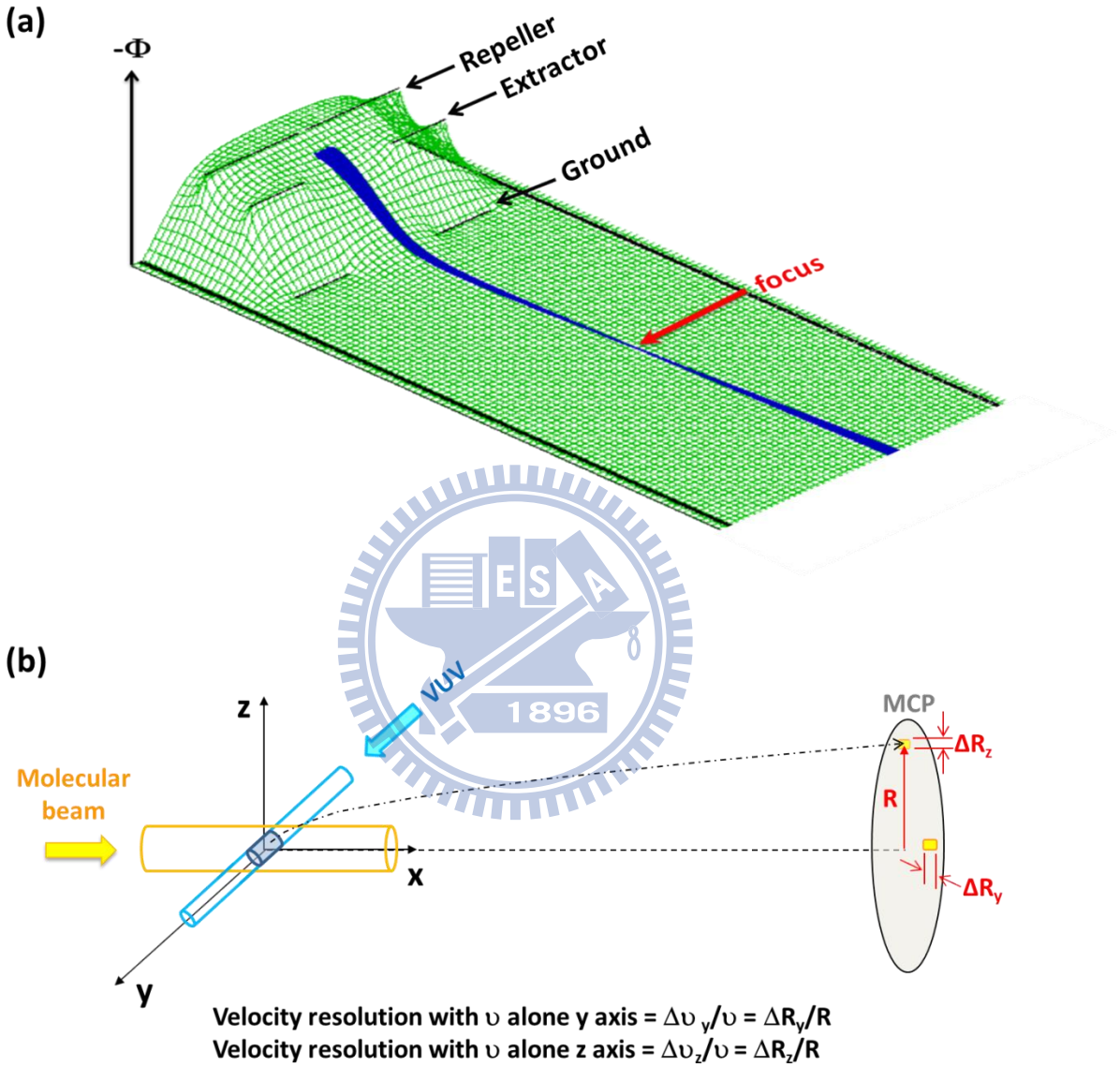

Figure 3.8 (a) 2D representation of the cylindrically symmetric potential Φ in the VMI spectrometer. (b) Experimental geometry for photoelectron imaging experiment. The molecular beam and time-of-flight axis are located along the x axes; VUV light beam is located along y axis.

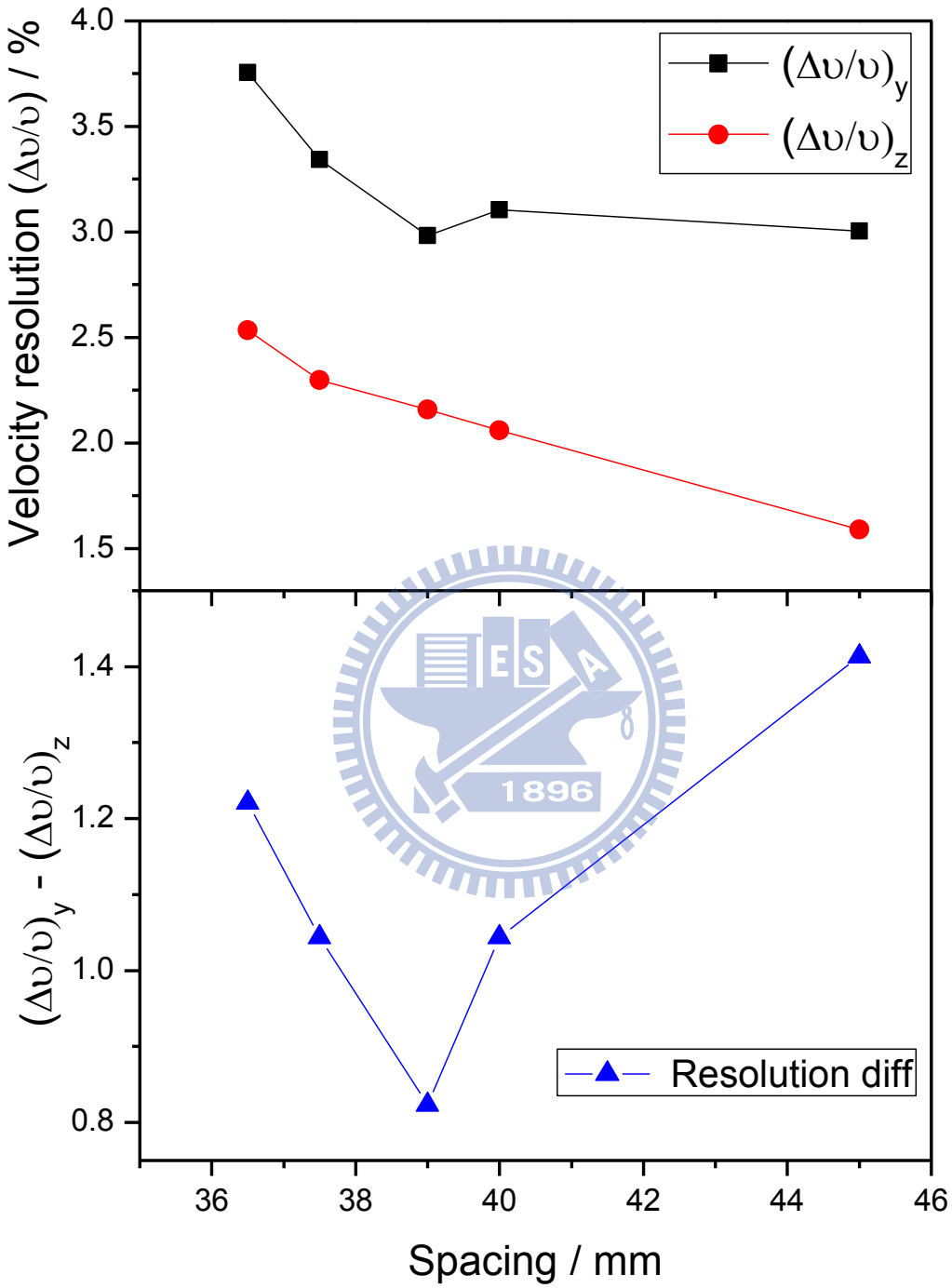

Figure 3.9 The simulated velocity resolution $(\Delta\upsilon/\upsilon)_y$ (black solid square) and $(\Delta\upsilon/\upsilon)_z$ (red solid circle) as a function of electrode spacing (upper panel) and the resolution difference $[(\Delta\upsilon/\upsilon)_y - (\Delta\upsilon/\upsilon)_z]$ (lower panel).

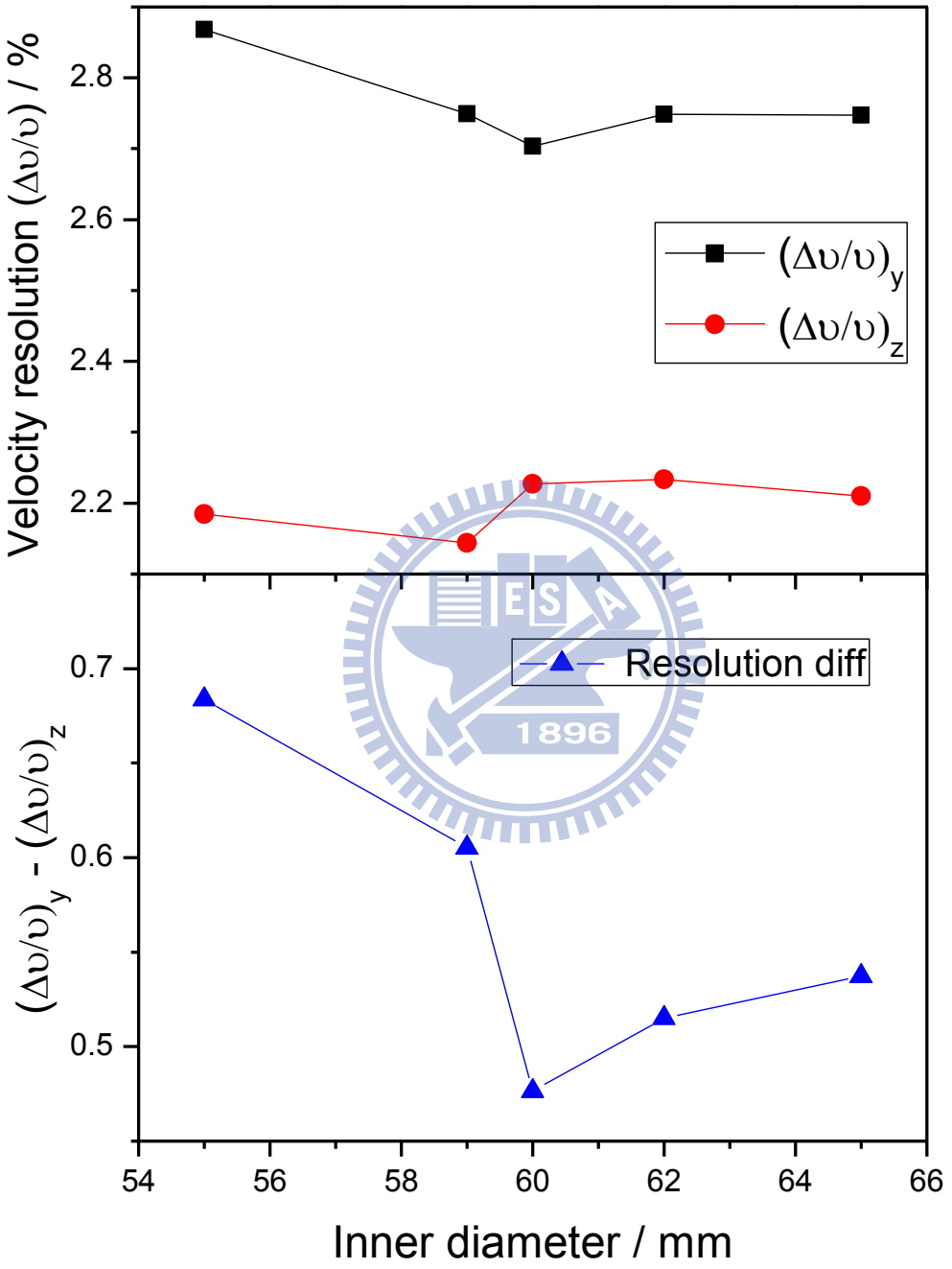

Figure 3.10 The simulated velocity resolution $(\Delta\upsilon/\upsilon)_y$ (black solid square) and $(\Delta\upsilon/\upsilon)_z$ (red solid circle) as a function of hole diameter (upper panel) and the resolution difference $[(\Delta\upsilon/\upsilon)_y - (\Delta\upsilon/\upsilon)_z]$ (lower panel).

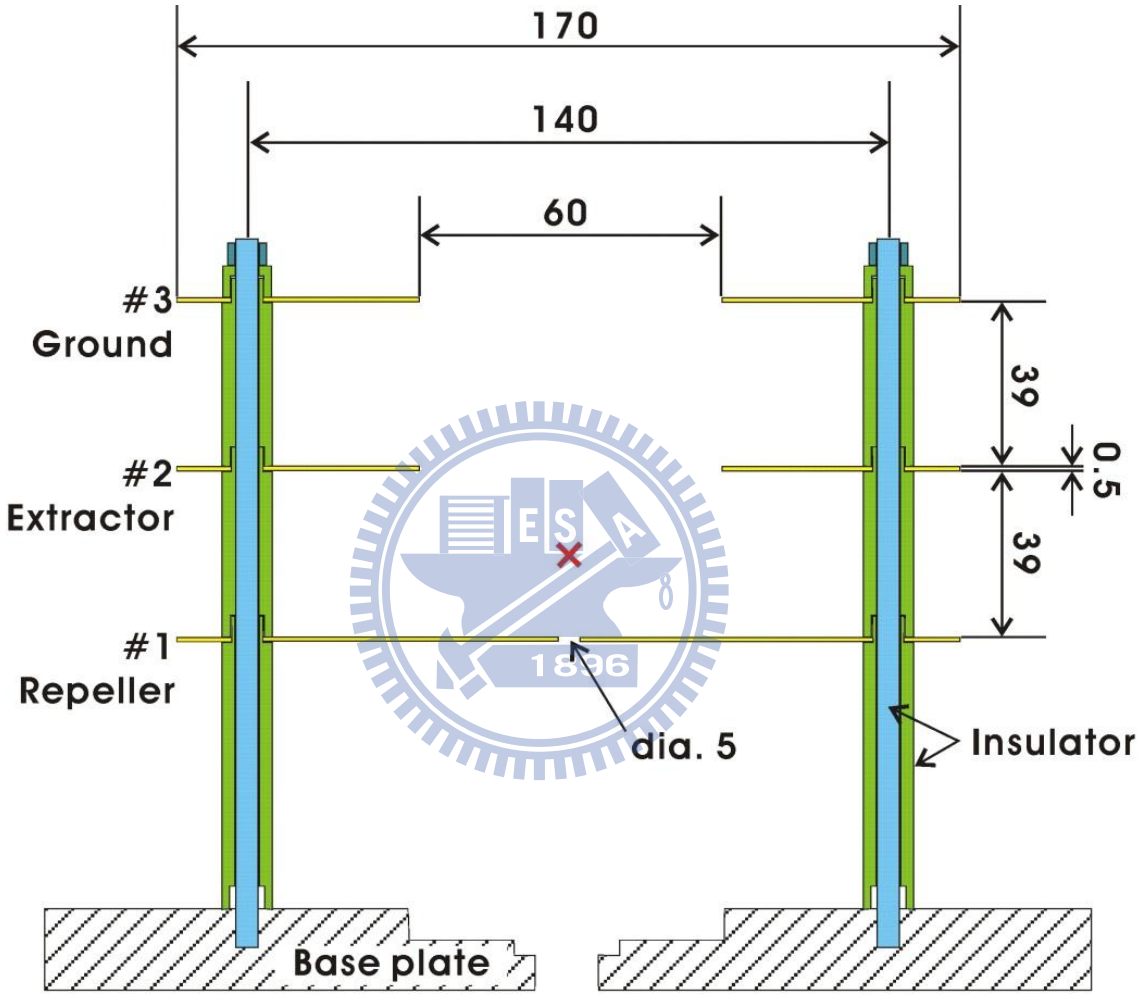

Figure 3.11 Cross-sectional view of the electrostatic lens system using three-electrode configuration (all units in millimeters). A molecular beam is introduced from the bottom and is irradiated by He(I) radiation at the position indicated by the cross (×).

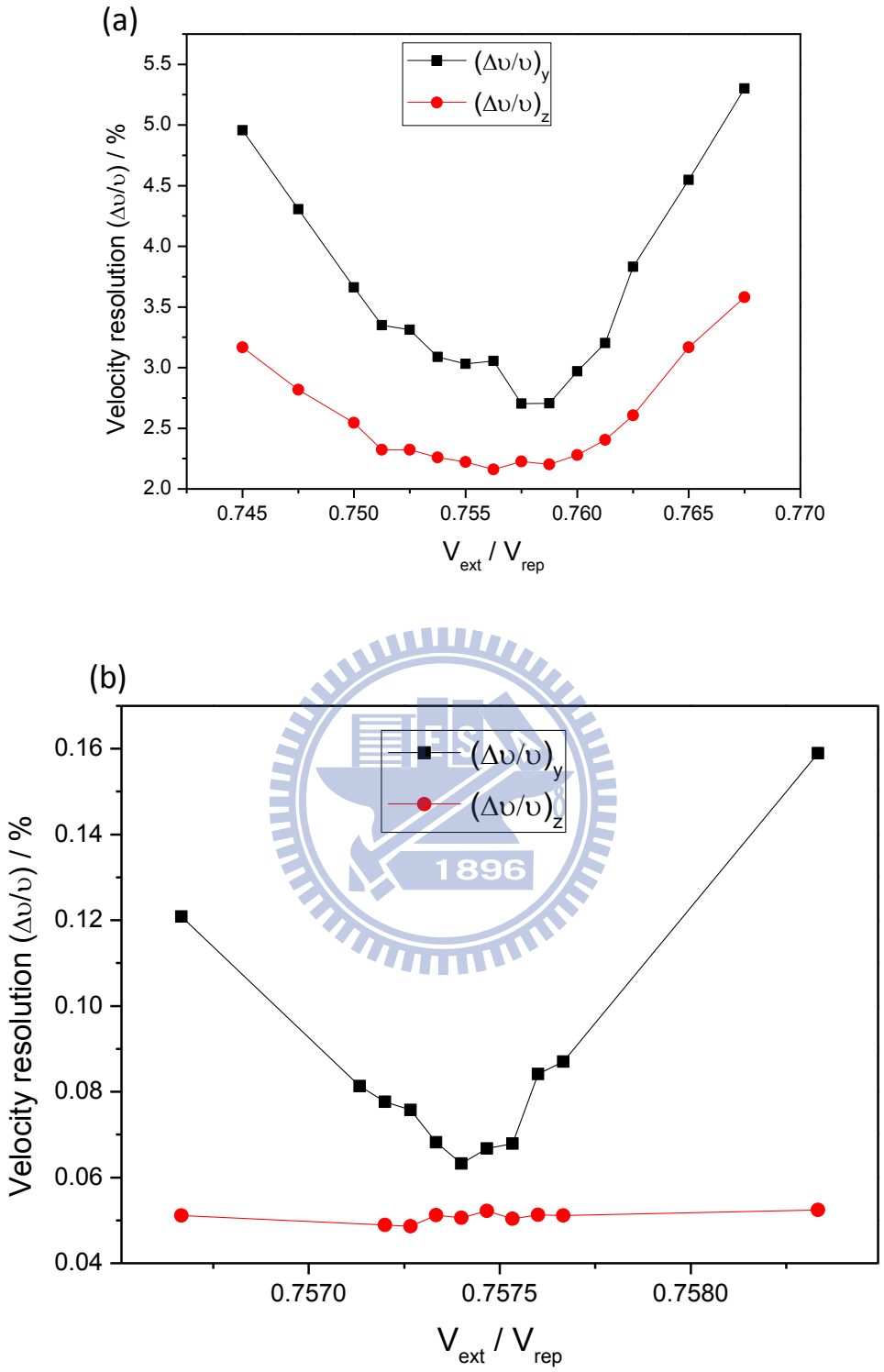

Figure 3.12 Velocity resolution simulated by performing trajectory calculation with 3D Simion software as a function of V_{ext}/V_{rep}: (a) He(I) experiment condition: light beam diameter = 4.2 mm. (b) FEL experiment condition: light beam diameter = 0.1 mm.

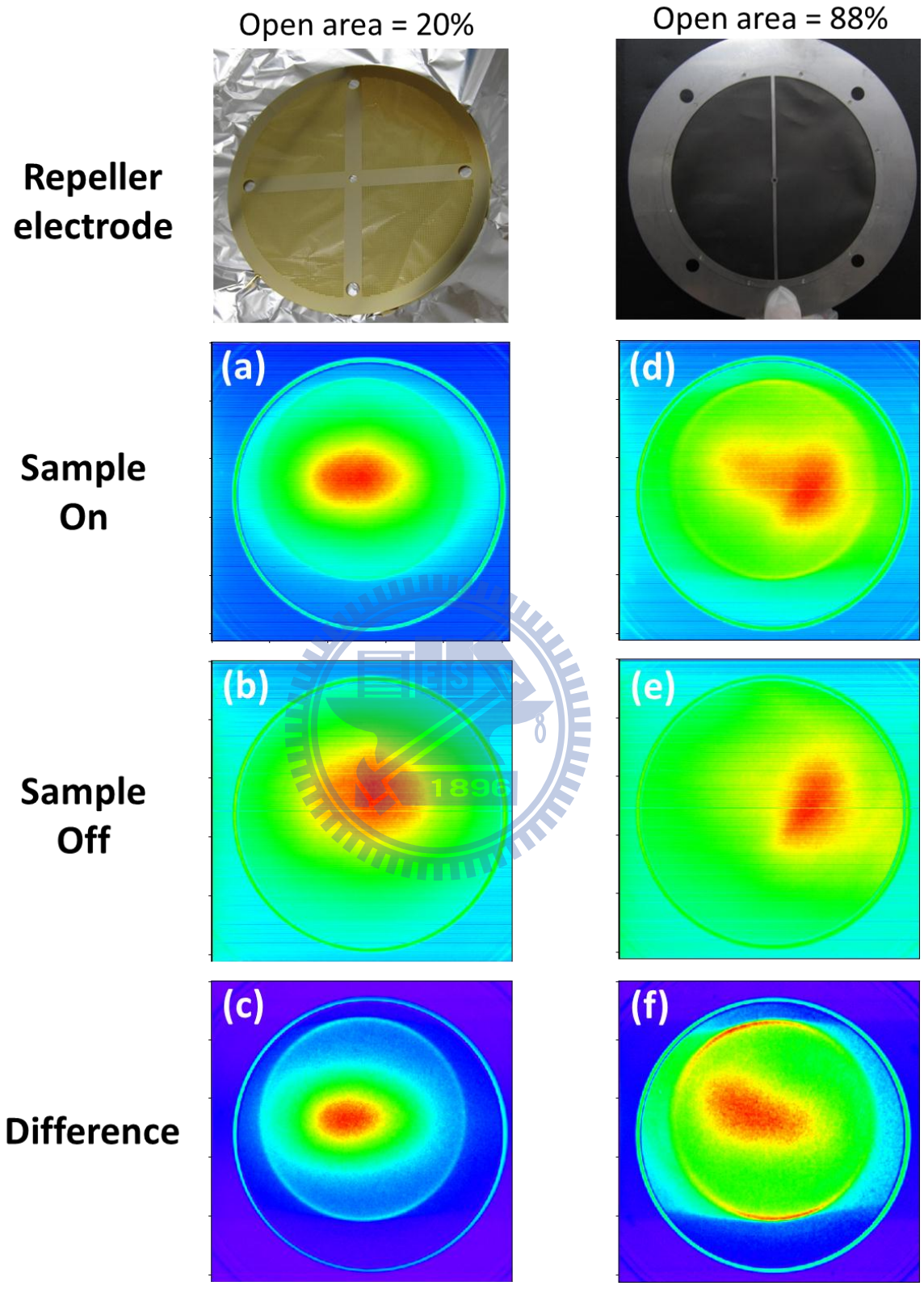

Figure 3.13 (a)-(c) Photoelectron images of Ar using the three-electrode configuration with solid repeller electrode. (d)-(f) Photoelectron images of Ar after replaced the solid repeller electrode to mesh repeller electrode.

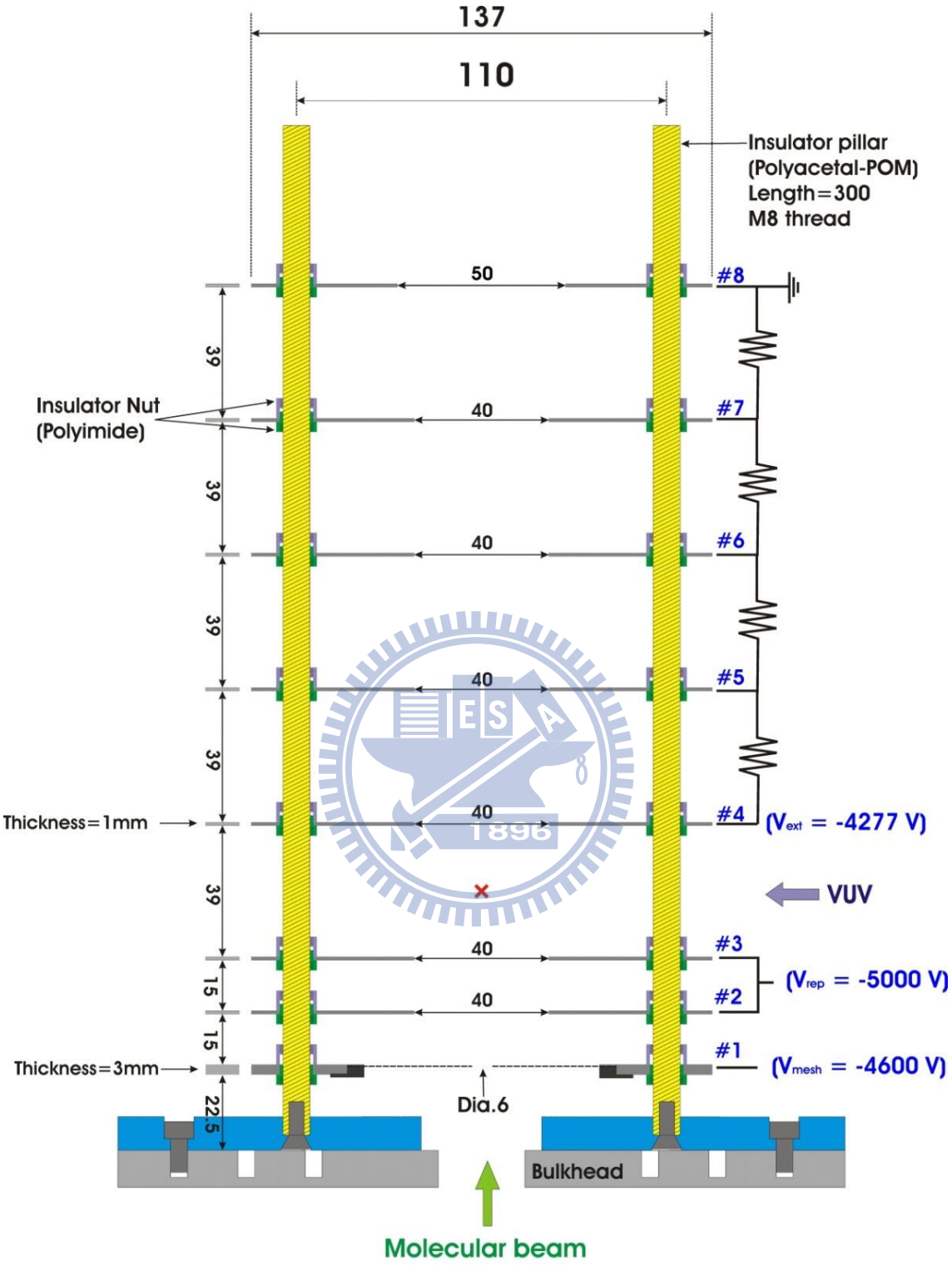

Figure3.14 Cross-sectional view of the electrostatic lens system (all units in millimeters). A molecular beam is introduced from the bottom and is irradiated by He(I) radiation at the position indicated by the cross (×). An example of the voltage setting in the measurement of photoelectron image of Kr is also shown in the figure.

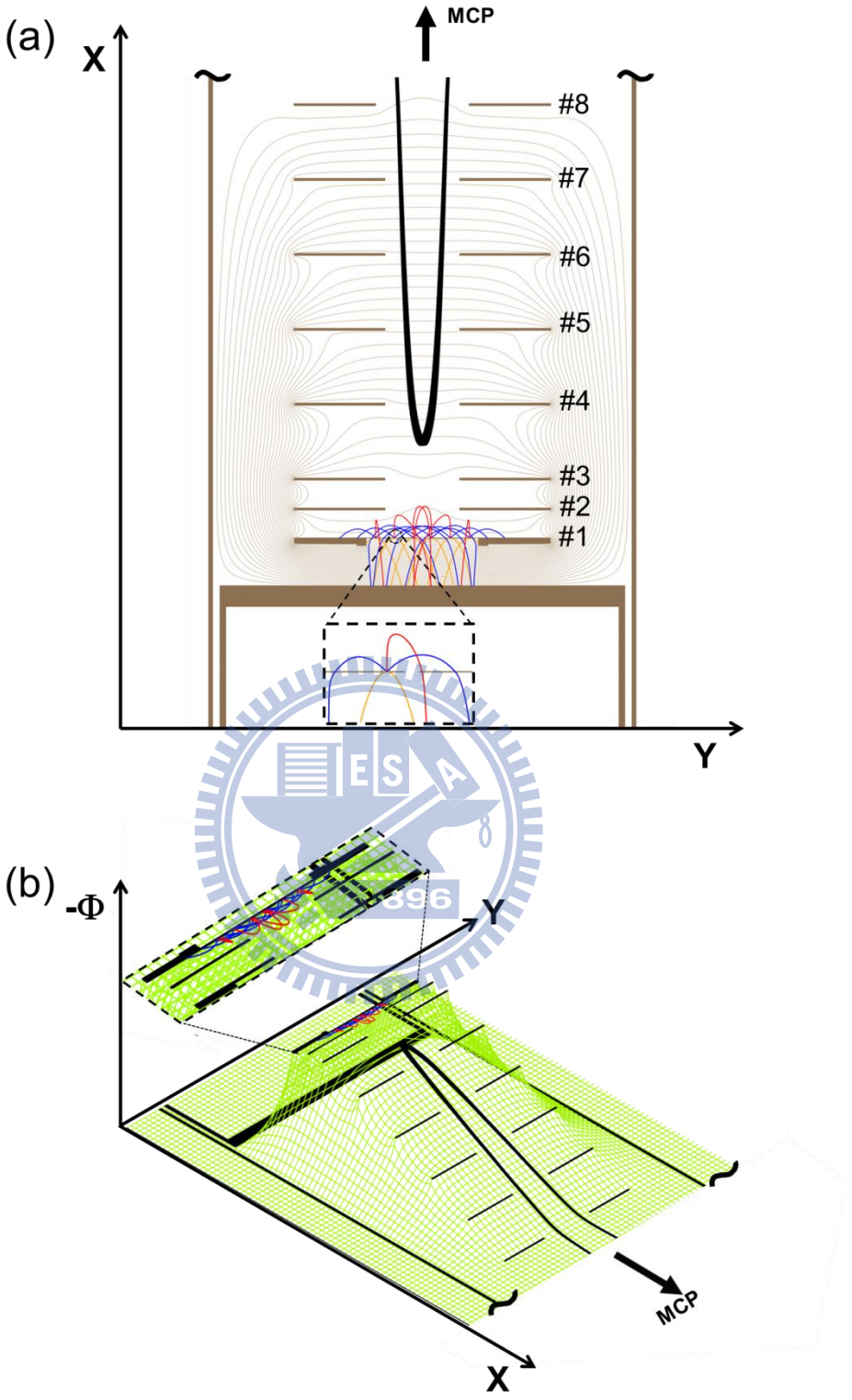

Figure 3.15 (a) Simulated trajectory (red, blue and orange) of electrons emitted from the mesh electrode and photoelectrons from the photoionization point (black). The equipotential lines are also shown (light brown). (b) 2D representation of the cylindrically symmetric potential Φ(x,y) of (a).

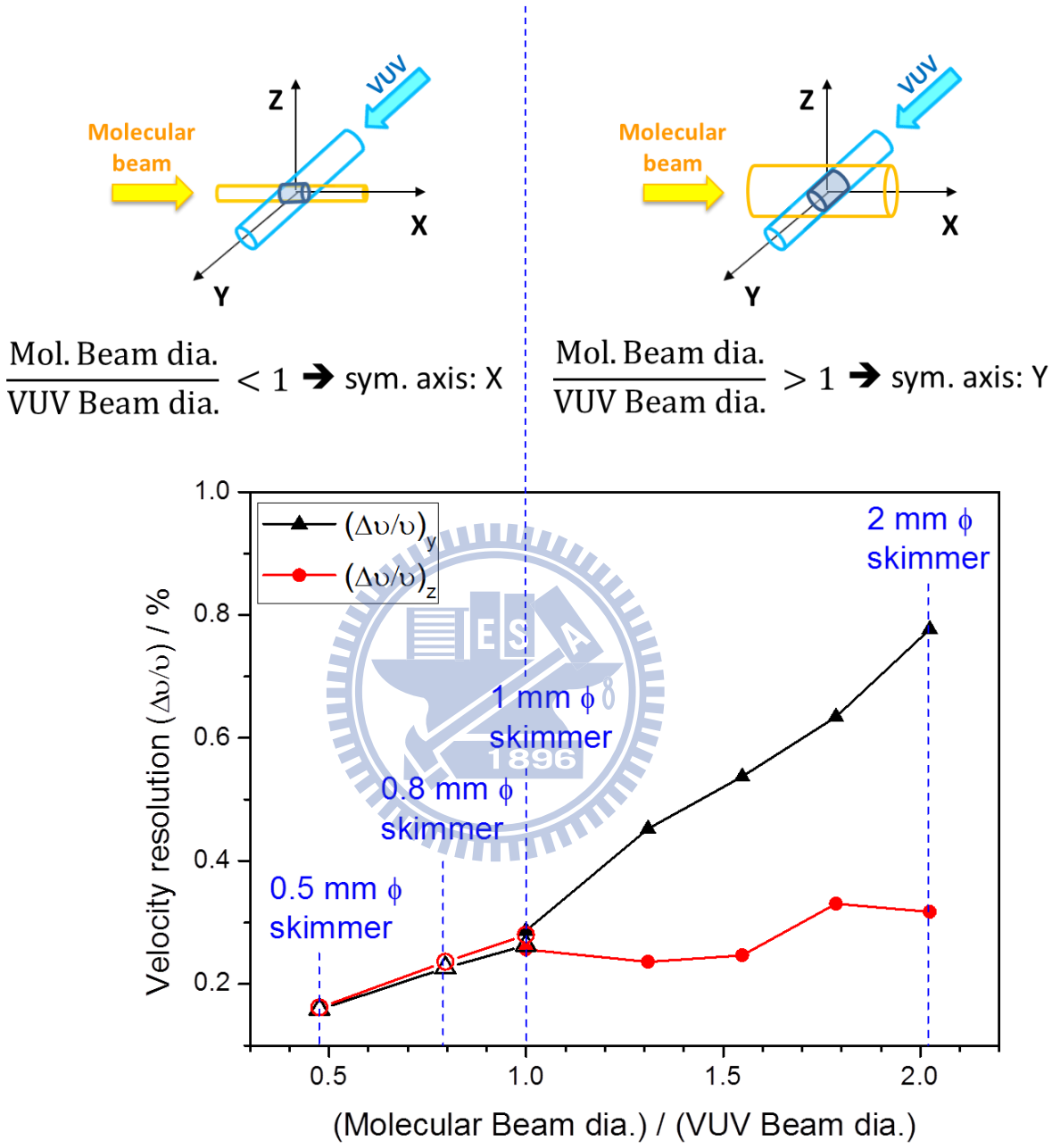

Figure 3.16 Velocity resolution simulated by performing trajectory calculation with 3D Simion software as a function of (molecular beam dia./VUV beam dia.) ratio and VUV beam diameter is fixed at 4.3 mm. Noted that solid symbol indicated the ionization volume aligned along the VUV beam axis (Y axis), open symbol indicated the ionization volume aligned along the molecular beam axis (X axis), as indicated at the top of the figure.

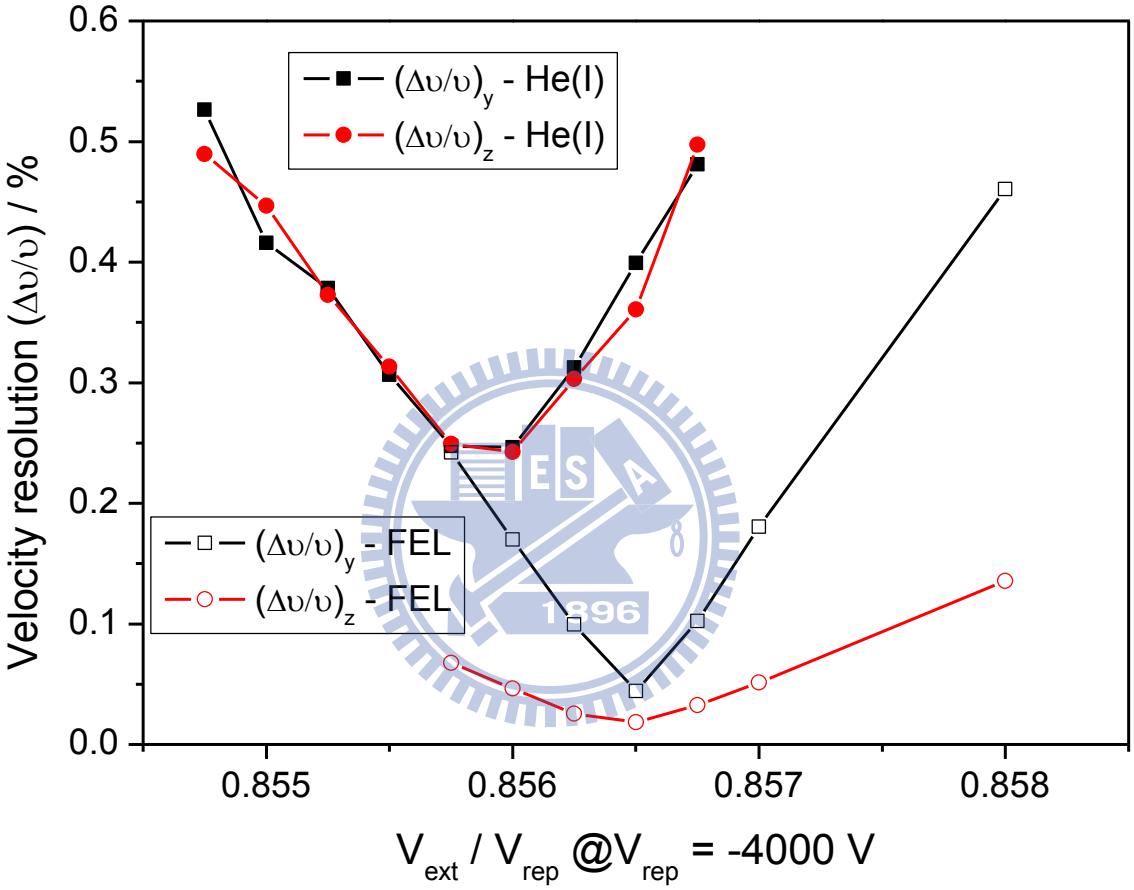

Figure 3.17 Velocity resolution simulated by performing trajectory calculation with 3D Simion software as a function of V_{ext}/V_{rep}: He(I) experiment with light beam diameter of 4.2 mm are indicated as solid symbol. FEL experiment with light beam diameter of 0.1 mm are indicated as open symbol.

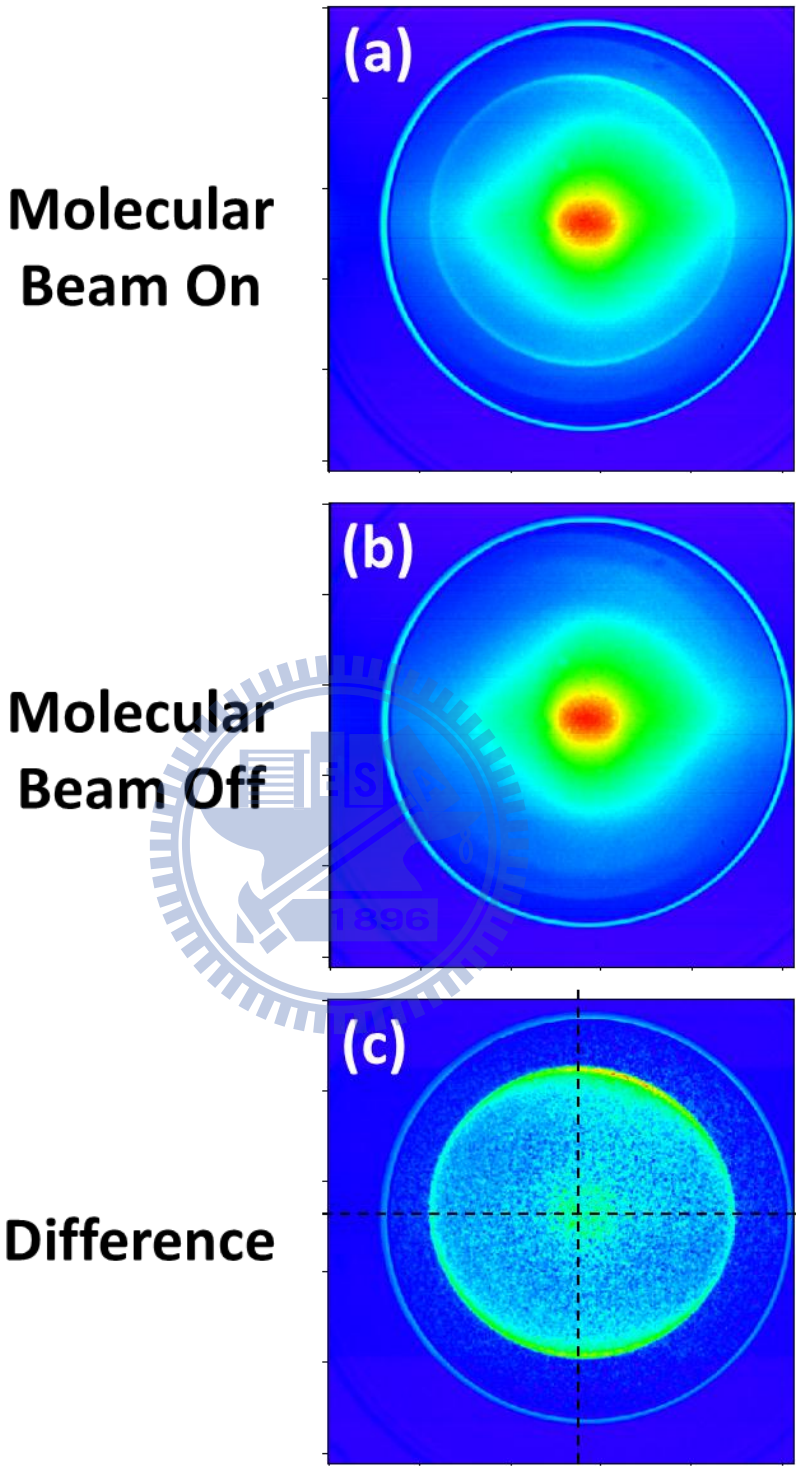

Figure 3.18 Photoelectron images of Ar using a new design electrode. (a) before background subtraction. (b) background image observed without the sample gas. (c) after background subtraction. The distortion of the image was observed.

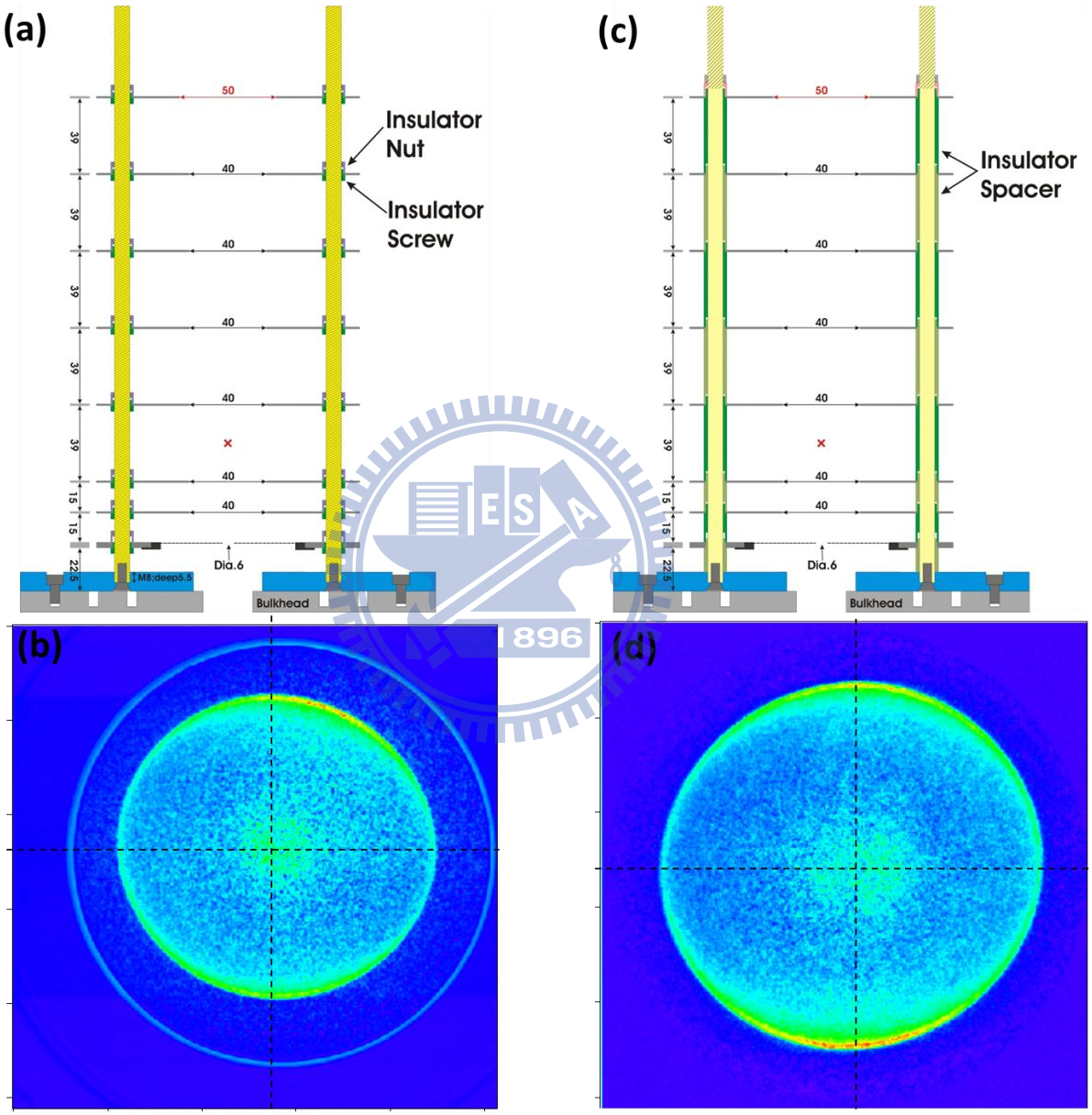

Figure 3.19 (b) and (d) are photoelectron images of Ar measuring with electrode (a) and (c), respectively.

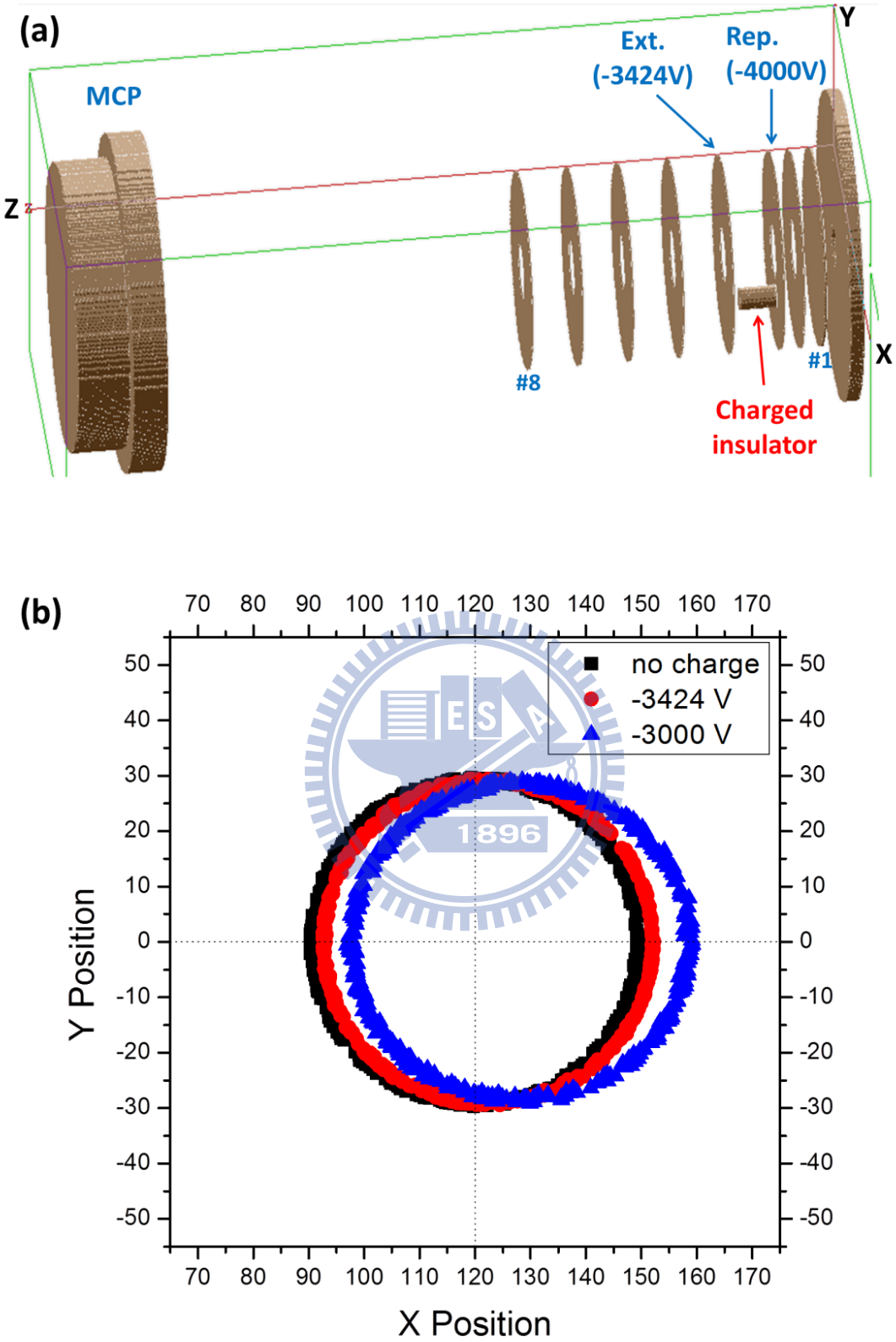

Figure 3.20 (a) The configuration of the spectrometer including a charged insulator in 3D drawing. (b) The images simulated in three conditions: (i) no charged insulator (black), (ii) charged insulator with -800V (red) and (iii) charged insulator with -50 V (blue).

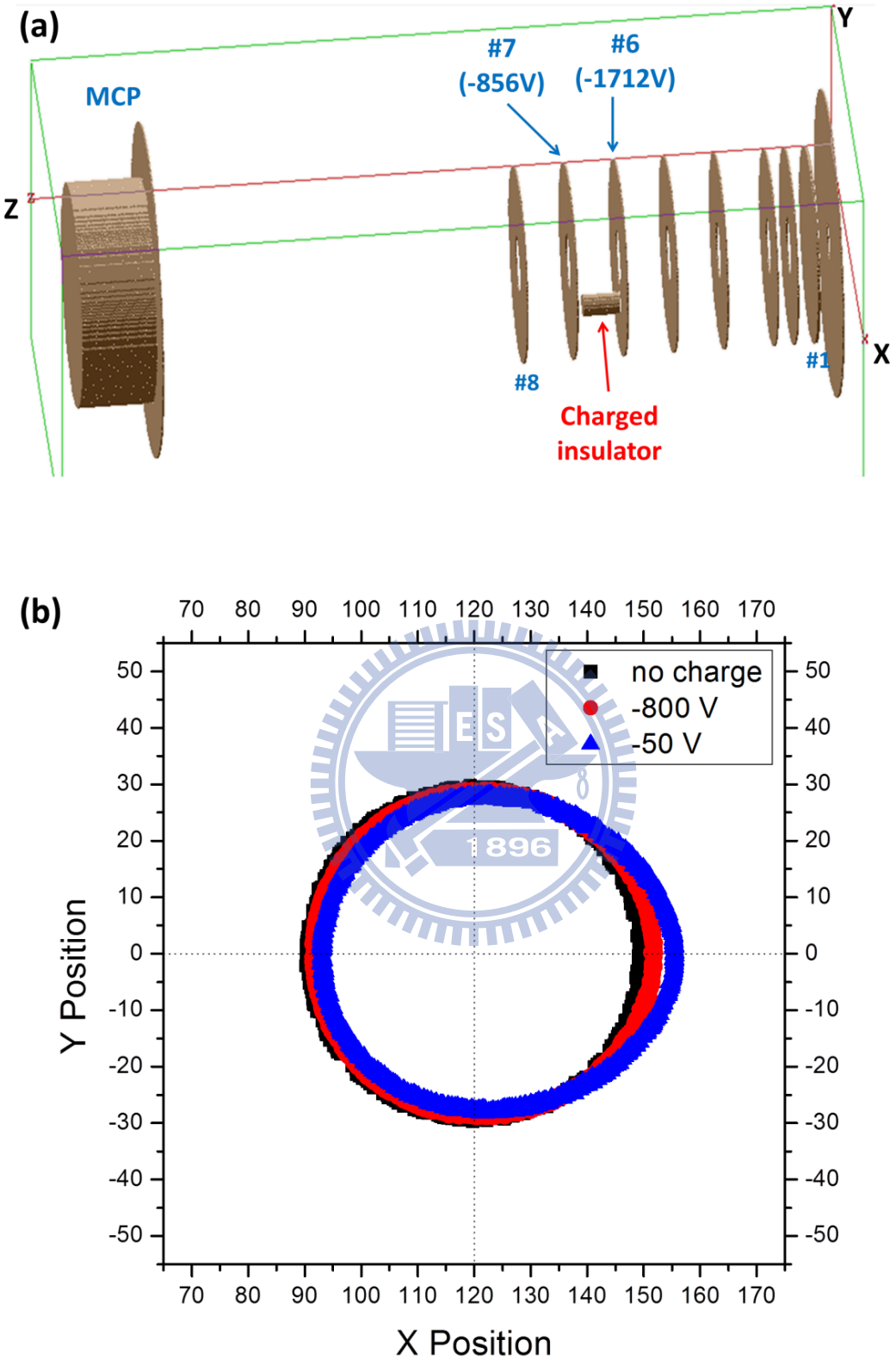

Figure 3.21 (a) The configuration of the spectrometer including a charged insulator in 3D drawing. (b) The images simulated in three conditions: (i) no charged insulator (black), (ii) charged insulator with -800V (red) and (iii) charged insulator with -50 V (blue).

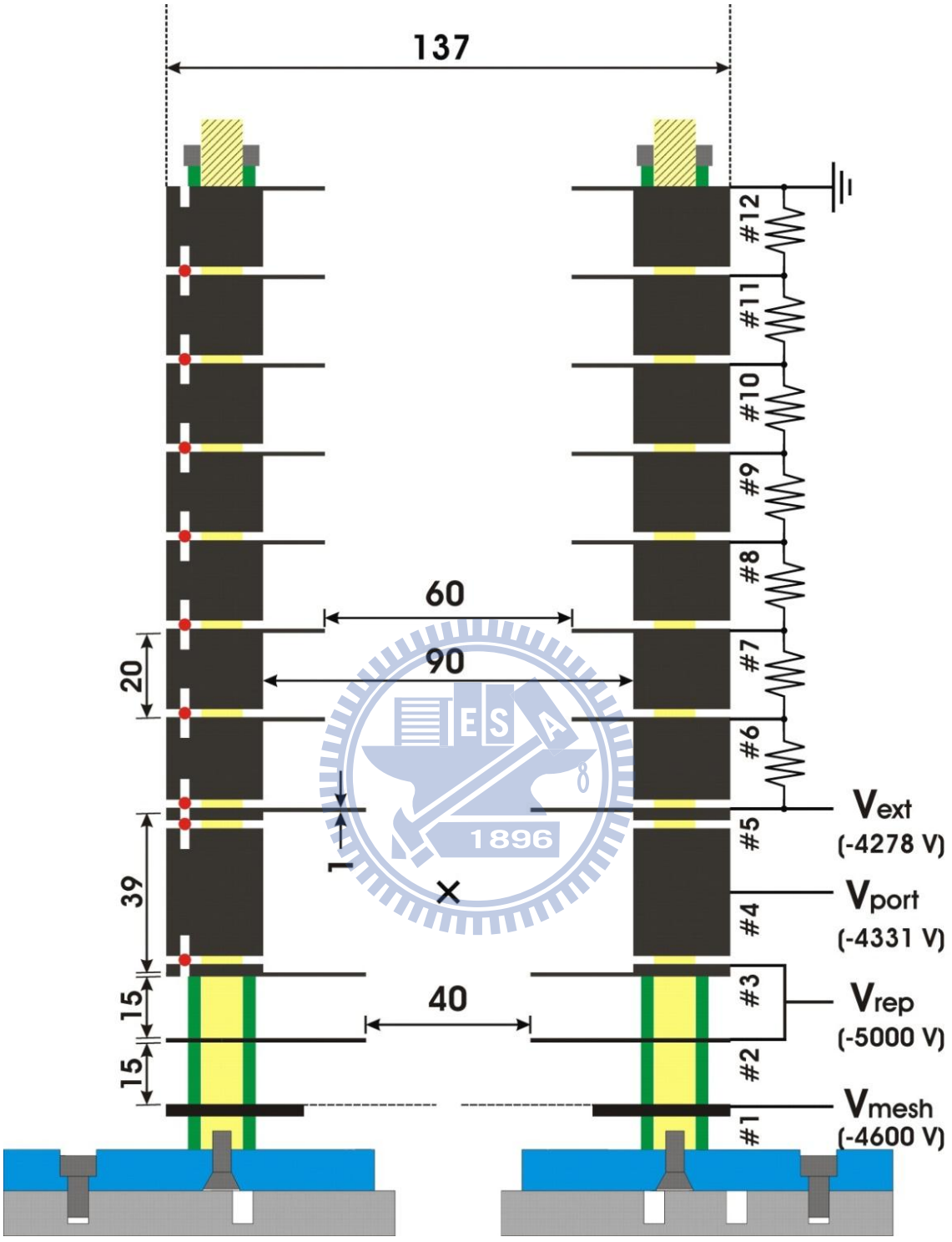

Figure 3.22 Cross-sectional view of the final design of the electrostatic lens system (all units in millimeters). A molecular beam is introduced from the bottom and is irradiated by He(I) radiation at the position indicated by the cross (×).An example of the voltage setting in the measurement of photoelectron image of Kr is also shown in the figure.

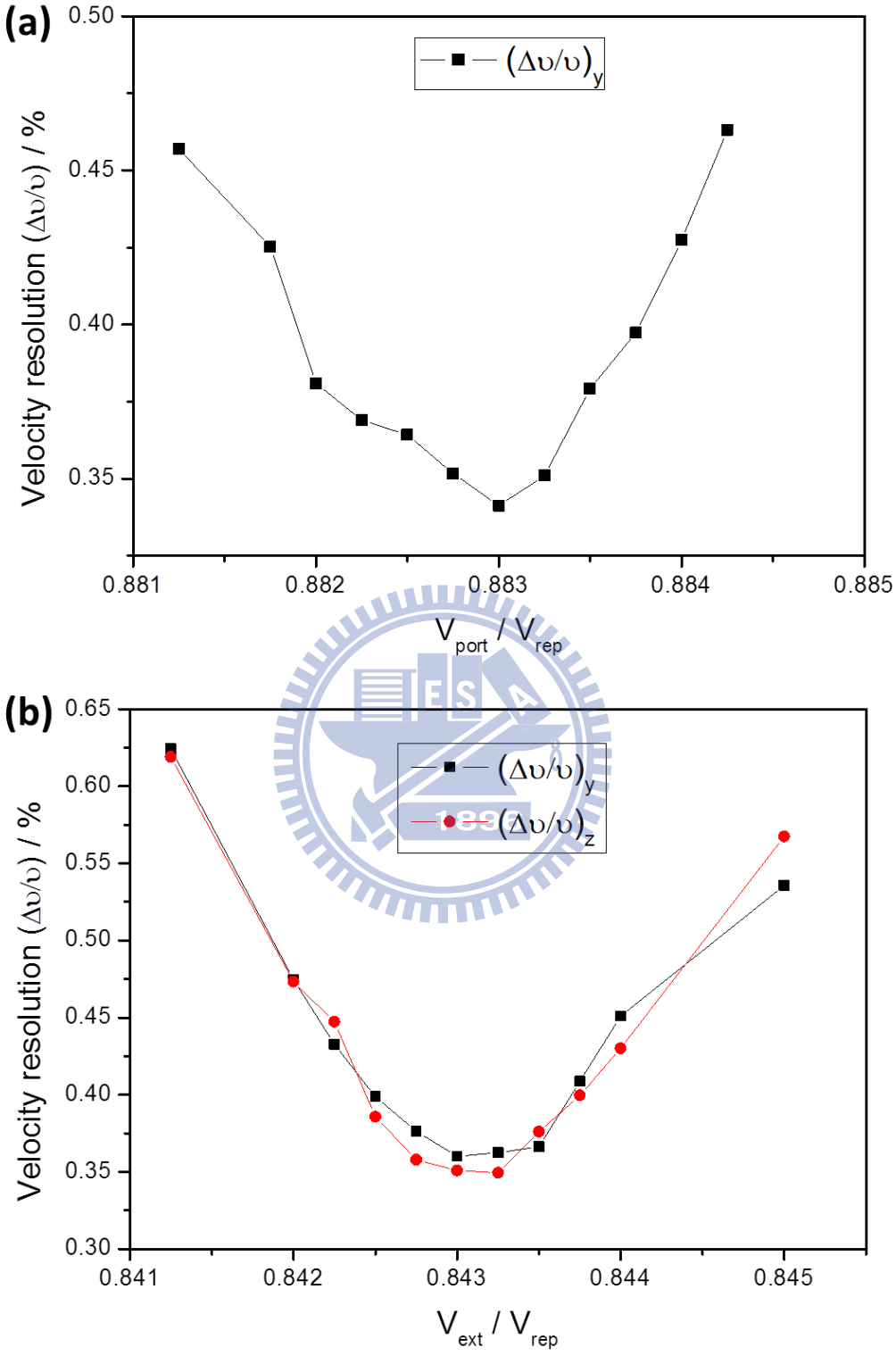

Figure 3.23 Velocity resolution simulated by performing trajectory calculation with 3D Simion software as a function of V_{port}/V_{rep} and V_{ext}/V_{rep}.

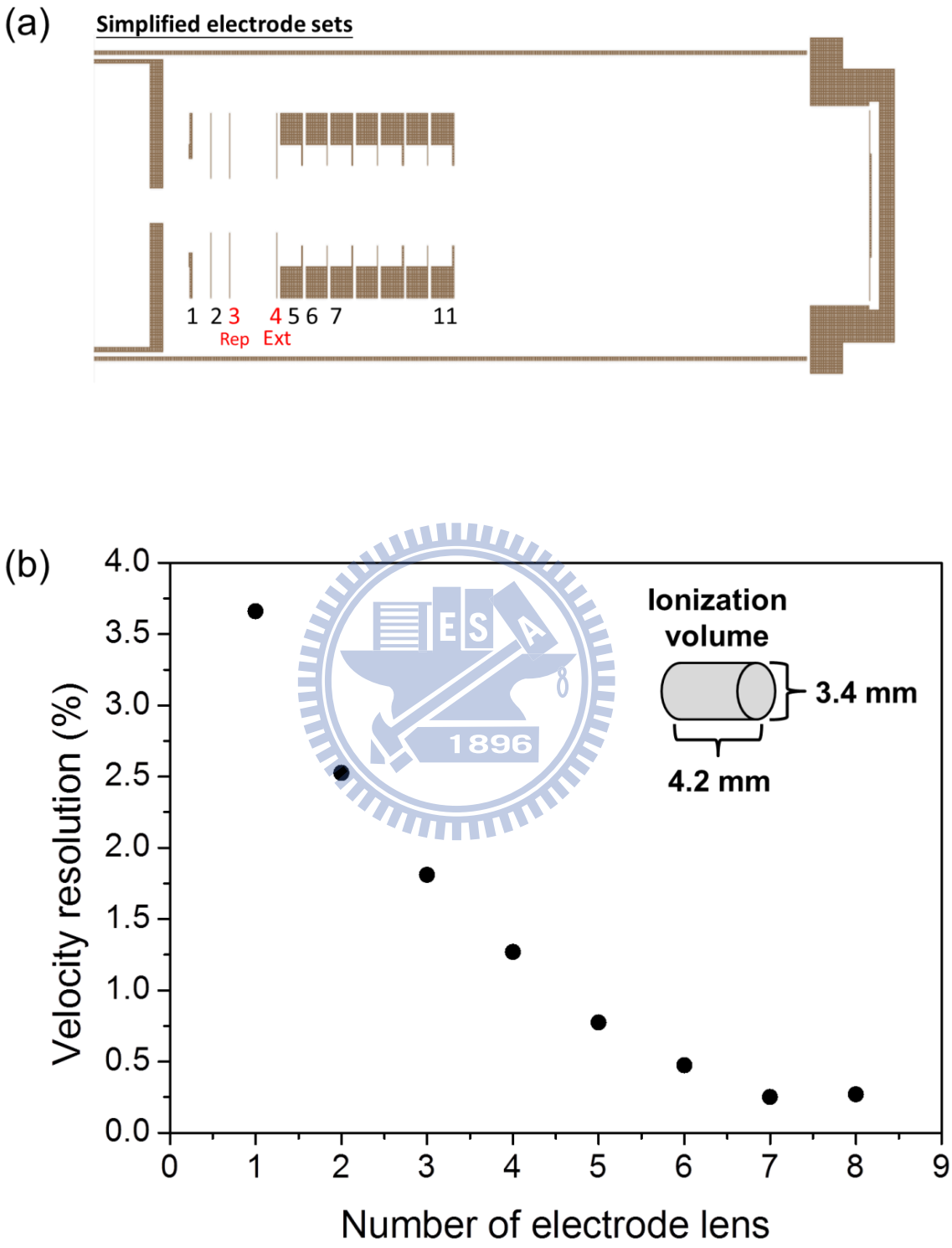

Figure 3.24 (a) The geometries of the simplified electrodes. (b) Calculated velocity resolution as a function of the number of lens electrodes behind the extractor. The ionization volume was assumed to be 3.4 ϕ × 4.2 mm.

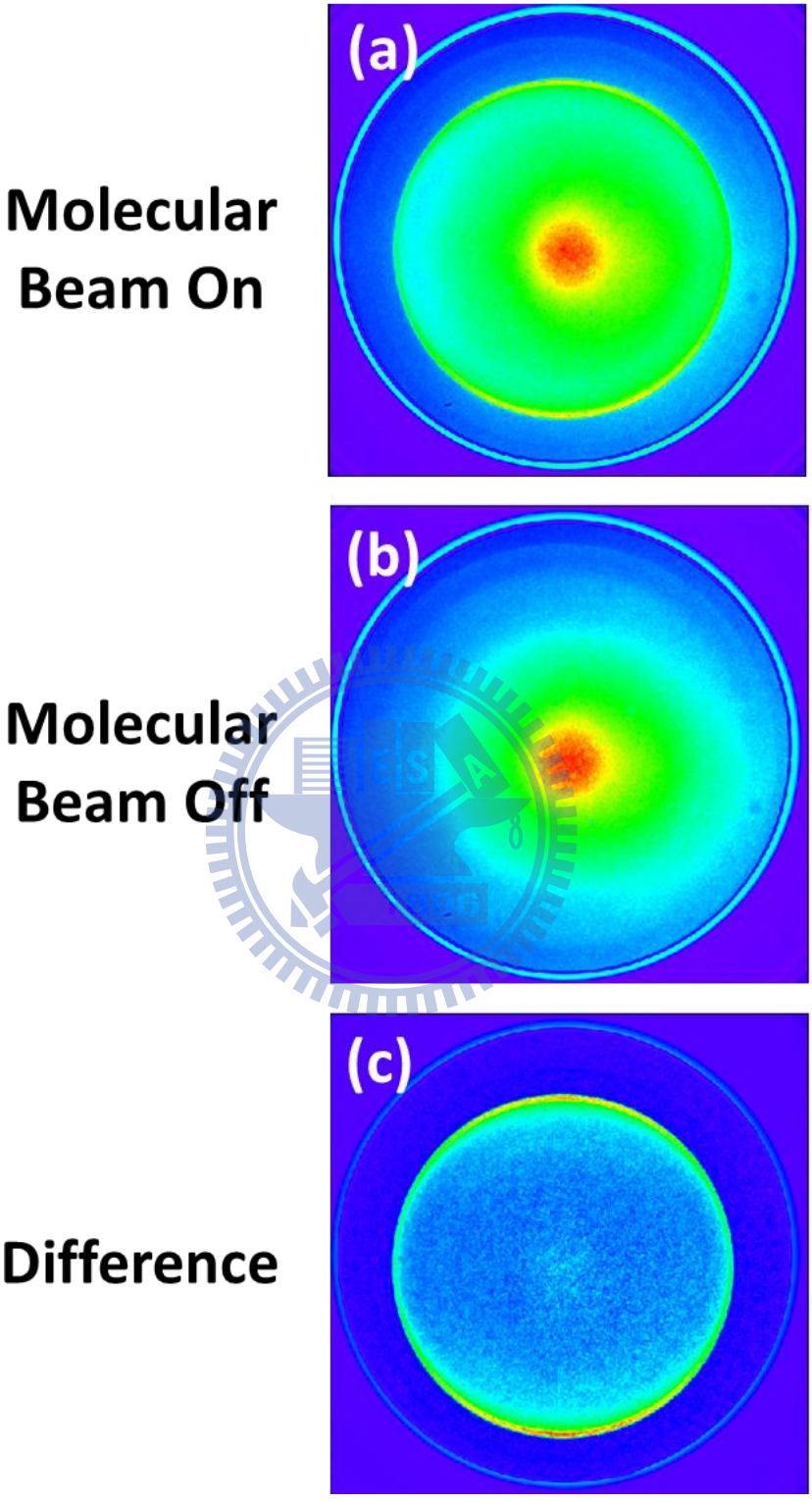

Figure 3.25 Photoelectron images of Ar using a new design electrode with shielding all insulators. (a) before background subtraction. (b) background image observed without the sample gas. (c) after background subtraction. No distortion of the image was observed.

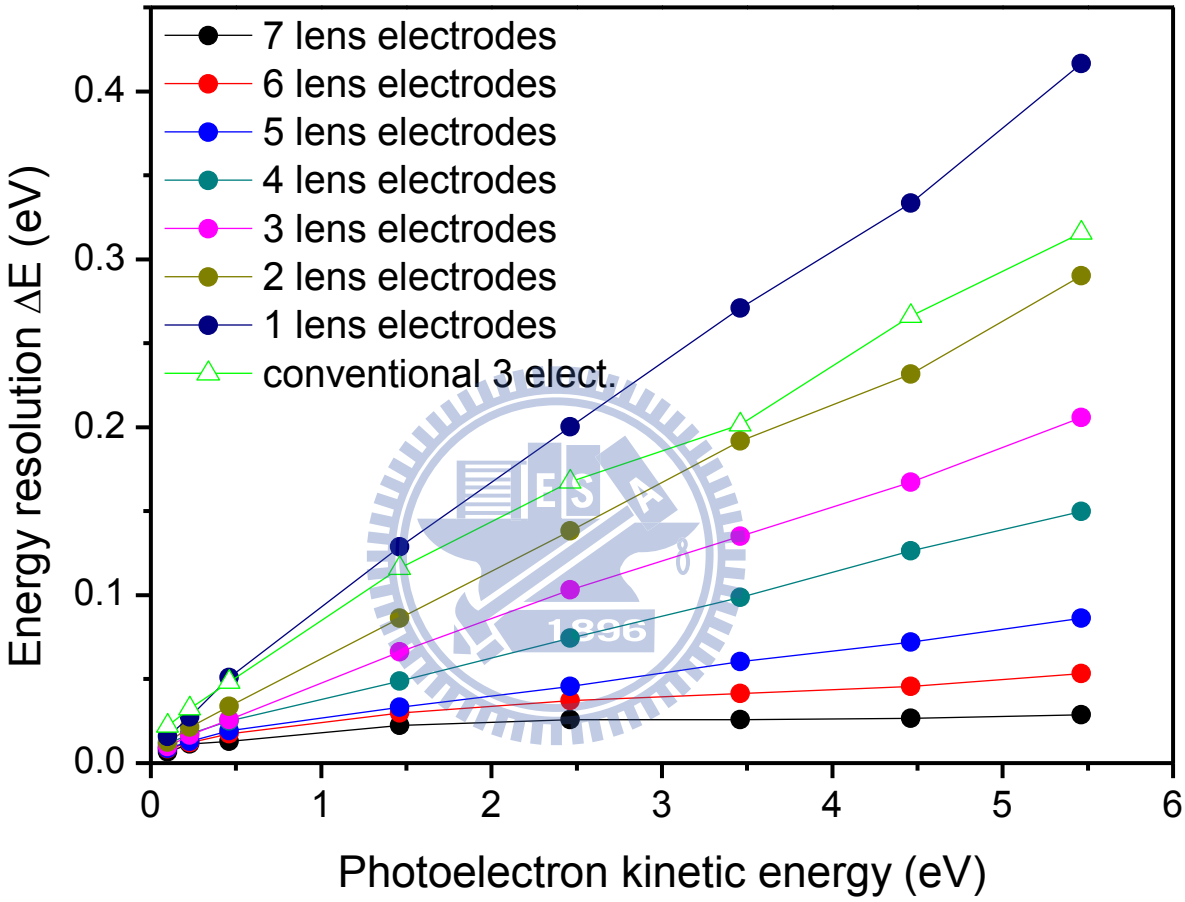

Figure 3.26 Simulated energy resolution (ΔE) as a function of photoelectron kinetic energy using our newly designed electrode with different number of lens electrodes. The result of conventional three-electrode design is also shown (open green triangle) in the figure.

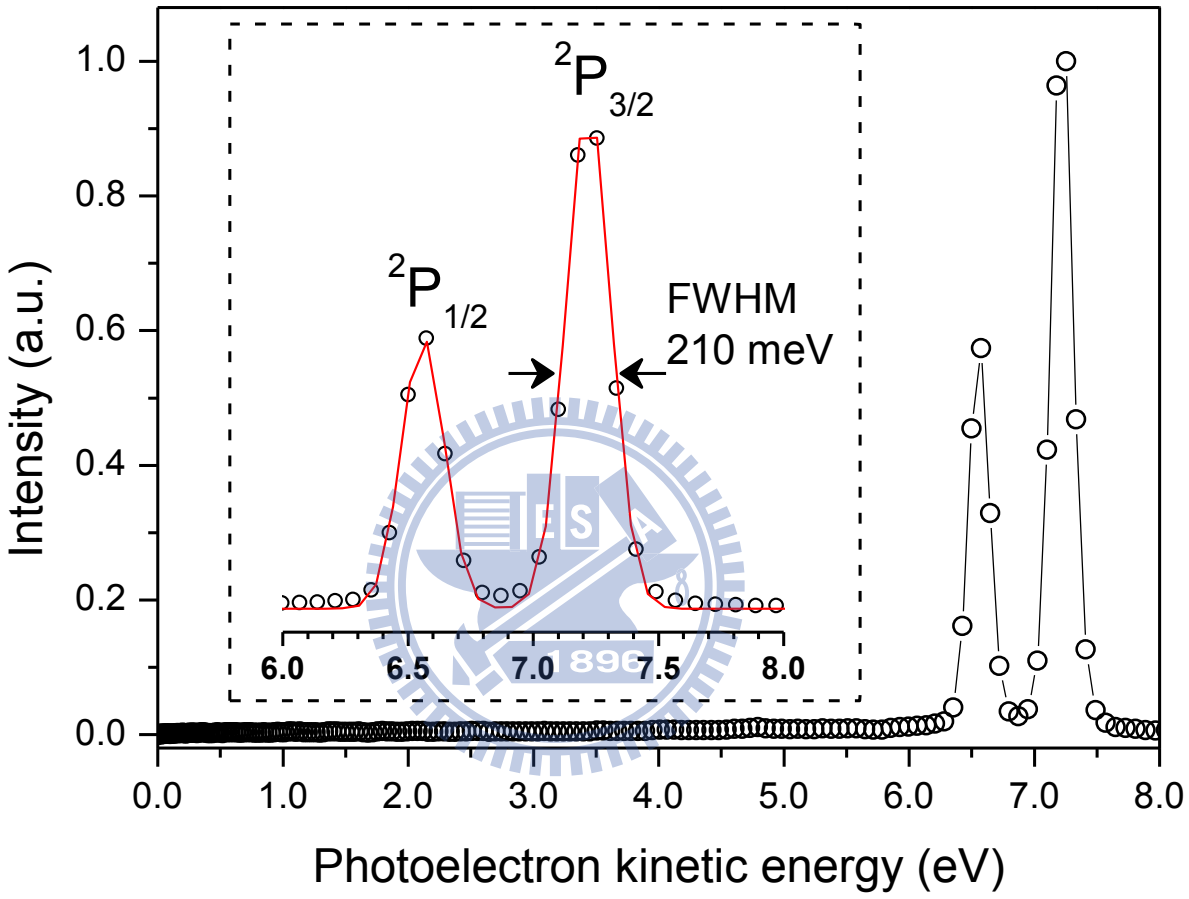

Figure 3.27 PKE distributions determined by He(I) PEI of supersonic beams of Kr using a (512 × 512 pixels) CCD camera. The inset shows an expanded view in the PKE region between 6.0 and 8.0 eV. The solid red line indicates the best-fit Gaussian to the observed data; it has a FWHM of 210 meV at 7.22 eV.

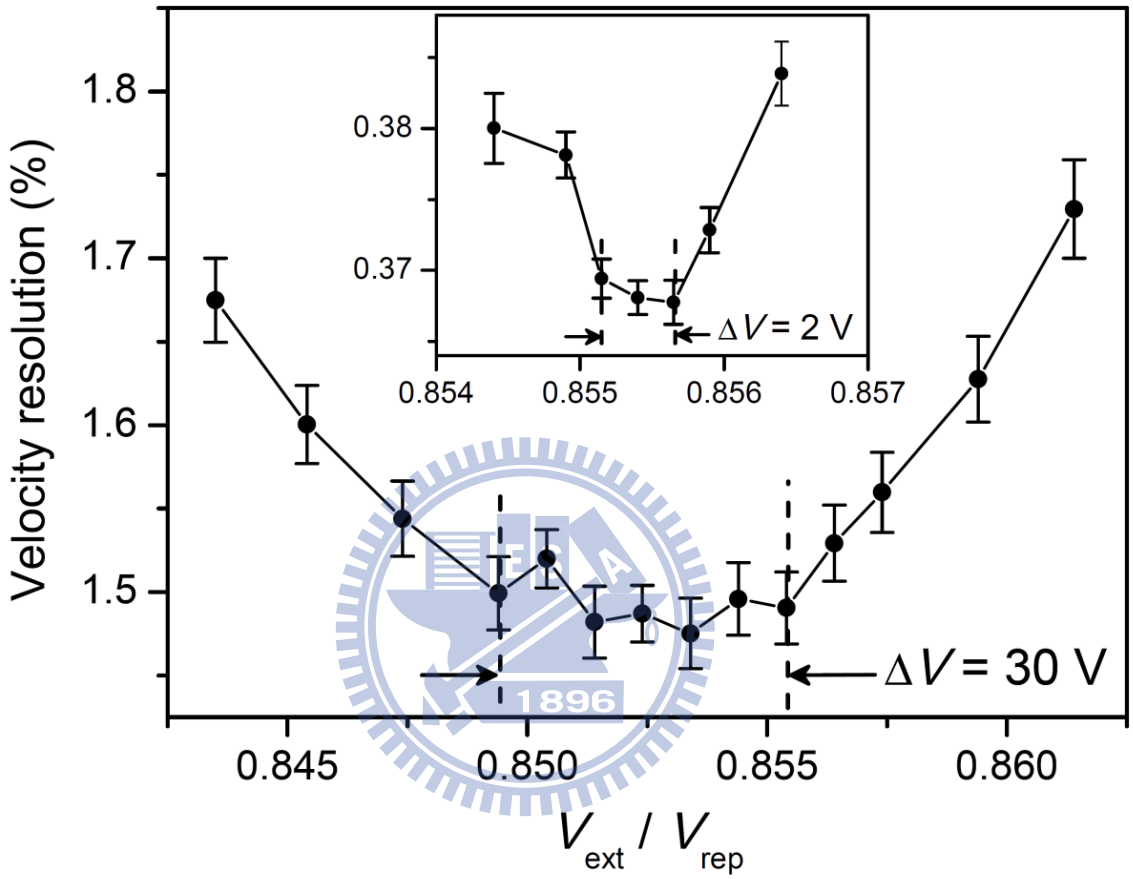

Figure 3.28 Velocity resolution evaluated using photoelectron imaging of Kr as a function of V_{ext}/V_{rep}. A low-resolution (512 × 512 pixels) CCD camera was used without image processing. Due to insufficient resolution of the camera, the focusing curve is dull. The inset shows velocity resolution evaluated using photoelectron imaging of Ar with super-resolution (4096 × 4096 pixels) imaging system. The focusing curve becomes much sharper and the resolution varies as a V-shape for the V_{ext}/V_{rep} ratio. The error bar corresponds to the fitting error (fwhm).

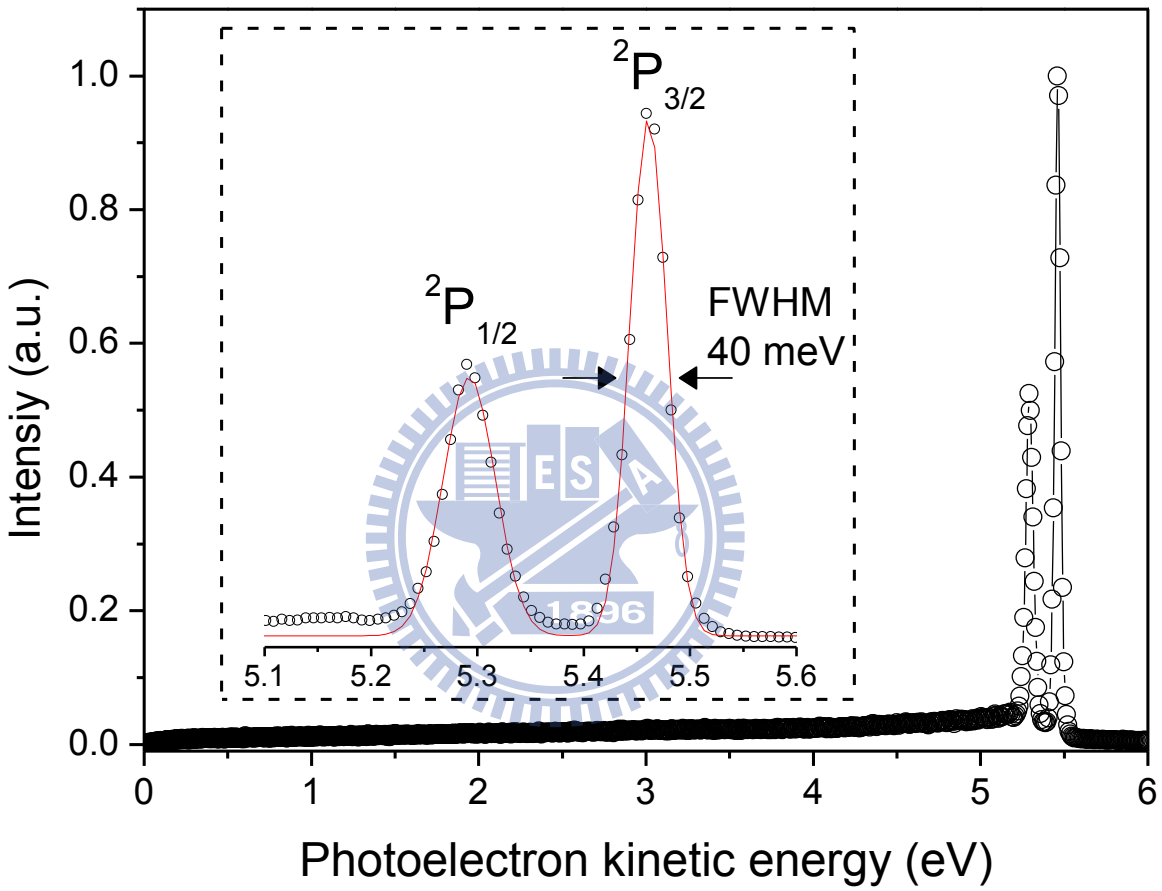

Figure 3.29 PKE distributions determined by He(I) PEI of supersonic beams of Ar using a super-resolution (4096 × 4096 pixels) imaging system. The inset shows an expanded view in the PKE region between 5.1 and 5.6 eV. The solid red line indicates the best-fit Gaussian to the obeerved data; it has a FWHM of 40 meV at 5.461 eV.

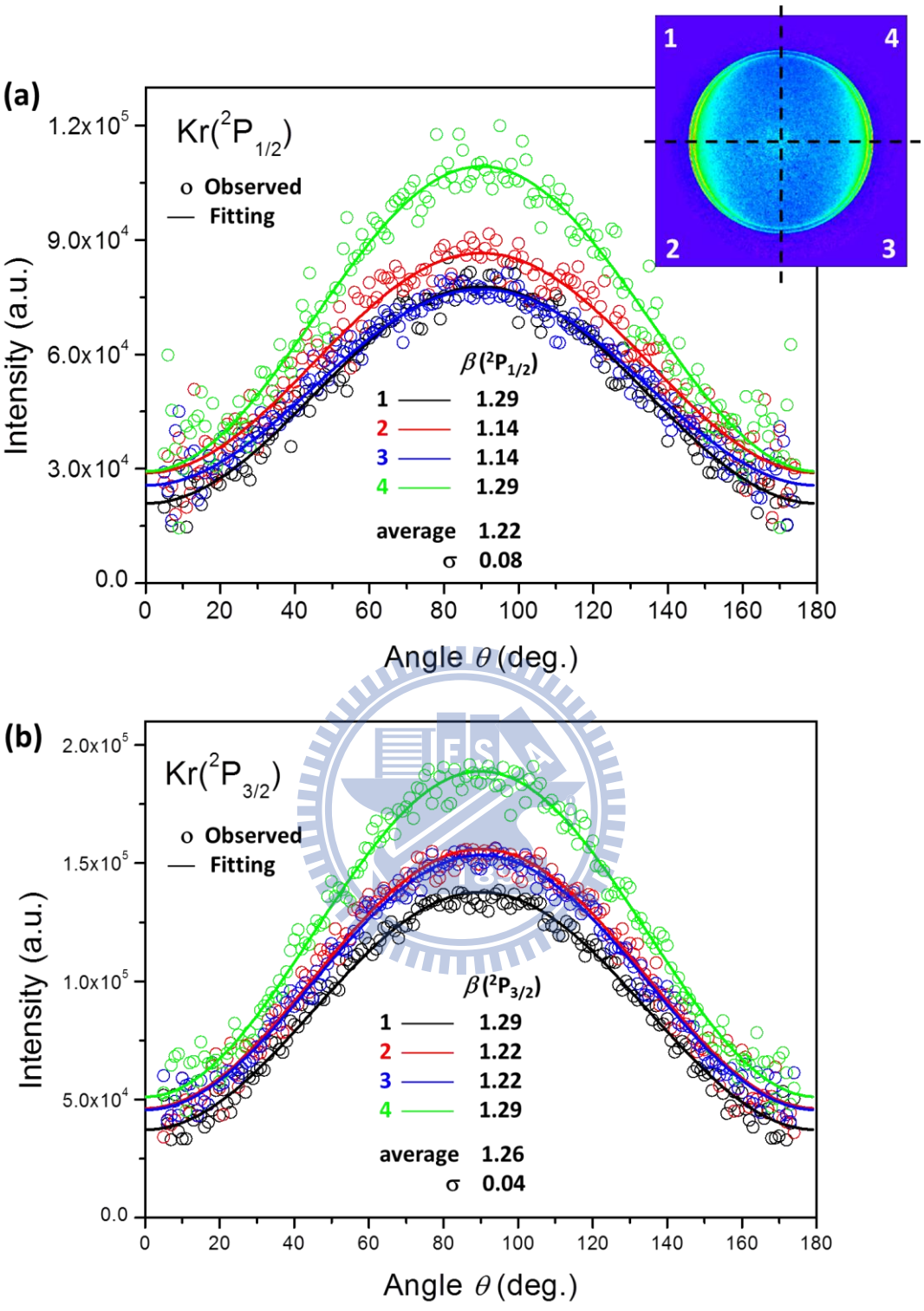

Figure 3.30 The definition of the individual four quadrants of the image is shown in the inset. The observed PAD of (a) $^2P_{1/2}$ and (b) $^2P_{3/2}$ of Kr, obtained from each quadrant and the corresponding least-squares fits are shown with open circles and solid lines. The determined anisotropy parameters, the average and the standard deviation σ obtained in each quadrant are also shown.

Table 3.1 Anisotropy parameter β for krypton as obtained in this work in comparison with the literature values.

		β	
Ionic state	**eBE(eV)**	**This work**	**Previous reports**
$^2P_{3/2}$	14.00	1.23	1.24(2), 1 1.30(4),[7] 1.30(5),[8] 1.29(5),[9] 1.37(2),[10] 1.20(5)[11]
$^2P_{1/2}$	14.65	1.09	1.21(2),1 1.23(4),7 1.23(5),8 1.25(5),9 1.37(3),10 1.20(5)11

Errors (±, in the last digit unless indicated otherwise) given in parentheses.

Table 3.2 Anisotropy parameter β for argon as obtained in this work in comparison with the literature values.

		β	
Ionic state	**eBE(eV)**	**This work**	**Previous reports**
$^2P_{3/2}$	15.76	0.92	0.93(2),7 0.97,[12] 0.88(2),[13] 0.95(2),[14] 0.89(4),9 0.95(2),10 0.85(5)11
$^2P_{1/2}$	15.94		0.92(2),7 0.97,12 0.86(2),[13] 0.95(2)[14] 0.89(4),9 0.95(2),10 0.85(5)11

Errors (±, in the last digit unless indicated otherwise) given in parentheses.

3.4 References

[1] Kreile, J.; Kurland, H. D.; Seibel, W.; Schweig, A. *Nucl. Instr. and Meth.* **1991**, *308* 621.

[2] Carnovale, F. *et al*. *J. Chem. Phys*. **1989**, *90*, 1452.

[3] Dehmer, P. M.; Dehmer, J. L. *J. Chem. Phys*. **1979**, *70*, 4574.

[4] Eppink, A. T. J. B.; Parker, D. H. *Rev. Sci. Instrum.* **1997**, *68*, 3477.

[5] Szilagyi, M. N. *Proc. IEEE* **1985**, *73*, 412.

[6] Ogi, Y.; Kohguchi, H.; Niu, D.; Ohshimo, K.; Suzuki, T. *J. Phys. Chem. A* **2009**, *113*, 14536

[7] Kreile, J.; Schweig, A. *J. Electron Spectrosc. Relat. Phenom.* **1980**, *20*, 191.

[8] Karlsson, L.; Mattson, L.; Jadrny, R.; Siegbahn, K.; Thimm, K. *Phys. Lett. A* **1976**, *58*, 6.

[9] Dehmer, J. L.; Chupka, W. A.; Berkowitz, J.; Jivery, W. T. *Phys. Rev. A* **1975**, *12*, 1966.

[10] Niehaus, A.; Ruf, M. W. *Z. Phys.* **1972**, *252*, 84.

[11] Carlson, T. A.; Jonas, A. E. *J Chem. Phys.* **1971**, *55*, 4913.

[12] Kibel, M. H.; Leng, F. J.; Nyberg, G. L. *J Electron Spectrosc. Relat. Phenom*. **1979**, *15*, 281.

[13] Mason, D. C.; Mintz, D. M.; Kuppermann, A. *Rev. Sci. Instrum.* **1977**, *48*, 926.

[14] Hancock, W. H.; Samson, J. A. R. *J Electron Spectrosc. Relat. Phenom.* **1976**, *9*, 211.

Chapter 4

He(I) Photoelectron Imaging of Benzene and Pyridine

The preceding chapters have focused on the designing of a photoelectron imaging spectrometer. In this chapter, He(I) ultraviolet photoelectron imaging of benzene and pyridine in supersonic molecular beams are discussed.

4.1 He(I) Ultraviolet Photoelectron Imaging of Benzene

4.1.1 Introduction

Benzene (C_6H_6) is one of the most fundamental polyatomic molecules, and its photoelectron spectroscopy has been performed using UV[1-14] and X-ray light sources.[15-19] The configuration of valence electrons in benzene is

$[2e_{2g}(\sigma)]\ [3a_{1g}(\sigma)]\ [2b_{1u}(\sigma)]\ [1b_{2u}(\sigma)]\ [3e_{1u}(\sigma)]\ [1a_{2u}(\pi)]\ [3e_{2g}(\sigma)]\ [1e_{1g}(\pi)]$

in the ascending order of the orbital energy. Theoretical studies predict that eight ionic states can be observed by photoionization of benzene with He(I) radiation (21.22eV). There were some controversies in the assignment of observed He(I) photoelectron spectrum of benzene[1,20]. One controversy was the assignments of the D_1 and D_2 states between 11 and 13 eV. Lindholm *et al*.[6] suggested the electron removals from the $3e_{2g}(\sigma)$ and $1a_{2u}(\pi)$ orbitals as $D_2[A^2E_{2g}]$ and $D_1[B^2A_{2u}]$ states of $C_6H_6^+$, respectively. Although this assignment has been supported by a number of researchers,[4,7,16,21,22] Turner *et al*.[1] and Price *et al*.[5,23] preferred the reversed assignment. Carlson *et al*.[4] measured the angle-resolved He(I) photoelectron spectrum and found that the anisotropy parameter gradually increases between 11 and 13 eV. They suggested $D_1[A^2E_{2g}]$ and $D_2[B^2A_{2u}]$. This assignment has been further supported by

Mattsson *et al.*[24] and Sell *et al.*[25] Carlson *et al.*[26] and Baltzer *et al.*[27] measured the energy dependence of the anisotropy parameters using synchrotron radiation and compared with calculations based on the multiple scattering Xα method. These studies established $D_1[A^2E_{2g}]$ and $D_2[B^2A_{2u}]$. Another controversy concerned the assignments of the band at 15.5 eV. Jonsson *et al.*[28] assigned this band as the electron removals from the $2b_{1u}(\sigma)$ orbital, whereas Price *et al.*5 assigned it to $3a_{1g}(\sigma)$. This problem was settled by Gelius *et al.*[16,23] who supported Jonsson based on the intensity analysis of the X-ray photoelectron spectrum.

4.1.2 Interference from the residual water vapor in the chamber

We performed PEI experiments using continuous supersonic beams of polyatomic molecules. However, the signal level was not much higher than the background photoionization signal of the residual water vapor in the chamber. The partial pressure of water in the ionization camber was measured to be ~ 2×10^{-8} Torr using a residual gas analyzer (Stanford Research Systems, RGA200). Figure 4.1 (a) shows a photoelectron image obtained with a continuous beam of benzene 8 % in He expanded with a stagnation pressure of 1.2 atm; the signal and background images were integrated for 100 min, and the background image obtained without the molecular beam has already been subtracted. This image exhibits a vertical band along the VUV light path, which is due to photoionization of water vapor. The photoelectrons signal of water remains in Fig. 4.1 (a) even after the background subtraction, indicating water vapor pressure changed with and without the molecular beam. Figures 4.1 (b) and (c) show ion images observed with and without the molecular beam, respectively; ions were not mass-selected. These images spatial distribution of ions along the light path of He(I) radiation. Bright elliptical spot in the center is due to benzene ions produced in the molecular beam, whereas the vertical band arises from water ions.

4.1.3 Results

To enhance the signal/background contrast ratio, we replaced a continuous beam with a pulsed beam and we added a turbo molecular pump (650 L/s) to the ionization chamber. This allowed us to increase the ratio of the partial pressure of benzene against water vapor during the gas pulse. We time-gated both CCD and MCP so as to detect photoelectrons only when a pulsed beam was introduced into the ionization region. In order to synchronize the readout of the CCD camera with a gas pulse, we used a low-resolution CCD camera (512 × 512 pixels) that accepts an external trigger. Figure 4.2 (a) shows a photoelectron image measured with a pulsed supersonic beam of benzene 18 % seeded in He expanded at a stagnation pressure of 0.55 atm; the signal and background images were integrated for 90 min at a data acquisition rate of 20 Hz, and the latter was subtracted from the former to obtain Fig. 4.2(a). It is seen that the background photoelectron signal is considerably smaller than the case using a continuous molecular beam. As the vacuum system can allow 100 Hz of gas pulses at a stagnation pressure of 0.55 atm, the duty cycle of our PEI system can be easily increased by a factor of five by not synchronizing the CCD camera.

Figure 4.2 (b) shows the slice image obtained by taking the inverse Abel transform of Fig. 4.2 (a). As mentioned in chapter 1, photoionization with unpolarized light generates a PAD that is cylindrically symmetric about the light propagation direction (indicated by the arrow in the figure). Figure 4.2 (c) shows the energy-dependent anisotropy parameter determined from the image. Although the concentration of benzene (18 %) in the pulsed beam was high, no signature from benzene dimers has been identified at ionization energy (IE) of 8.65 eV[29] in our photoelectron spectrum. No vibrational structure was resolved with our energy resolution of 0.2–0.3 eV. The vibrationally-resolved He(I) photoelectron spectrum of the first band has been reported by Baltzer *et al.*[20]; however, β has not been determined at a vibrational resolution. The energy-dependent anisotropy parameter determined in the present study is in excellent agreement with the literature as presented in Fig. 4.2(c) and Table 4.1.[11,12,19] In the

lowest photoelectron band, β decreases with the electron binding energy. Carlson and Anderson[4] have observed the same feature and suggested that it may be due to the Jahn–Teller effect in D_0. However, the influence of Jahn–Teller splitting on β has not been elucidated experimentally or theoretically for any molecular system.[30] Another possible origin for the variation of β is a Coulomb phase. Since β for photoionization from the $1e_{1g}(\pi)$ orbital increases with increasing PKE,[19,20,31] β is expected to diminish at higher binding energies (i.e., lower PKEs) within the first band.

4.2 He(I) Ultraviolet Photoelectron Imaging of Pyridine

4.2.1 Introduction

Pyridine (C_5H_5N) is an important model system in relation to biologically active nicotinic acid and the nucleotides of cytosine, uracil, and thymine. It is also an example of heterocyclic aromatic molecules. The replacement of a carbon atom with a nitrogen atom in a benzene ring creates a lone-pair orbital. The lowest photoelectron band of pyridine has overlapping bands from ionization of a nonbonding (n) and a π electron. El-Sayed *et al.*[32] studied Rydberg series of pyridine by absorption spectroscopy and postulated that the π^{-1} state exist at 9.266 and 11.56 eV and the n^{-1} state is at about 10.3 eV. Jonsson *et al.*[33] suggested the D_0, D_1, and D_2 to be π^{-1}, π^{-1}, and n^{-1} based on the electron-scattering spectrum and theoretical calculations. Berg *et al.*[34] measured multiphoton spectrum of pyridine and suggested that n^{-1} is the lowest cation state.

These early photoelectron experiments suggested all three possible assignments of π-π-n,[1,35] π-n-π,[36] and n-π-π[37-40]. The resolution of this confusion required additional information. Utsunomiya *et al.*[41] performed the first angle-resolved PES of pyridine in 1978 and found that near the ionization threshold β increases from 0.2 to ~ 0.6 in the middle of the first band. They referred that ionization to the n^{-1} state of 2,6-lutidine (dimethyl-pyridine)

exhibits low β and assigned D_0 of pyridine to the n^{-1} state and D_1 to the π^{-1} state. Piancastelli *et al.*[42] found that β in the higher binding energy region of the first band increases more rapidly with the photon energy than the lower binding energy region, from which they also assigned D_0 to the n^{-1} state and D_1 to the π^{-1} state. In theoretical studies, Green function calculations[43-45] and valence bond method[46] predict a π-n-π ordering, while more recent calculations of SAC-CI,[44] DFT-TP,[45] CASPT2,[46] and MRDCI[47] suggest an n-π-π ordering in agreement with experimental studies. MRDCI predict that the first two ionic states have an energy difference of 0.7 eV, whereas the other methods predict differences less than 0.2 eV.

So far, angle-resolved PES of pyridine has been limited to the first three ionic states. In this study, the energy-dependent anisotropy parameter is determined for the entire energy region accessible with He(I) radiation.

4.2.2 Results

Figure 4.3 (a) shows a photoelectron image measured with a pulsed supersonic beam of 10 % pyridine seeded in He. The background image has been subtracted. The left half is the raw image and the right half is the slice image obtained by inverse Abel transform. Figure 4.3 (b) shows the photoelectron energy spectrum and β extracted from the slice image. The numerical values of β are also compared with the literature[41,42] in Table 4.2. A microdischarge of MCP occurred when a high density molecular beam impinged on the detector, we needed to restrict the stagnation pressure for supersonic expansion to be 0.2 atm. (The observed microdischarge was a specific problem of this detector.) Because of the low stagnation pressure of 0.2 atm, a long (3 hours) integration time was needed to measure the image. In the future, microdischarge should be avoided by redesigning the PEI spectrometer so that a molecular beam travells parallel to the face of the imaging detector.

As seen in Fig. 4.3 (b), β of the first band between 9.2 and 10.2 eV increases with the binding energy in agreement with Utsunomiya *et al.*[41] and Piancastelli *et al.*,[42]. This band has

contribution of D_0 and D_1 associated with electron removal from $11a_1(n)$ and $1a_2(\pi)$ orbitals, respectively. In He(I) UPS of pyridine, the first band corresponds to PKE between 12.02 and 11.02 eV. In this PKE region, β increases only gradually with PKE if it is due to the energy-dependent Coulomb phases.[31] The observed β increases rather rapidly with the electron binding energy (i.e. decreasing PKE), which indicates that the variation of β in the first band is not due to Coulomb phases and rather due to D_1 overlap with D_0. The origin of D_1 has not been determined yet.

The fourth and fifth bands between 12.5 and 13.5 eV have been assigned to ionization from $b_2\sigma$ and $b_1\pi$, respectively.[41] As far as we know, β has not been determined at the electron binding energies over 14 eV. The variation of β in this region is similar to that of benzene; β has a deep minimum at about 15.8 eV for pyridine and 14.9 eV for benzene. All these cation states are due to the removal of an electron from the σ orbitals (see Fig. 4.3). There are two different theoretical assignments for the overlapping bands within 0.3 eV around 15.8 eV. These bands are associated with the $9a_1(\sigma)$ C–H and $5b_2(\sigma)$ C–C bonding orbitals. All calculations that suggest $D_0(n^{-1})$–$D_1(\pi^{-1})$–$D_2(\pi^{-1})$ assignment of the first three states suggest $[5b_2(\sigma)]^{-1} < [9a_1(\sigma)]^{-1}$ whereas the others that predict π–n–π ordering for the first three states suggest the opposite $[5b_2(\sigma)]^{-1} > [9a_1(\sigma)]^{-1}$. The assignments in Fig. 4.3 follow the former assignment.

4.3 Conclusion

A high signal/background contrast ratio was achieved in PEI using a seeded molecular beam by introduction of a pulsed beam. The major source of the background photoelectrons are from residual water vapor in the photoioniztion chamber. The photoelectron anisotropy parameters determined for benzene and pyridine were in good agreement with the literatures.

The anisotropy parameters were determined for the first time for pyridine at the electron binding energies over 14 eV. Higher energy resolution is obtainable in principle by centroiding calculations of the light spots on the phosphor screen of the detector. However, our super-resolution imaging system is currently able to handle up to 256 light spots in a single frame (30 frames/s), which is too low for He(I) PEI. This problem will be solved in the future when a higher frame rate of a camera and a faster digital image processing circuit become available.

Figure 4.1 (a) Photoelectron image of a continuous supersonic beam of 8% benzene seeded in He (the background image has been subtracted). (b) Ion image with the supersonic molecular beam. (c) Ion image without the molecular beam. The arrow indicates the propagation direction of the He(I) radiation.

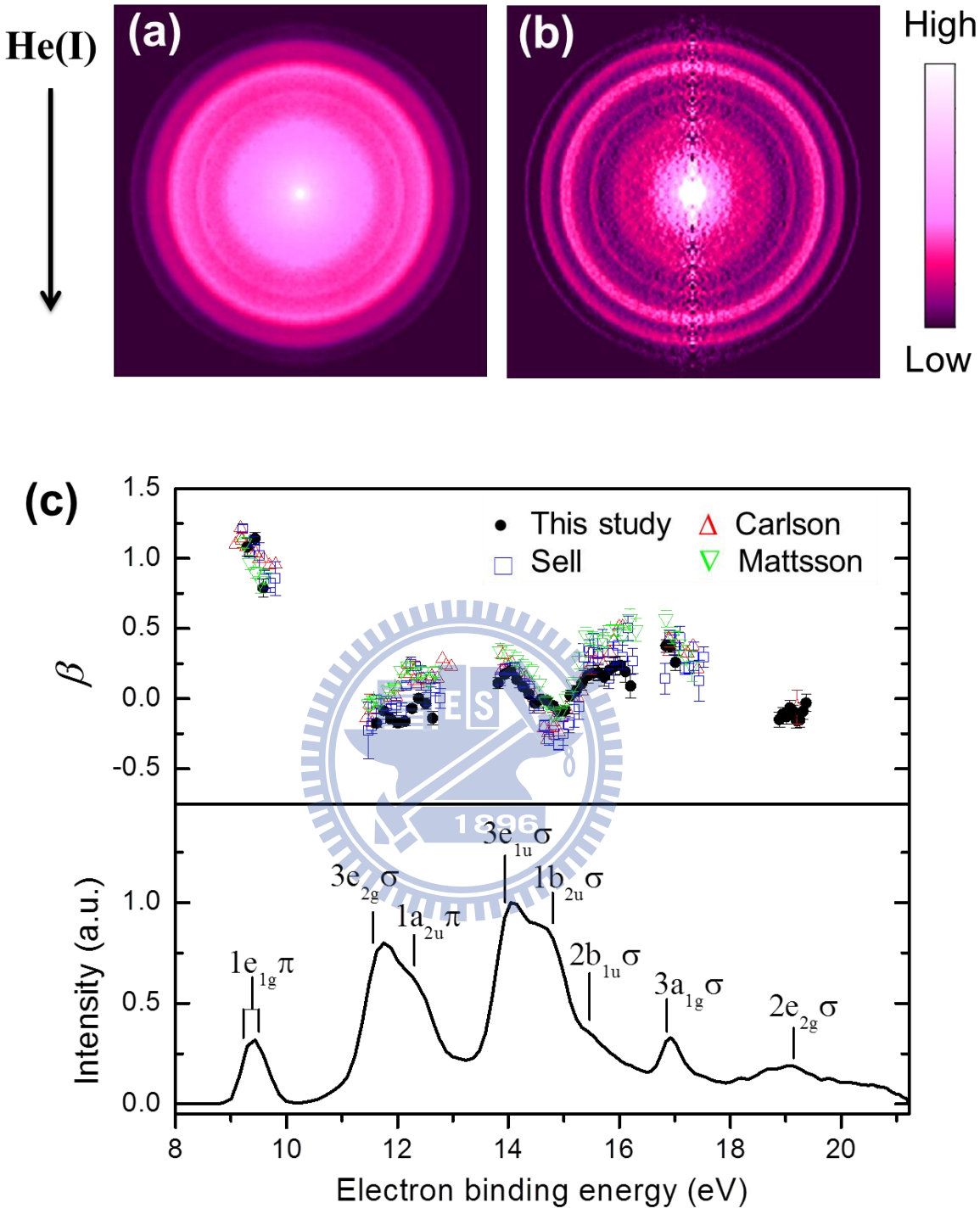

Figure 4.2 (a) Symmetrized photoelectron image of a pulsed supersonic beam of benzene. (b) the slice image obtained from (a). (c) The energy-dependent anisotropy parameters β (upper panel, solid circle) and photoelectron spectra (lower panel) obtained from (b). Data from [ref. 12], [ref. 19] and [ref. 11] are given as open squares (□), open triangles (Δ) and open inverted triangles (∇), respectively. The assignments of the ionized orbitals are indicated at the vertical ionization point [ref. 19]. The error bars are the fitting errors.

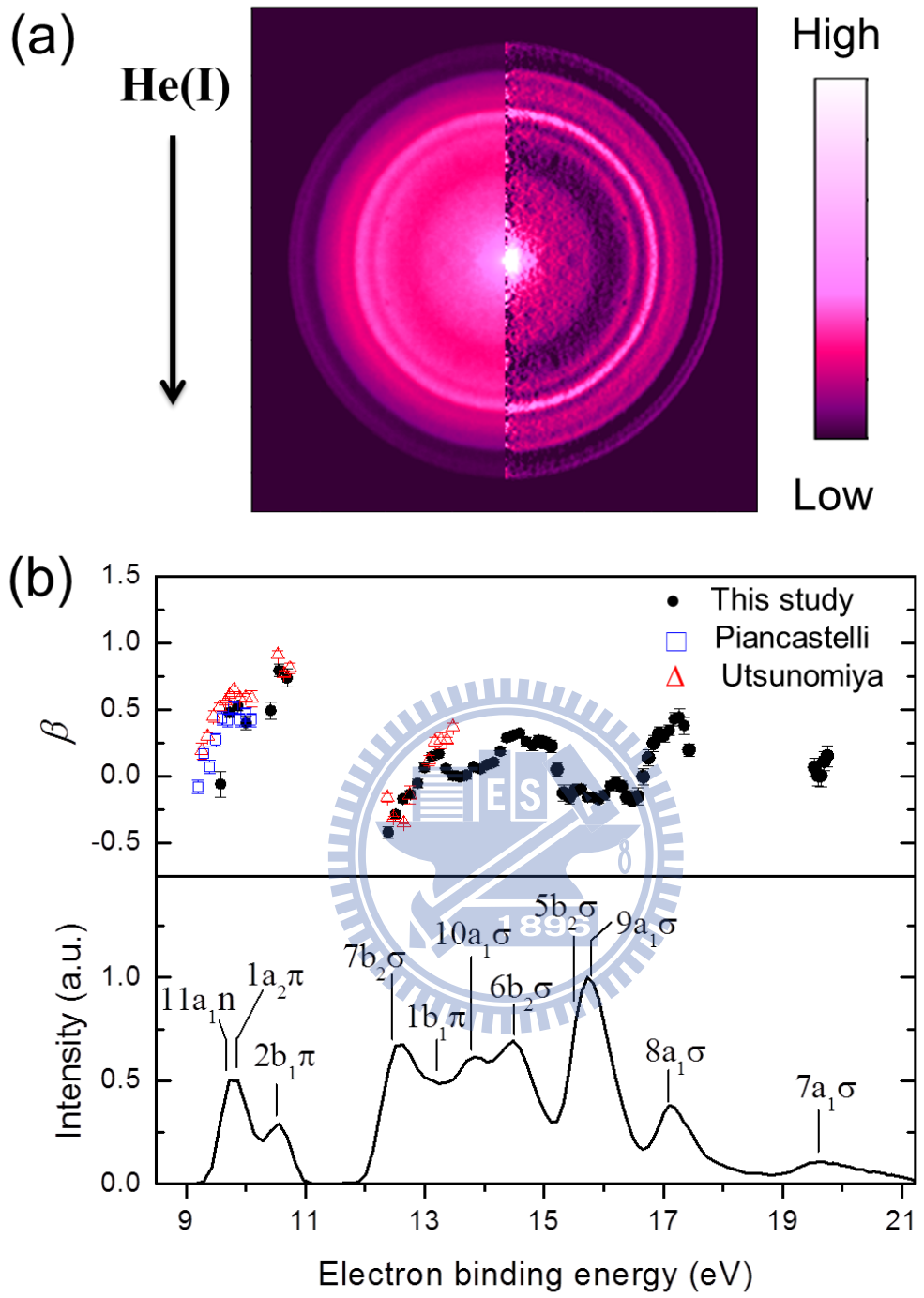

Figure 4.3 (a) Symmetrized photoelectron image of a pulsed supersonic beam of 10% pyridine seeded in He (left half) and the slice image taking the inverse Abel transform (right half). (b) The energy-dependent anisotropy parameter β (upper panel, solid circles) and photoelectron spectra (lower panel) obtained from (a). Data from [ref. 42] and [ref.41] are given as open squares (□) and open triangles (Δ), respectively. The assignments of the ionized orbitals are indicated at the vertical ionization point [ref. 44]. The error bars are the fitting errors.

Table 4.1 Electron binding energy (in eV) and anisotropy parameters (β) for benzene

	This study		Sell *et al.*[c]		Carlson *et al.*[d]		Mattsson *et al.*[f]	
Orbital[a]	eBE	β	eBE	β	eBE	β	eBE	β
$1e_{1g}(\pi)$					9.11	1.11		
			9.21	1.21(3)	9.19	1.15	9.24	1.11(4)
	9.29	1.08(6)[b]	9.33	1.04(4)	9.30	1.10	9.34	0.97(5)
					9.38	1.06		
	9.44	1.14(5)	9.42	1.13(3)	9.48	1.05	9.44	0.90(4)
			9.51	1.02(9)	9.53	1.01	9.53	0.84(9)
	9.58	0.79(7)	9.60	0.85(7)	9.63	1.00	9.61	0.87(5)
			9.71	0.83(7)	9.72	0.96		
			9.80	0.86(12)	9.84	0.97		
$3e_{2g}(\sigma)$			11.48	–0.23(2)	11.46	–0.13	11.49	–0.04(4)
			11.53	–0.20(5)	11.59	–0.16	11.57	–0.01(2)
	11.62	–0.18(3)	11.62	–0.04(7)	11.64	–0.07		
	11.75	–0.09(2)	11.70	–0.11(6)	11.73	–0.03	11.67	–0.02(3)
			11.80	–0.04(5)	11.82	–0.04		
	11.88	–0.15(3)	11.90	–0.07(3)	11.90	0.02	11.84	0.06(2)
	12.01	–0.17(3)	11.98	–0.05(5)	12.00	0.03	11.95	0.08(2)
			12.08	–0.09(5)	12.05	0.09		
$1a_{2u}(\pi)$							12.07	0.20(3)
	12.13	–0.16(3)	12.16	0.09(2)	12.16	0.18	12.19	0.23(2)
	12.26	–0.07(2)	12.24	0.25(5)	12.25	0.18		
			12.33	0.23(3)	12.32	0.13	12.31	0.18(4)
	12.39	0.00(3)	12.42	0.15(9)	12.38	0.11	12.44	0.19(4)
	12.51	–0.04(4)	12.52	0.01(5)	12.49	0.15		

Table 4.1 (Continued)

	This study		Sell *et al.*		Carlson *et al.*		Mattsson *et al.*	
Orbital	eBE	β	eBE	β	eBE	β	eBE	β
	12.63	–0.14(5)	12.60	0.14(5)	12.59	0.15	12.56	0.13(4)
			12.69	0.08(5)	12.65	0.16	12.68	0.19(4)
			12.77	0.00(7)	12.74	0.15		
					12.83	0.29		
					12.91	0.24		
					13.00	0.24		
$3e_{1u}(\sigma)$	13.82	0.11(4)	13.85	0.14(5)	13.89	0.20	13.85	0.34(5)
	13.93	0.17(3)	13.94	0.21(4)	14.00	0.25	14.00	0.32(6)
	14.04	0.20(2)	14.02	0.21(4)	14.06	0.22		
	14.15	0.14(2)	14.12	0.21(4)	14.17	0.20	14.14	0.28(5)
	14.26	0.08(2)	14.20	0.14(7)	14.26	0.19	14.27	0.23(5)
			14.30	0.11(2)	14.34	0.16		
	14.37	0.03(2)	14.38	0.07(5)	14.40	0.11	14.42	0.20(4)
	14.48	–0.03(2)	14.46	–0.05(5)	14.49	0.02		
$1b_{2u}(\sigma)$	14.59	–0.01(2)	14.55	–0.04(5)	14.58	–0.07	14.56	0.11(3)
			14.65	–0.20(4)	14.67	–0.20	14.68	–0.02(4)
	14.70	–0.01(2)	14.73	–0.29(4)	14.76	–0.24		
	14.81	–0.05(2)	14.83	–0.26(3)	14.84	–0.20	14.81	–0.11(4)
	14.91	–0.09(3)	14.91	–0.33(4)	14.94	–0.23	14.93	–0.10(4)
	15.02	–0.08(4)	14.99	–0.25(8)	14.98	–0.13		
			15.09	–0.19(5)	15.07	–0.07	15.05	0.00(5)
	15.12	0.02(4)	15.19	–0.08(13)	15.15	0.01	15.17	0.10(5)
	15.22	0.06(4)	15.27	–0.06(9)	15.25	0.02		

Table 4.1 (Continued)

	This study		Sell *et al.*		Carlson *et al.*		Mattsson *et al.*	
Orbital	eBE	β	eBE	β	eBE	β	eBE	β
$2b_{1u}(\sigma)$	15.32	0.11(4)	15.35	0.30(10)	15.34	0.07	15.28	0.27(6)
	15.43	0.16(5)	15.46	0.34(8)	15.41	0.19	15.40	0.45(6)
	15.53	0.18(5)	15.53	0.33(14)	15.50	0.33	15.52	0.43(5)
	15.63	0.18(5)	15.62	0.32(7)	15.62	0.33	15.63	0.40(6)
	15.72	0.15(6)	15.70	0.39(10)	15.74	0.25	15.74	0.42(5)
	15.82	0.20(7)	15.81	0.14(7)	15.84	0.34	15.84	0.49(4)
	15.92	0.23(6)	15.90	0.32(8)	15.91	0.42		
	16.01	0.24(6)	15.98	0.38 (12)	16.02	0.52	15.96	0.49(4)
			16.06	0.30(9)	16.07	0.52	16.07	0.46(5)
	16.11	0.19(8)	16.16	0.50(9)			16.19	0.57(7)
	16.20	0.09(9)	16.24	0.27(9)			16.30	0.49(8)
$3a_{1g}(\sigma)$	16.84	0.38(5)	16.83	0.14(11)			16.84	0.57(6)
	16.93	0.37(4)	16.91	0.45(4)	16.93	0.34	16.96	0.45(6)
	17.01	0.26(5)	16.99	0.38(7)	17.03	0.40		
			17.09	0.43(8)	17.07	0.37	17.07	0.39(9)
			17.19	0.21(4)	17.17	0.29	17.19	0.31(7)
			17.26	0.21(4)	17.25	0.33		
			17.34	0.30(10)	17.34	0.38	17.31	0.23(11)
			17.44	0.13(15)	17.42	0.21		
			17.52	0.30(8)				
$2e_{2g}(\sigma)$	18.89	–0.15(5)						
	18.95	–0.11(5)						
	19.01	–0.13(5)						
	19.07	–0.07(5)						

Table 4.1 (Continued)

	This study		Sell *et al.*		Carlson *et al.*		Mattsson *et al.*	
Orbital	eBE	β	eBE	β	eBE	β	eBE	β
	19.13	–0.09(5)						
	19.19	–0.16(5)			19.20	–0.06(12)[e]		
	19.25	–0.15(5)						
	19.31	–0.09(6)						
	19.37	–0.03(6)						

[a]The orbital assignments for benzene are those in ref. [19]. [b]Errors (±, in last digit unless indicated otherwise) given in parentheses. [c]The energy-dependent anisotropy parameters are reproduced from ref. [25]. [d]The energy-dependent anisotropy parameters are reproduced from ref. [19]. [e]β was determined by integrating over the area of the $2e_{2g}(\sigma)$ band. [f]Reference [24].

Table 4.2 Electron binding energy (in eV) and anisotropy parameters (β) for pyridine.

	this study		Utsunomiya *et al.*[c]		Piancastelli *et al.*[d]	
orbital[a]	eBE	β	eBE	β	eBE	β
$11a_1(n)$, $1a_2(\pi)$			9.26	0.19(6)	9.20	–0.08(5)
			9.36	0.30(3)	9.30	0.17(5)
			9.46	0.45(4)	9.40	0.07(5)
	9.58	–0.06(10)[b]	9.56	0.52(3)	9.50	0.27(5)
			9.66	0.56(1)	9.60	0.43(5)
	9.72	0.48(3)	9.73	0.61(1)	9.70	0.42(5)
	9.86	0.53(3)	9.80	0.65(2)	9.80	0.51(5)
			9.90	0.58(2)	9.90	0.42(5)
	10.00	0.40(5)	10.00	0.59(3)	10.00	0.47(5)
			10.10	0.58(6)	10.10	0.42(5)
$2b_1(\pi)$	10.42	0.49(6)				
	10.56	0.79(4)	10.54	0.91(3)		
	10.69	0.73(7)	10.64	0.77(2)		
			10.74	0.81(4)		
$7b_2(\sigma)$	12.39	–0.42(4)	12.37	–0.16(3)		
	12.51	–0.29(3)	12.48	–0.31(1)		
	12.63	–0.17(3)	12.65	–0.35(1)		
	12.75	–0.13(3)	12.75	–0.14(7)		
	12.88	–0.05(3)				
$1b_1(\pi)$	13.00	0.07(3)	13.07	0.12(4)		
	13.12	0.15(3)	13.17	0.26(3)		
	13.23	0.17(3)	13.27	0.27(6)		

Table 4.2 (Continued)

	this study		Utsunomiya *et al.*		Piancastelli *et al.*	
orbital	eBE	β	eBE	β	eBE	β
	13.35	0.06(3)	13.37	0.27(2)		
	13.47	0.00(3)	13.47	0.37(3)		
	13.59	0.00(3)				
$10a_1(\sigma)$	13.70	0.01(3)				
	13.82	0.07(2)				
	13.93	0.06(2)				
	14.04	0.09(3)				
	14.15	0.11(3)				
$6b_2(\sigma)$	14.26	0.19(3)				
	14.37	0.29(2)				
	14.48	0.31(2)				
	14.59	0.32(2)				
	14.70	0.26(3)				
	14.81	0.23(4)				
	14.91	0.26(4)				
	15.02	0.25(4)				
	15.12	0.23(5)				
$5b_2(\sigma)$,	15.22	0.05(5)				
	15.32	-0.13(6)				
	15.43	-0.15(5)				
	15.53	-0.11(4)				
	15.63	–0.10(3)				
	15.72	–0.16(2)				

Table 4.2 (Continued)

	this study		Utsunomiya *et al.*		Piancastelli *et al.*	
orbital	eBE	β	eBE	β	eBE	β
	15.82	–0.16(3)				
	15.92	–0.18(3)				
	16.01	–0.14(4)				
	16.11	–0.07(4)				
	16.20	–0.04(4)				
	16.30	-0.08(4)				
	16.39	-0.16(5)				
	16.48	-0.18(5)				
	16.57	-0.15(7)				
$8a_1(\sigma)$	16.66	0.00(6)				
	16.75	0.14(6)				
	16.84	0.25(6)				
	16.93	0.32(5)				
	17.01	0.30(4)				
	17.10	035(4)				
	17.18	0.43(5)				
	17.27	0.44(6)				
	17.35	0.38(6)				
	17.43	0.20(5)				
$7a_1(\sigma)$	19.54	0.07(7)				
	19.59	0.01(8)				
	19.64	0.00(8)				
	19.69	0.11(7)				
	19.75	0.15(8)				

[a]The orbital assignments for benzene are those made in ref. [44]. [b]Errors (±, in last digit unless indicated otherwise) given in parentheses. [c]Reference [41]. [d]The energy-dependent anisotropy parameters are reproduced from ref. [42].

4.4 References

[1] Turner, D. W. *et al*. *Molecular Photoelectron Spectroscopy*, Wiley-Interscience, London, **1970**.

[2] Asbrink, L.; Edqvist, E.; Lindholm, E.; Selin, L. E. *Chem. Phys. Lett*. **1970**, *5*, 192.

[3] Asbrink, L.; Lindholm, E.; Edqvist, O. *Chem. Phys. Lett*. **1970**, *5*, 609.

[4] Carlson T. A.; Anderson, C. P. *Chem. Phys. Lett*. **1971**, *10*, 561.

[5] Potts, A. W. *et al*. *Faraday Discuss. Chem. Soc*. **1972**, *54*, 168.

[6] Lindholm, E. *Faraday Discuss. Chem. Soc*. **1972**, *54*, 200.

[7] Clark, P. A.; Brogli, F.; Heilbronner, E. *Helv. Chim. Acta* **1972**, *55*, 1415.

[8] Streets, d. G.; Potts, A. W. *J. Chem. Soc. Faraday Trans. II* **1974**, *70* ,1505.

[9] Kobayashi, T.; Nagakura, S. *J. Electron Spectrosc. Relat. Phenom*. **1975**, *16*, 221.

[10] Karsson, L. *et al*. *Physica scripta* **1976**, *14*, 230.

[11] Mattsson, l. *et al. Physica scripta* **1977**, *16*, 149.

[12] Sell, J. A.; Kupperman, A. *Chem. Phys*. **1978**, *33*, 367.

[13] Bieri, G.; Asbrink, L. *J. Electron Spectrosc. Relat. Phenom*. **1980**, *20*, 149.

[14] Kimura, K. *et al. Handbook of HeI Photoelectron Spectra of Fundamental Organic Molecules*, Japan Scientific Societies press, Tokyo, **1981**.

[15] Gelius, U. *et al. J. Electron Spectrosc. Relat. Phenom*. **1974**, *2*, 405.

[16] Gelius, U. *et al. J. Electron Spectrosc. Relat. Phenom* **1974**, *5*, 985.

[17] Kinsinger, J. A.; Taylor, J. W. *Int. J. Mass Spectrom. Ion Phys*. **1972**, *10*, 445.

[18] Mehaffy, D. *et al. J. Electron Spectrosc. Relat. Phenom*. **1983**, *28*, 239.

[19] Carlson, T. A. *et al. J. Chem. Phys*. **1987**, *86*, 6918.

[20] Baltzer, P. *et al. Chem. Phys.* **1997**, *224*, 95.

[21] Gelius, U. *et al. Phys. Scr*. **1971**, *3*, 237.

[22] Brundle, C. R.; Robin, M. B.; Kuebler, N. A. *J. Am. Chem. Soc*. **1972**, *94*, 1466.

[23] Price, W. C. *Faraday Discuss. Chem. Soc*. **1972**, *54*, 205.

[24] Mattsson, L. *et al. Physica Scripta* **1977**, *16*, 221.

[25] Sell, J. A.; Kuppermann, A. *Chem. Phys.* **1978**, *33*, 367.

[26] Carlson T. A. *et al. J. Chem. Phys*. **1987**, *86*, 6918.

[27] Baltzer, P. *et al. Chem. Phys*. **1997**, *224*, 95.

[28] Jonsson, B. O.; Lindholm, E. *Ark. Fys*. **1969**, *39*, 65.

[29] Krause, H.; Ernstberger, B.; Neusser, H. J. *Chem. Phys. Lett.* **1991**, *184*, 411.

[30] Shiromaru, H.; Katsumata, S. *Bull. Chem. Soc. Jpn*. **1984**, *57*, 3543.

[31] Suzuki, Y.; Suzuki, T. *J. Phys. Cham. A* **2008**, *112*, 402.

[32] EL Sayed, M. F. A.; Kasha, M.; Tanaka, Y. *J. Chem. Phys*. **1961**, *34*, 334.

[33] Jonsson, B. O.; Lindholm, E.; Skerbele, A. *Int. J. Mass Spectrom. Ion Phys*. **1969** *3*, 385.

[34] Jacqueline, O. Berg; Parker, D. H.; El-Sayed, M. A. *Chem. Phys. Lett*. **1978**, *56*, 411.

[35] Baker, A. D.; Turner, D. W. *Phil. Trans. Roy. Soc. London. Ser. A* **1970**, *268*, 131.

[36] Dewar, M. J. S.; Worley, S. D. *J. Chem Phys*. **1969**, *51*, 263.

[37] Gleiter, R.; Heilbronner, E.; Hornung, V. *Angew. Chem*. **1970**, *82*, 878.

[38] Asbrink, L.; Fridh, C.; Lindholm, E. *Chem. Phys. Lett*. **1977**, *52*, 69.

[39] Karlsson, L. *et al*. *Chem. Scr* **1974** *6*, 214.

[40] Gleiter, R.; Heilbronner, E. Hornug, V. *Helv. Chim. Acta* **1972**, *55*, 255.

[41] Utsumoniya, C.; Kobayashi, T. Nagakura, S. *Bull. Chem. Soc. Jpn*. **1978**, *51*, 3482.

[42] Piancastelli, M. N. *et al*. *J. Am. Chem. Soc.* **1983**, *105*, 4235.

[43] Moghaddam, M. S. *et al*. *Chem. Phys.* **1996**, *207*, 19.

[44] Wan, J.; Hada, M.; Ehara, M.; Nakatsuji, H. *J. Chem. Phys.* **2001**, *114*, 5117.

[45] Plashkevych, O. *et al. J. Electron Spectrosc. Relat. Phenom.* **2000**, *106*, 51.

[46] Lorentzon, J.; Fülscher, M. P.; Roos, B. O. *Theor. Chim. Acta* **1995**, *92*, 67.

[47] Walker, I. C.; Palmer, M. H.; Hopkirk, A. *Chem. Phys.* **1990**, *141*, 365.

Chapter 5

Time-resolved PEI of Pyrazine using a fs-UV Laser and a VUV FEL

The first time-resolved photoelectron imaging using a vacuum ultraviolet free-electron laser and a femtosecond ultraviolet laser is presented. The key instrument for this achievement is the photoelectron imaging spectrometer developed using He(I) light source. Ultrafast internal conversion (IC) and intersystem crossing (ISC) in pyrazine in a supersonic molecular beam are discussed in terms of the observed time profiles of photoelectron intensity and kinetic energy distribution.

5.1 Introduction

The ultrafast pump-probe spectroscopy (Fig. 5.1) enables us to study real-time dynamics of chemical reactions. In this method, a pump laser pulse prepares molecules in an excited electronic state and a probe pulse interrogates their time evolution with various spectroscopic methods.[1] Transient absorption and fluorescence up-conversion techniques are often used as the probing method in the condensed-phase, while gas-phase studies of molecules and clusters usually use laser-induced fluorescence or photoionization (including single photon and resonant multiphoton ionization) because of their high sensitivity. However, photoionization has the following advantages over laser induced fluorescence. Firstly, ionization allows observation of dark states with extremely low fluorescence quantum yields; therefore, it enables observation of intersystem crossing (ISC) to triplet states and internal conversion (IC) to the ground electronic state. Secondly, ionization detection is extremely sensitive, since

photoionization is an induced process and the photoelectrons can be collected efficiently by an electromagnetic field. Thus, I use pump-probe time-resolved photoelectron spectroscopy (TRPES) to study real-time dynamics of molecules.

As I have already described in earlier chapters, photoelectron imaging (PEI) enables efficient and accurate measurements of the photoelectron kinetic energy (PKE) and photoelectron angular distribution (PAD). The latter is important for elucidation of the characters of the electronic states involved in the dynamics. The time-resolved photoelectron imaging (TRPEI) has already been used extensively in studying ultrafast electronic dynamics in photoexcited molecules.[2,3] However, what is novel in this work is the use of a femtosecond vacuum ultraviolet laser free electron laser (VUV-FEL) for photoionization.

It is noted that TRPES using UV photons sometimes had difficulty in observation of the excited-state molecules when they undergo molecular deformation of a large scale. For example, recent TRPES of isolated DNA bases have observed femtosecond (fs) or picosecond (ps) decays of photoionization signals, which were interpreted as ultrafast electronic deactivations; [4,5,6] however, theoretical calculations have suggested that the decays were owing to rapid increase of the effective ionization energy caused by molecular deformation that stabilize and destabilize the neutral and ionic state, respectively. TRPES with a VUV or extreme UV (EUV) probe lasers would avoid such confusion and allow clear observation of ultrafast electronic dynamics and photochemical reactions.[7]

The VUV light source I use in this study is VUV-FEL named SCSS (SPring-8 compact self-amplification of spontaneous emission source) at RIKEN Harima instate. SCSS is usually operated at 51–61 nm, and its maximum pulse energy and pulse duration are 30 μJ/pulse and sub-picosecond, respectively. On the other hand, the drawback of the VUV-FEL is its low repetition rate, 20 – 30 Hz. The advantage of PEI is that its ultimate detection solid angle of photoelectrons compensates the low repetition rate and makes possible to perform pump-probe experiments in acceptable data acquisition time (eg. one photoelectron image /

hour).

Although pump-probe experiments using a femtosecond laser and an EUV FEL (Hamburg; FLASH) have been reported,[8-12] these previous studies were limited to nonlinear optical processes of atoms induced by a Ti:sapphire laser (800 nm) and an FEL. As far as I know, the study presented in this chapter is the first UV pump – VUV-FEL probe experiment on chemical dynamics of polyatomic molecules.

5.2 One-photon ionization by SASE-FEL

5.2.1 SPring-8 Compact SASE Source

SCSS[13] (Spring-8 compact self-amplification of spontaneous emission (SASE) source) was constructed as a prototype of X-ray FEL (XFEL). SCSS emits radiation in the VUV to EUV regions.[14] Figure 5.2 shows a schematic configuration of SCSS that comprises of an ultralow-emittance electron gun, C-band accelerator and two-stage in-vacuum undulator. The electron beam (500 keV) from the electron gun is accelerated to 250 MeV in tandem C-band accelerators, and a beam halo is removed by a chicane. In the first section of the undulator, spontaneous emission of radiation occurs from the electrons and it serves as seed radiation for induced emission in the main part of the undulator. Thus, spontaneous emission of radiation is amplified. Since the spontaneous emission of radiation is stochastic, Self-Amplification of Spontaneous Emission of radiation (SASE) inherently has fluctuation in wavelength and energy. SASE is used because there is no good optical mirror to construct a laser cavity in the EUV to X-ray regions. The characteristics of SCSS[14] are summarized as follows:

Pulse energy :	>10 mJ @61 nm
Intensity fluctuation:	<20 %
Wavelength range:	50-61 nm
Spectral width:	<1 % (FWHM)
Pulse width:	sub ps
Polarization:	linear >99 %
Repetition rate:	20 Hz (max. 60 Hz）
Harmonics:	2nd H. < 0.1 %, 3rd H. < 1 %

5.2.2 Suppression of background photoemission using newly designed electrode system

Since the coherent VUV-FEL beam can be focused tightly, background photoemission induced by scattered light are much less than in the case of He(I) radiation. However, we found that the conventional three-plate electrostatic lens reported by Eppink and Parker[15] generates considerable background electrons even with FEL, as shown in Fig. 5.3 (a) and (b). On the other hand, the background signal was almost completely eliminated by our new electrostatic lens, as shown in Fig. 5.3 (c): notice that it is a raw image without background subtraction. The background signal that still remains in Fig. 5.3 (c) is due to photoelectron from residual water vapor in the vacuum chamber and not background photoemission from the apparatus. Water vapor pressure can be reduced considerably by baking the entire vacuum chamber for a week; therefore, it is possible to eliminate photoelectron signals from water vapor. However, in practice, a severely limited beam time of SCSS did not allow us to bake the chamber prior to the experiment unfortunately.

5.2.3 Comparison of PEI with He(I) and SASE-FEL

As discussed in detail in Chapter 3, the resolution of He(I) PEI is limited by a large ionization volume. On the other hand, the VUV-FEL beam can be focused to a diameter of ~ 0.1 mm. Our trajectory calculations indicate that the electron lens system is capable of providing the energy resolution $\Delta E/E$ of 0.04 % at 5.461 eV, if an ionization volume is 0.1 mmϕ × 3.4 mm. The resolution of 0.04 % reaches the ultimate resolution, 0.06 %, obtainable with the best commercial MCP (70 mm in diameter and 10 μm in pore size). The proof of the ultimately high resolution of our PEI apparatus awaits an experiment with nanosecond UV lasers.

However, as shown in Figure 5.4, photoelectron kinetic energy distributions of Kr measured with FEL radiation (wavelength 58.4 nm) is broader than that with measured He(I) radiation under the same experimental condition; the FWHM of the peak at 7.22 eV (indicated by * in Fig. 5.4) is 246 meV with He(I) and 298 meV with FEL. In both cases, a high-resolution CCD camera (2048 × 2048) was used without centroiding calculation. The inferior resolution with FEL, in spite of its smaller ionization volume, is ascribed to a large effective bandwidth (0.1 eV) of SASE.[14]

Figure 5.5 shows a photoelectron image of pyridine with FEL at 58.4 nm and the photoelectron spectra extracted from the image. Since FEL radiation is polarized, the photoelectron distribution is cylindrically symmetric about its polarization direction (indicated by the arrow in the Fig.5.5). Similarly with Kr, the image shown in Fig. 5.5 exhibit broader structures than Fig. 4.3 measured with He(I).

One of the advantages of VUV-FEL over He(I) is much higher photon density. However, the pulse energy of the SCSS radiation is too high for single-photon ionization experiments. We had to reduce pulse energy with metal and gas filters to avoid multiphoton ionization. Since SCSS is operated at a low repetition rate (20–30 Hz), the reduction of pulse energy diminishes the advantage of VUV-FEL over He(I) for conventional UPS. In the next section,

we utilize another important advantage of VUV-FEL, namely the ultrashort pulse duration, for pump-probe experiments.

5.3 (1 + 1') pump-probe experiment of pyrazine

5.3.1 Introduction

Pyrazine ($C_4H_4N_2$, 1,4-diazabenzene) is a heterocyclic aromatic molecule that belongs to the D_{2h} point group. The S_2-S_0 absorption spectrum of pyrazine in the deep UV region (230–270 nm) exhibits a broad feature,[16] which implies ultrafast decay of the S_2 state. Low-lying conical intersection (CI) between the S_2 and S_1 potential energy surfaces was identified by semiempirical calculations.[17] Thereafter, extensive *ab initio* calculations have been performed to characterize S_2/S_1 CI more precisely,[18,19] and it has been established that the S_2/S_1 CI is located at the bottom of the S_2 diabatic PES. Thus, the ultrafast decay from S_2 has been established as the internal conversion through CI, as shown in fig. 5.6 (a). For observation of this ultrafast dynamics in real time, TRPES of pyrazine has been proposed by theoretical simulations.[20,21,22] However, the time constant of the internal conversion is predicted to be only less than 30 fs.[23,24] Such high time-resolution has been hardly realized in the pump-probe experiments in deep UV region. For instance, Wang *et al.*[25] performed the first femtosecond [1+2'] TRPEI of pyrazine to study this internal conversion; however, their time-resolution (450 fs) did not allow observation of ultrafast decay from S_2 to S_1, and they observed only the decay of S_1 after internal conversion from S_2. The S_1-S_0 decay time constant was 22 ps. Stert *et al.*[26] performed a similar experiment. Very recently, TRPEI of pyrazine was performed with sub-20 fs deep UV pulse in our laboratory, and the time constant of the $S_2 \rightarrow S_1$ internal conversion was experimentally determined as 22 fs.[27,28]

The $S_1 \rightarrow T_1$ ($n\pi^*$) ISC in pyrazine is also well known as the intermediate coupling case in molecular radiationless transition. Frad *et al.*[29] and Lahmani *et al.*[30] observed ISC as a biexponential fluorescence decay, in which the fast component corresponds to ISC. The biexponential fluorescence decay was extensively studied in the 1980s and a debate ensued as to whether the observed fast component was due to the predicted dephasing or Rayleigh–Raman light scattering.[16,31,32] The presence of a fast component and its finite lifetime have been unambiguously proved by picosecond laser spectroscopy. Although fluorescence studies only observed the decay of the singlet state, TR-PEI allowed detection of both S_1 and T_1 states involved in ISC in pyrazine by (1+2') resonance enhanced multiphoton ionization (REMPI)[25,33,34] and (1+1') REMPI.[35] In the latter, pyrazine was excited to 0^0 level of S_1 with a 324 nm femtosecond pump pulse and subsequently ionized with a 197 nm femtosecond probe pulse. Ionization from the S_1 zero vibrational level occurred to low vibrational states of cation, due to Franck–Condon principle, creating rapid electrons, whereas ionization from high vibrational levels of the triplet state created slow electrons, as shown in Fig. 5.6 (b). TR-PEI clearly demonstrated a rapid decay of the ionization component from S_1 and a growth of that from T_1 with a clear isosbestic point in the time-dependent photoelectron spectra. The lifetime of S_1 was estimated to be 110 ps.

We revisited internal conversion and ISC in pyrazine by TRPEI using VUV-FEL.

5.3.2 Experimental setup

Figure 5.7 shows the experiment setup for pump-probe experiments using a fs UV laser and a VUV FEL. The vacuum chamber and PEI spectrometer are the same as He(I) experiment described in chapters 2 and 3. A pulsed supersonic molecular beam of 10 % pyrazine ($C_4H_4N_2$) seeded in He was introduced into a photoionization chamber and crossed with a femtosecond UV laser pulse and a VUV FEL pulse (161 nm). The UV laser at 324 or 260 nm excited pyrazine to the first or second excited singlet state (S_1 of S_2), respectively, and

the VUV laser ionizes molecules from the excited states. Electrons generated by (1+1') REMPI were accelerated along the molecular beam propagation axis and projected onto a position-sensitive detector comprising 10-μm pore MCPs, a phosphor screen (P47), and a CCD camera (512 × 512 pixels). Light baffles were used at the entrance and exit ports of the laser beams to reduce scattered light.

The femtosecond laser system comprises an oscillator, a regenerative amplifier, and an optical parametric amplifier (OPA). The laser system was operated at 1 kHz, and a pulse picker was used to gate a pulse train from the OPA. Although the gate width of our pulse picker was long to allow two consecutive pulses separated by 1 ms to pass through each gate, background subtraction eliminated any interference from this additional pulse. The UV laser pulse was introduced into the vacuum chamber through an optical path length of about 10 m. The laser beam was focused with an axisymmetric lens placed in the air and reflected with an aluminum mirror inside the vacuum chamber to the molecular beam. The timing of the laser pulse was synchronized to the 238-MHz master clock of SCSS by feedback locking the cavity length of the Ti:Sapphire oscillator. The time delay between the laser and SCSS pulses was varied electronically with an expected accuracy in sub-ps and the temporal overlapping of them is monitored by the high speed photodiode.

The SCSS is typically operated at 51–61 nm with electron beam energy of 250 MeV;[14] however, 61-nm radiation can directly ionize the molecule without the pump light, which makes the observation of two-color REMPI signal highly difficult. Therefore, in this study, we used 161 nm radiation to perform the pump-probe experiment. The VUV radiation intensity was attenuated to be less than 1 μJ/pulse with a gas filter using air as a medium. The beam size was controlled by two slits placed before the focusing mirror (see Fig. 5.7), and the VUV radiation was finally focused onto the molecular beam using a pair of elliptical and cylindrical mirrors. The repetition rate of the whole system was 20 Hz. The crossing angle between the femtosecond laser and FEL beams was 1 degree. The polarization direction of

UV and VUV pulses was parallel to the face of the MCP detector. Owing to the characteristics of SASE,[14] the time-averaged spectrum of 161 nm radiation had an energy width (FWHM) of ~ 0.1 eV.

5.3.3 Spatial overlapping between UV and VUV FEL

The spatial overlap of the pump and probe laser beams at the interaction region is crucial in two-color experiments. We have taken the advantage of the imaging apparatus and overlapped the two laser beams precisely by monitoring the image and TOF of photoions. Pyrazine in the molecular beam was ionized by one-color 2-photon ionization using either pump or probe laser. The intensities of both lasers were increased for the alignment. The photoion signals were observed by changing the polarity of the voltages applied to the electrodes from that for electron detection. The crossing point of the laser beam with the flight tube axis was determined from the TOF of photoions. This was because the arrival time of the ion depends on the distance of the ionization point from the repeller. As the ionization point is closer to the MCP detector, it is farther away from the repeller and the ion gains less kinetic energy in the electric field. This leads to a smaller speed of ion in the field free region and consequently a longer flight time of the ion. Figure 5.8 (a) and (b) show the mass spectra of pyrazine observed by 161-nm FEL radiation and 260-nm UV radiation, respectively. The parent ion signal is used as an indicator of the overlap of the laser beams. Since the VUV-FEL beam cannot be moved in the laboratory, the position of the UV laser beam was adjusted to overlap with the VUV beam.

To overlap the two beams in the plane perpendicular to the flight axis, the arrival positions of ions on the MCP detector were imaged by the CCD camera. Figure 5.9 (a) and (b) show the ion image of pyrazine observed by 161-nm FEL radiation and 260-nm UV radiation, respectively. The UV laser beam direction was changed by moving a focusing lens until the ion image created by a UV laser overlaps with that by a VUV-FEL.

5.3.4 Results

(A) S_1–S_0 Internal Conversion (IC)

Figure 5.10 (a) shows a time profile of the pyrazine ion observed by (1+1') REMPI with 260-nm pump and 161-nm probe pulses. The pump pulse excited pyrazine from S_0 to S_2. It is ideal that each pulse does not produce any ionization signal to have high contrast ratio of the two-color signal against the one-color signals. However, the pump pulse created a small amount of one-color two-photon ionization signal. 161 nm is also resonant with an electronic transition.[36] Therefore, one-color two-photon ionization signals were observed for both pump and probe pulses. However, the sum of these one-color signals is still 3–4 times smaller than the two-color signal, and was already subtracted in Fig. 5.10. Least-squares fitting of the time profile by assuming a single exponential decay yielded a lifetime of ~ 20 ± 3 ps. Previously, TRPEI by Horio *et al.*[27] using 264-nm pump and 198-nm probe have shown that the S_2 state dephases to S_1 in ~ 23 fs, and TRPEI by Wang et al. reported that these S_1 state decays in ca. 22 ps.[25,26] Owing to a limited time resolution (< 5 ps) of this experiment, the ultrafast S_2–S_1 internal conversion within 30 fs cannot be observed. The time constant of the decay of ionization signal is in good agreement with the lifetime of hot S_1 state reported by Wang et al. The lifetime of these highly vibrationally excited S_1 molecules are determined by IC to the S_0 state.[16]

Figure 5.10 (b) shows a photoelectron image observed at the delay time of about 5 ps. In a [1+1'] pump and probe ionization experiment with laser polarization vectors parallel to each other, the photoelectron angular distribution (PAD) is characterized by:

$$I(\theta) = \frac{\sigma}{4\pi}\left[1 + \beta_2 P_2(\cos\theta) + \beta_4 P_4(\cos\theta)\right]$$

where P_n is the n-th order Legendre polynomial, θ is the angle between the photoelectron velocity and the linear polarization of the laser, β_n is anisotropy parameter. The least-squares fitting of the photoelectron angular distribution extracted from Fig. 5.10 (b) provides β_2 =

-0.15 ± 0.05 and $\beta_4 = -0.03 \pm 0.10$. The low anisotropy is typical for valence excited states of molecules.

The photoelectron kinetic energy distribution (PKED) extracted from Fig. 5.10 (b) is showed in Fig. 5.11 (a). Comparing with the previous study with 264-nm UV pump and 198-nm DUV probe (red curve in Fig. 5.11a), the advantage of 161-nm VUV radiation over 198-nm DUV light is clear. With the latter, the observed distribution is truncated around its maximum at the electron binding energy (EBE) of 10.96 eV. In contrast, the entire Franck-Condon envelope is observed with the former. The high-resolution He(I) photoelectron spectrum of jet-cooled pyrazine adopted from Oku *et al.*[37] is also shown in Fig. 5.11 (a). Their spectrum indicates that the first ionization energy is 9.29 eV, while our PKED exhibits a peak at ca. 10.6 eV. The $S_2 \rightarrow S_1$ IC transforms the difference of the electronic energies of S_2 and S_1, 0.86 eV, into the vibrational energy in S_1. This energy is approximately conserved upon ionization, which shifts the peak nearly 1 eV (Fig. 5.11 (b)). The S_1 state has an electronic configuration of (n, π^*), whereas the D_0 and D_1 states are of n^{-1} and π^{-1}. Therefore, frozen core approximation predicts that ionization from S_1 predominantly occurs to D_0. This experiment clearly shows that ionization from S_1 to D_1 is actually minor, if present.

(B) S_1–T_1 Intersystem Crossing (ISC)

Figure 5.12 (a) shows the ionization signal upon the 324-nm pump and 161-nm probe excitation. The signal exhibits an initial decay, due to S_1-T_1 ISC, and reaches a plateau at later time: the least squares fitting of the decay curve yields the lifetime of S_1 state as 114 ± 17 ps, which is consistent with the previous reports (110 ps).[31,33,34] Figure 5.12 (b) shows the PKEDs and the photoelectron (Abel-inverted) images observed at 8, 58 and 408 ps. A 8 ps, photoelectron signal from the S_1 state appears clearly as the outer ring, whereas it diminished at longer time delays (408 ps) due to S_1–T_1 ISC. Previous studies concluded that the S_1 state dephases exclusively to T_1. Therefore, we anticipated that ionization occurs with similar

efficiencies from S_1 and T_1 at 161 nm, and that the total ionization intensity does not diminish. The observed decay, which contradicts with our expectation, may suggest that T_1 state has some deactivation processes and its population is lost. From the energy resolution of our PEI spectrometer and the broad bandwidth (0.1 eV) of SCSS, the energy resolution of PKED is estimated to be 0.2-0.3 eV. Accordingly, no distinct vibrational structure is discernible.

5.4 Conclusion

The new PEI spectrometer described in earlier chapters has been used for PEI with a VUV-FEL. The background electrons observed with a conventional three-plate electrostatic lens were almost completely eliminated by our new lens. Owing to the characteristics of SASE, the resolution was inferior with VUV-FEL to that with He(I). However, we utilized the short pulse duration of the VUV-FEL for the first time-resolved photoelectron imaging of polyatomic molecules by synchronization with a fs tunable UV laser. The time evolution of photoelectron intensity and photoelectron images clearly exhibited the features of ultrafast S_1–T_1 intersystem crossing and S_1–S_0 internal conversion in pyrazine in a supersonic molecular beam. This study clearly demonstrates the feasibility of picosecond TRPEI of photo-induced dynamics of large polyatomic molecules with an FEL and a tunable UV laser.

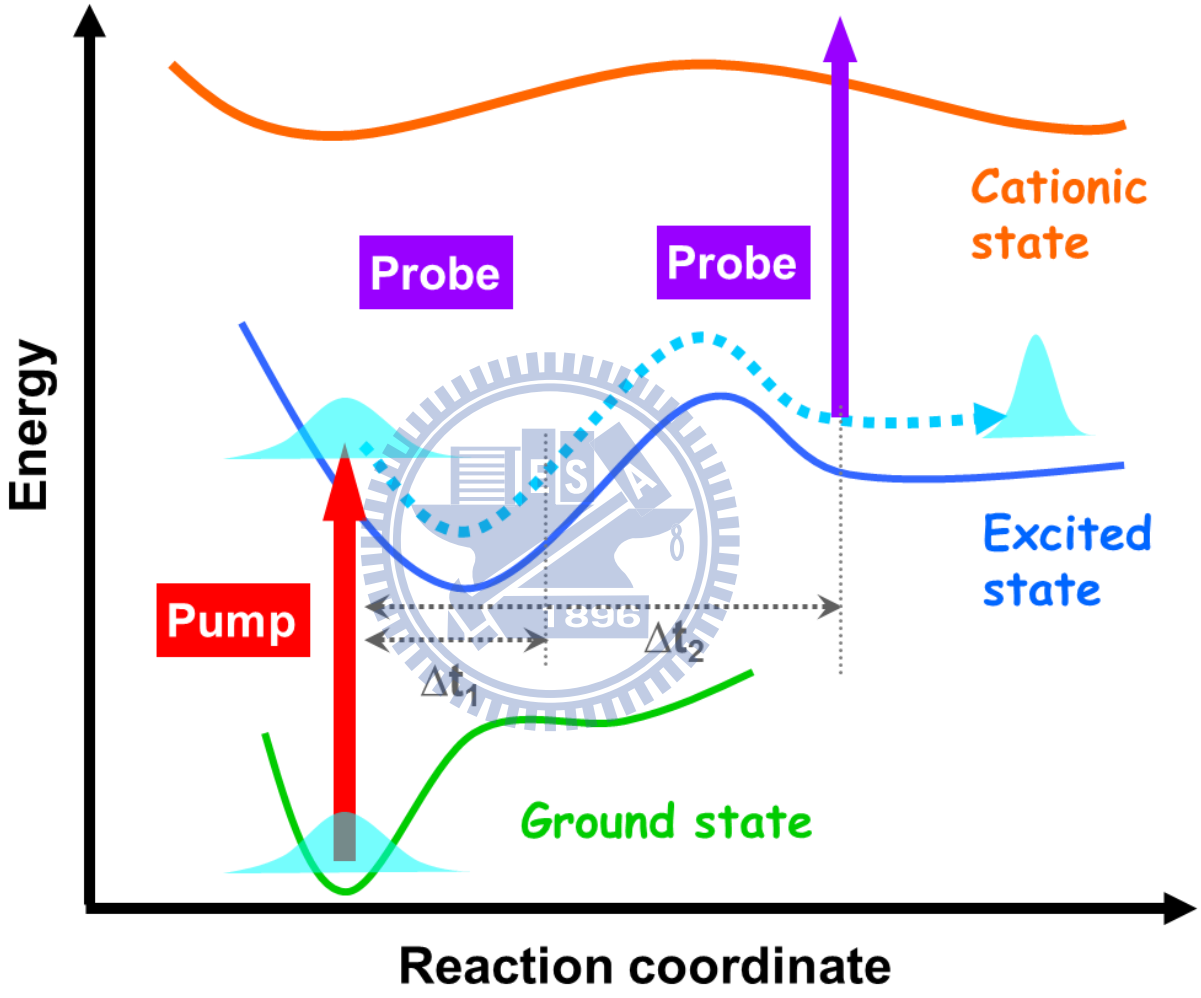

Figure 5.1 Schematic illustration of the principle of a pump-probe experiment with ionization for probing. The pump pulse excites an electronic state and after some delay (eg. Δt_1, Δt_2) the probe pulse ionizes the excited neutral molecule.

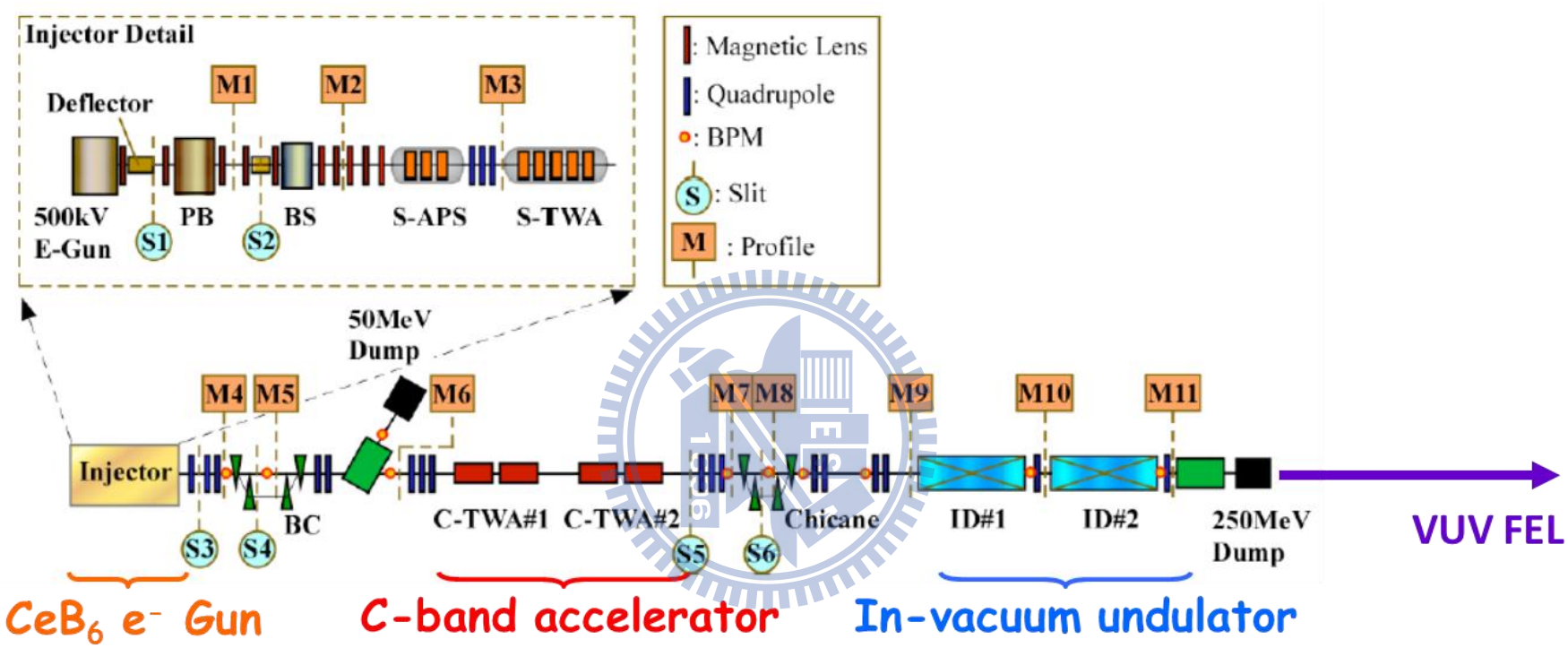

Figure 5.2 Schematic configuration of the SCSS test accelerator extracted from ref. 13.

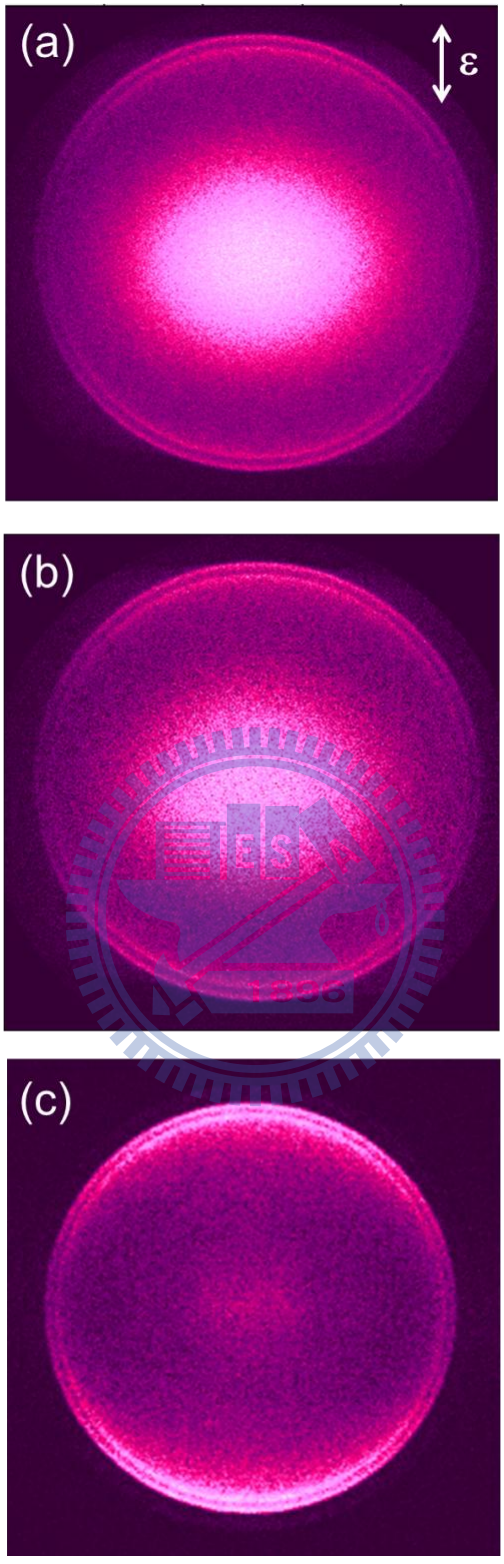

Figure 5.3 Photoelectron image observed for photoionization of a pulsed supersonic beam of Kr at a stagnation pressure of 0.1 MPa with FEL (60 nm) using a conventional three-plate electrostatic lens: (a) before and (b) after background subtraction. (c) Photoelectron image of Kr measured with newly-design electrostatic lens. No background image was subtracted.

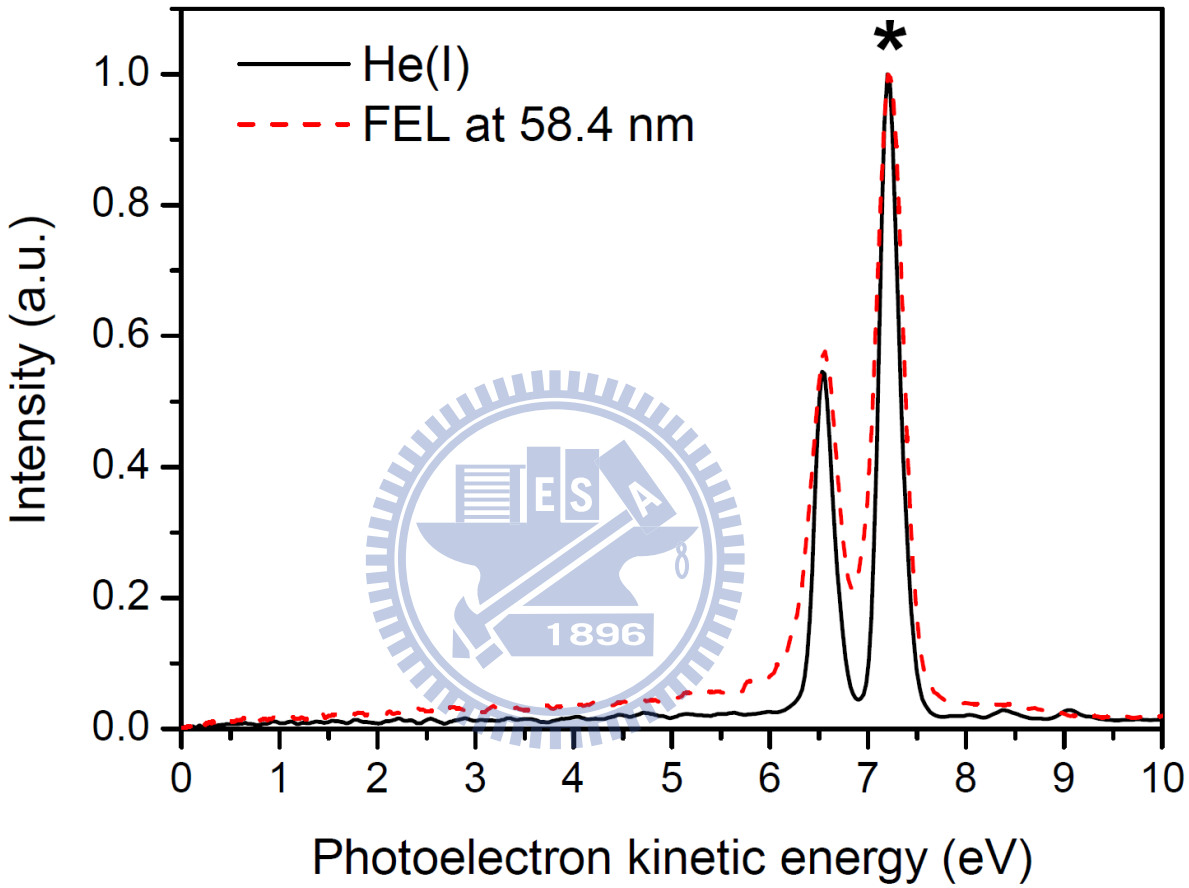

Figure 5.4 Comparison of PKE distributions of Kr in photoionization by He(I) radiation (solid) and FEL radiation (wavelength: 58.4 nm) (dashed).

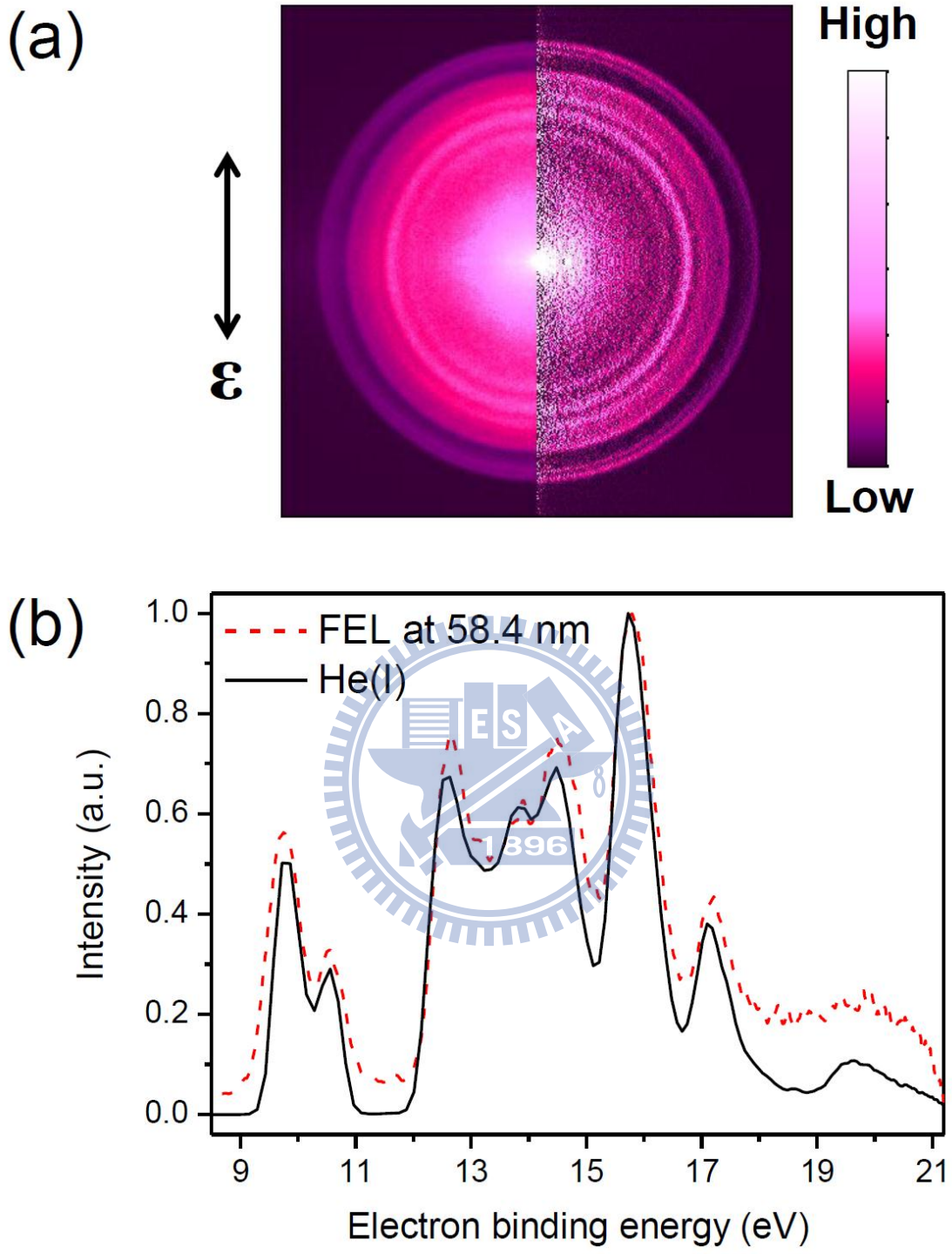

Figure 5.5 (a) Symmetrized photoelectron image observed for photoionization of a pulsed supersonic beam of 10 % pyridine seeded in He with FEL (λ = 58.4 nm). The left half is the raw image, whereas the right half is the slice image obtained by taking the inverse Abel transform. (b) Comparison of the photoelectron spectra extracted from the image obtained using FEL in Fig. 8(a) (dash) with the photoelectron spectrum obtained using He(I) (solid) measured with a 512 × 512 pixels CCD camera.

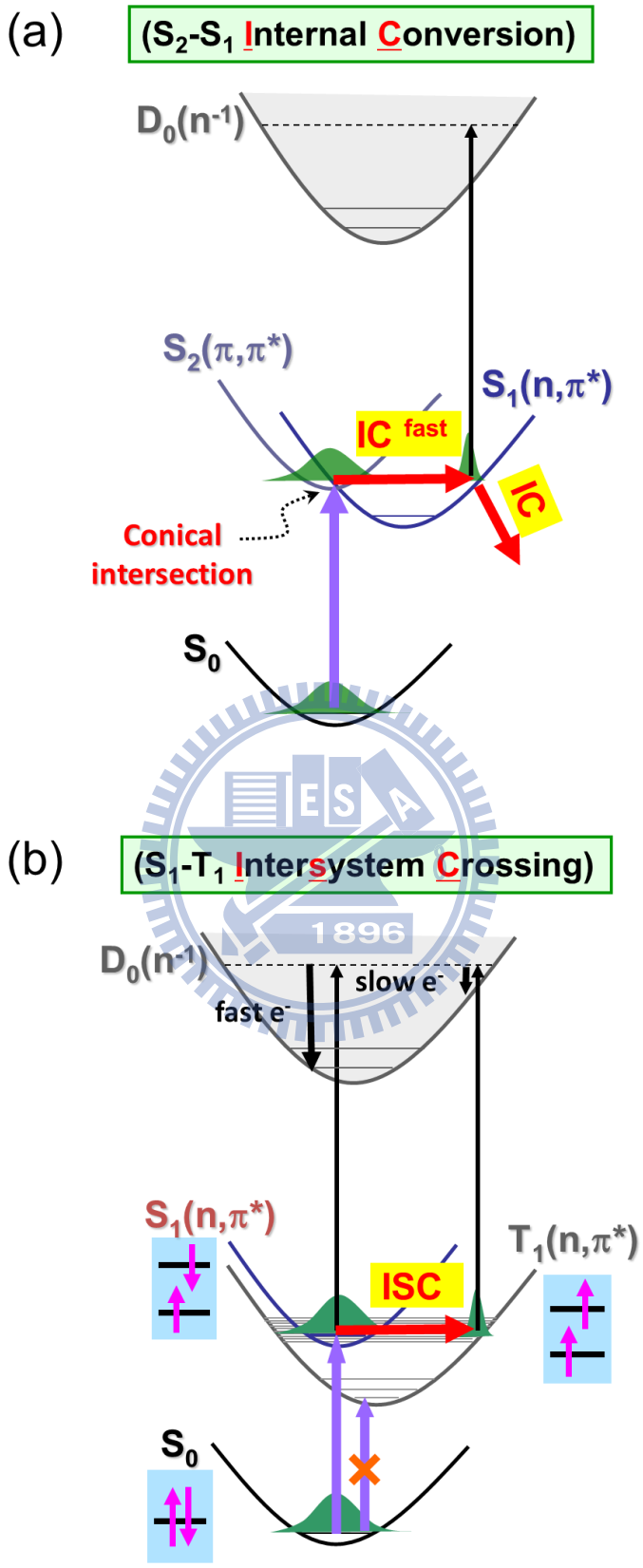

Figure 5.6 Schematic energy diagram of (a) S_2–S_1 internal conversion (IC) and (b) S_1–T_1 intersystem crossing (ISC) in pyrazine.

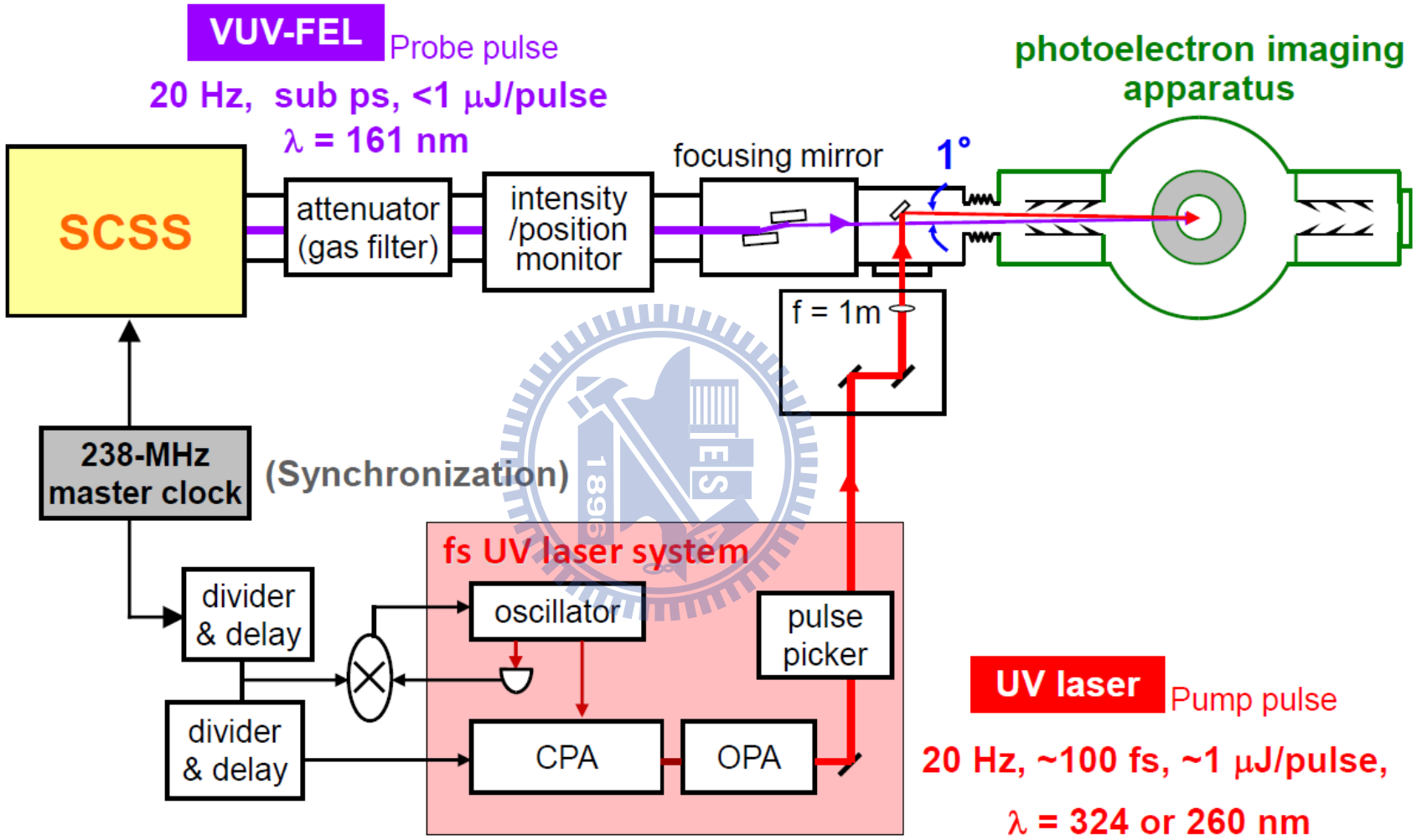

Figure 5.7 The setup for pump-probe experiment using a fs UV laser and a VUV free-electron laser.

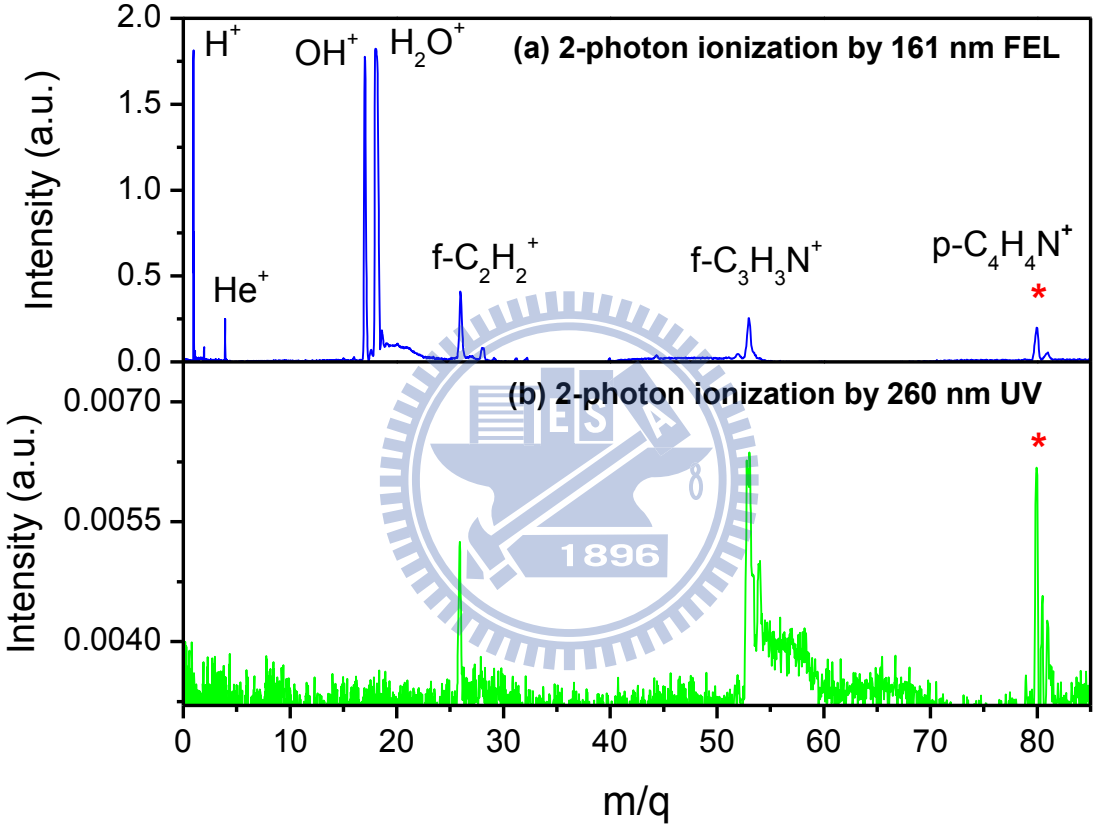

Figure 5.8 Mass spectrum of pyrazine obtained from: (a) 2-photon ionization by 161-nm FEL; (b) 2-photon ionization by 260-nm UV laser.

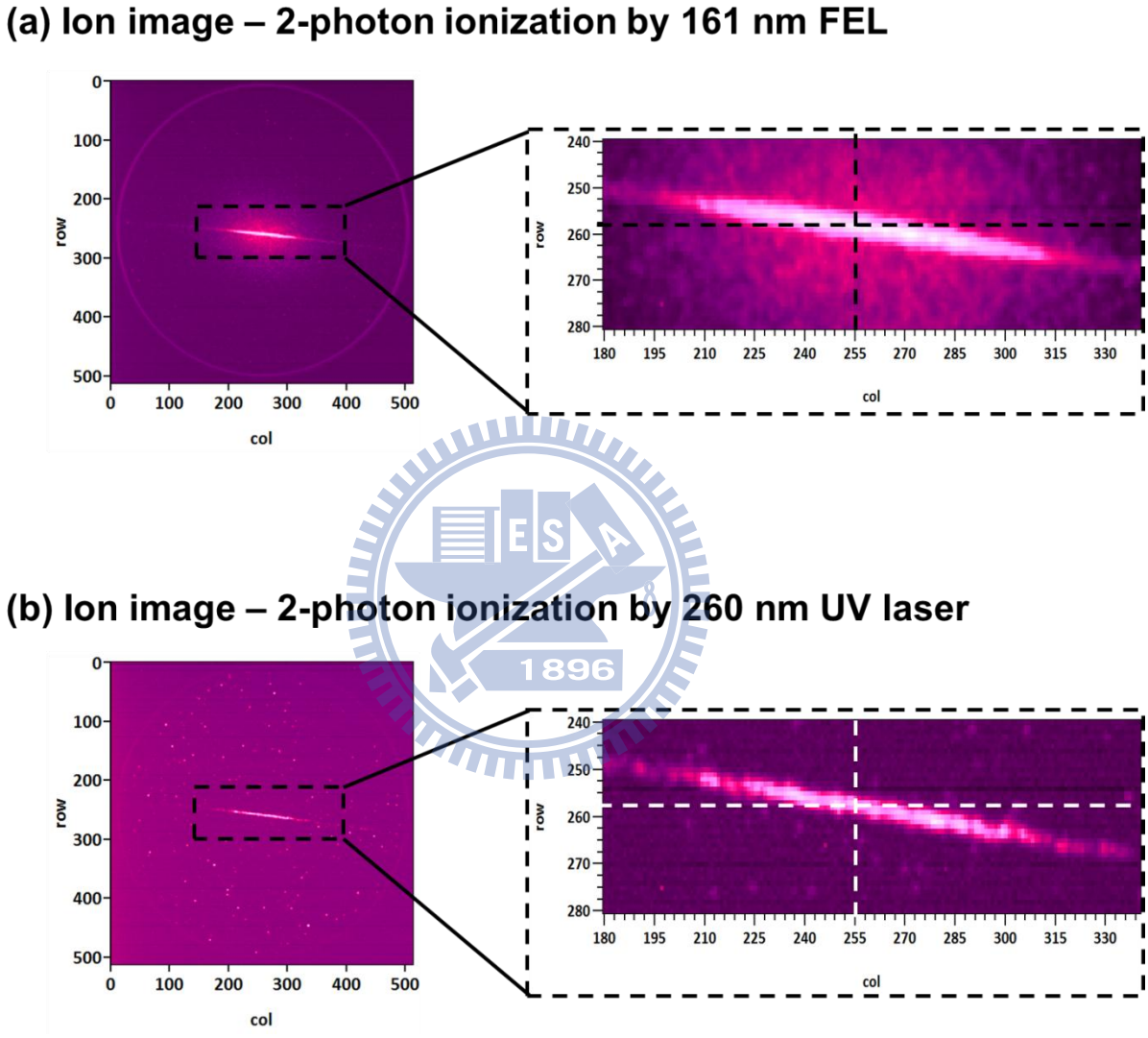

Figure 5.9 Ion image of 10% pyrazine seeded in He observed by: (a) FEL radiation; (b) UV radiation.

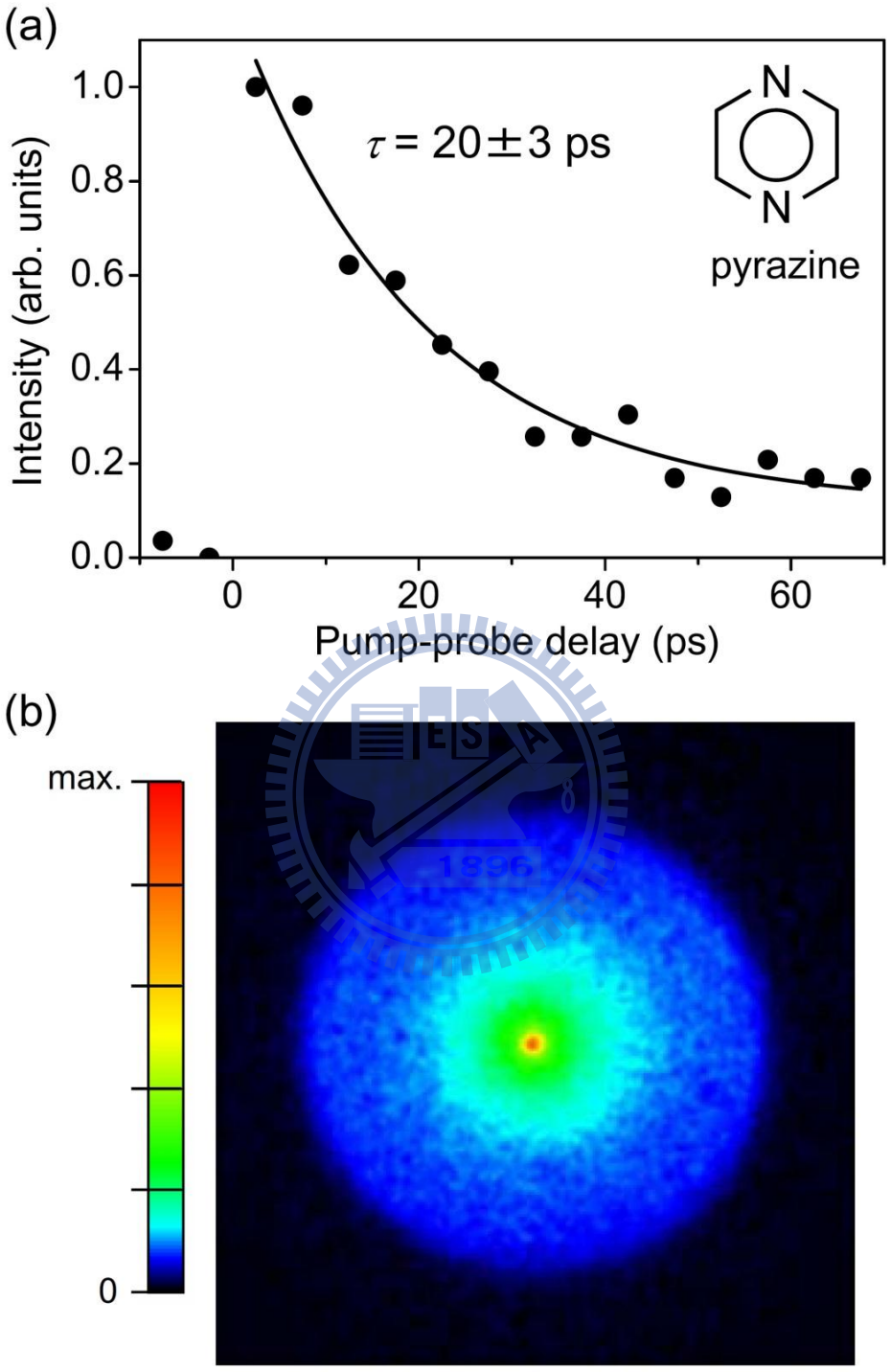

Figure 5.10 (a) (1+1') REMPI signal with 260-nm pump and 161-nm probe light. (a) Time profile of the pyrazine ion signal and least-squares fit of a single exponential decay curve. (b) Observed photoelectron image at the delay time of about 5 ps. A one-color background signal was already subtracted from the image.

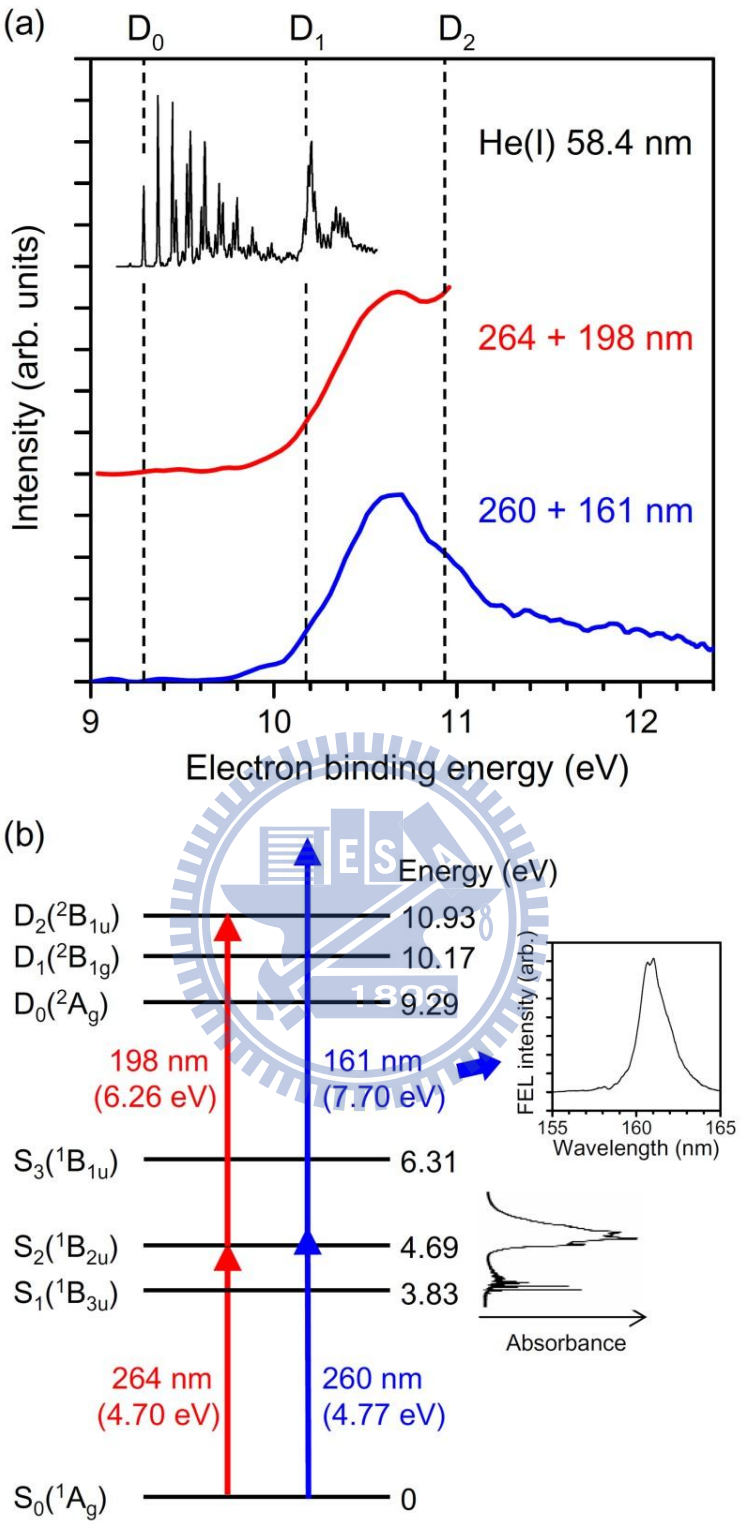

Figure 5.11 (a) Photoelectron kinetic energy distribution in He(I) photoelectron spectroscopy of the ground-state pyrazine (black) (ref. 37), 264-nm UV pump and 198-nm DUV probe experiment (red) (ref. 27) and 260-nm UV pump and 161-nm VUV probe (blue) (this work). (b) Schematic energy diagram of ionization process. UV absorption spectrum of pyrazine vapor at room temperature and time-spectrum of VUV FEL are shown as insets.

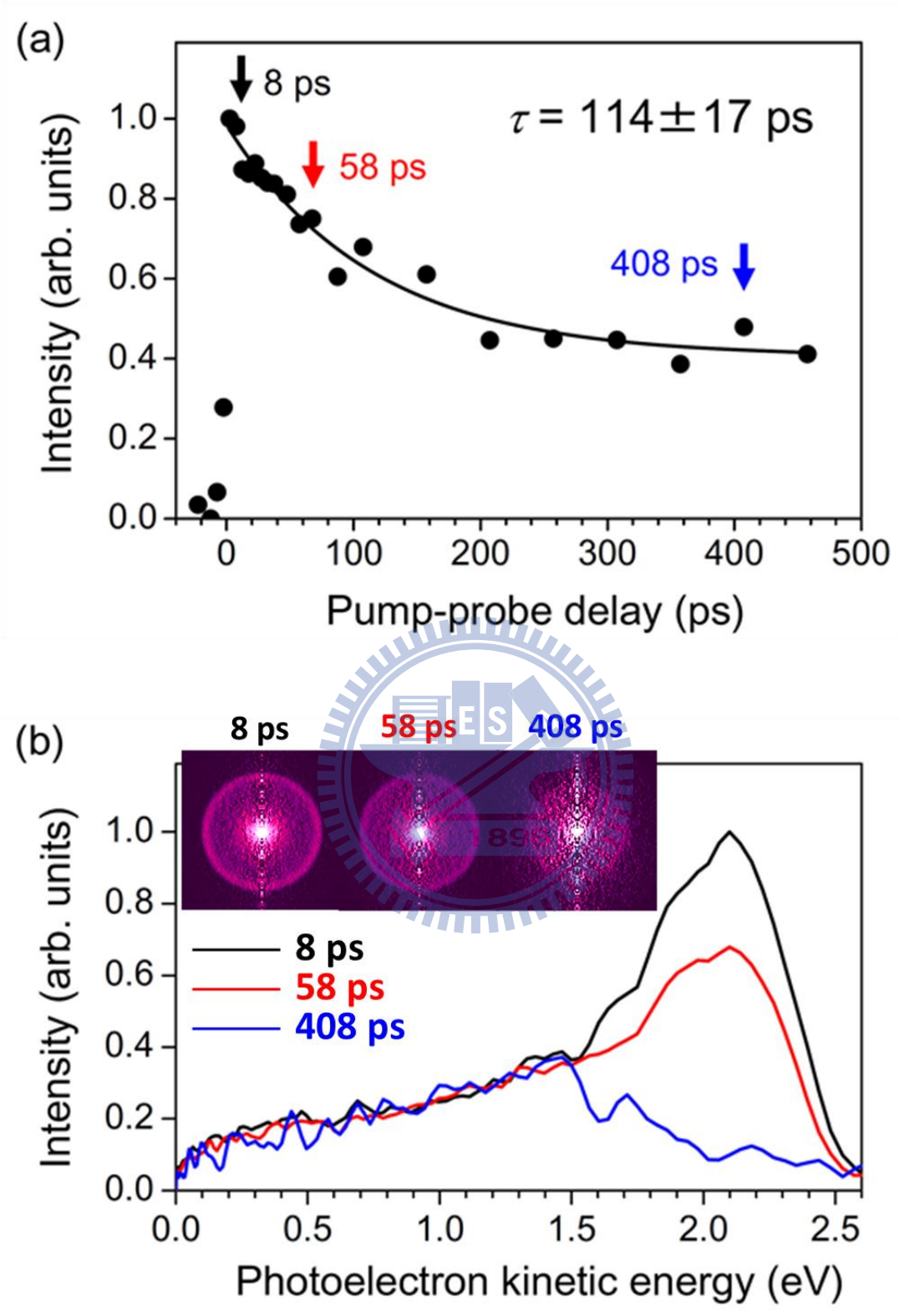

Figure 5.12 (a) (1+1') REMPI with 324-nm pump and 161-nm probe. (a) Time profile of pyrazine ion signal and least-squares fit of a single exponential decay curve. (b) Photoelectron kinetic energy distribution observed at various time delays. The inset shows the corresponding photoelectron (Abel-inverted) images.

5.5 References

[1] Zewail, A.H., *Science*, **1988**, *242*, 1645.

[2] Suzuki, T. *Annu. Rev. Phys. Chem.* **2006**, *57*, 555.

[3] Stolow, A.; Bragg, A. E.; Neumark, D. M. *Chem. Rev*. **2004**, *104*, 1719.

[4] Crespo-Hernandez, C. E. *et al. Chem. Rev*. **2004**, *104*, 1977.

[5] Samoylova, E. *et al. J. Am. Chem. Soc*. **2004**, *127*, 1782.

[6] Canuel, C. *et al. J. Chem. Phys*. **2005**, *122*, 074316.

[7] Farmanara, P. *et al. J. Chem. Phys*. **1999**, *111*, 6264.

[8] Meyer, M. *et al. Phys. Rev. A* **2006**, *74*, 011401.

[9] Radclife, P. *et al. Appl. Phys. Lett*. **2007**, *90*, 131108.

[10] Bostedt, C. *et al. Nucl. Instrum. Methods A* **2009**, *601*, 108.

[11] Azima, A. *et al. Appl. Phys. Lett*. **2009**, *94*, 144102.

[12] Johnsson *et al. J. Phys. B* **2009**, *42*, 134017.

[13] Tanaka, H. *et al*. *Proc. FEL* **2006**, 769-776.

[14] Shintake, T. *Nat. Photonics* **2008**, *2*, 555.

[15] Eppink, A. T. J. B.; Parker, D. H. *Rev. Sci. Instrum.* **1997**, *68*, 3477.

[16] Yamazaki, I. *et al. Faraday Discuss. Chem. Soc*. **1983**, *75*, 395.

[17] Schneider, R.; Domcke, W. *Chem. Phys. Lett*. **1988**, *150*, 235.

[18] Seidner, L. *et al. J. Chem. Phys*. **1992**, *96*, 5298.

[19] Woywod, C. *et al. J. Chem. Phys*. **1994**, *100*, 1400.

[20] Hahn, S.; Stock, G. *Phys. Chem. Chem. Phys*. **2001**, *3*, 2331.

[21] Suzuki, Y.; Stener, M.; Seideman, T. *J. Chem. Phys*. **2003**, *118*, 4432.

[22] Werner, U. *et al. Chem. Phys*. **2008**, *349*, 319.

[23] Stock, G.; Schneider, R.; Domcke, W.; *J. Chem. Phys.* **1989**, *90*, 7184.

[24] Seel, M.; Domcke, W. *J. Chem. Phys*. **1991**, *95*, 7806.

[25] Wang, L.; Kohguchi, H.; Suzuki, T. *Faraday Discuss*. **1999**, *113*, 37.

[26] Stert, V.; Farmanara, P.; Radloff, W. *J. Chem. Phys*. **2000**, *112*, 4460.

[27] Horio, T. *et al*. *J. Am. Chem. Soc*. **2009**, *131*, 10392.

[28] Suzuki, Y. *et al. J. Chem. Phys*. **2010**, *132*, 174302.

[29] Frad, A. *et al. J. Chem. Phys*. **1974**, *60*, 4419.

[30] Lahmani, F. *et al. J. Chem. Phys*. **1974**, *60*, 4431.

[31] McDonald, D. B.; Fleming, G. R.; Rice, S. A. *Chem. Phys*. **1981**, *60*, 335.

[32] Knee, J. L.; Doany, F. E.; Zewail, A. H. *J. Chem. Phys*. **1985**, *82*, 1042.

[33] Tsubouchi, M.; Whitaker, B. J.; Suzuki, T. *J. Phys. Chem. A* **2004**, *108*, 6823.

[34] Tsubouchi, M. *et al. Phys. Rev. Lett.* **2001**, *86*, 4500.

[35] Suzuki, T. Whitaker, B. *J. Int. Rev. Phys. Chem.* **2001**, *20*, 313.

[36] Walker, I. C.; Palmer, M. H. *Chem. Phys*. **1991**, *153*, 1669.

[37] Oku, M. *et al. J. Phys. Chem. A* **2008**, *112*, 2293.

Chapter 6

Summary

I have employed a photoelectron imaging (PEI) spectrometer with a He(I) light source to observe speed and angular distributions of photoelectrons. PEI experiment using He(I) radiation presented in this thesis is the first attempt reported so far. The challenge in coupling an incoherent VUV light source with PEI was to overcome the interference of the numerous background photoelectrons emitted from the instrument by scattered He(I) radiation. I have examined various designs of the acceleration electrodes experimentally and computationally and identified the major source of background photoemission to be from a repeller plate. Based on this finding, I designed a new electrostatic lens that places the repeller away from the ionization region and adds a retardation field to intercept background photoelectrons from the repeller toward the imaging detector. The resolution of PEI is enhanced by good spatial focusing of the electron trajectories starting from a finite ionization volume and also by high imaging resolution. As for the former, I used a number of electrodes behind the extractor plate to make the strength of the acceleration field varies more gradual than the simplest Eppink-Parker design using three electrodes. The energy resolution ($\Delta E/E$) better than 1 % was achieved even for a large ionization volume (i.e. of the order of millimeters). As for the latter, I used a super-resolution (4096 × 4096 pixels) imaging system developed in our laboratory (Chemical Dynamics Laboratory at RIKEN). Combining these two instruments, I obtained an energy resolution of 0.735 % at 5.461 eV (FWHM: 40 meV) with He(I) radiation. This does not represent the ultimate resolution achievable with the PEI spectrometer. It is possible to increase the resolution by one order of magnitude, if the photon beam can be more tightly focused. With the He(I) PEI spectrometer, I have measured the photoelectron image

of benzene and pyridine in supersonic molecular beams. In these experiments, time-gated measurement with a pulsed beam provided a high signal contrast with respect to the background photoionization signal from residual water vapor in the ionization chamber. On the other hand, the ultimate imaging resolution with centroiding calculation is not obtainable at the high signal count rate of He(I) PEI owing to spatial overlap between the light spots of two electron impacts on the detector. A camera with a higher frame-rate and a more rapid digital image processing would overcome this problem. The photoelectron anisotropy parameters determined for benzene and pyridine are in good agreement with the literature values. The anisotropy parameters of photoelectrons from pyridine are first reported for the electron binding energies over 14 eV.

The PEI spectrometer developed for He(I) radiation is also applicable to photoelectron spectroscopy with other vacuum ultraviolet (VUV) sources such as synchrotron radiation, free electron laser (FEL) and high harmonics of the output from ultrashort pulsed lasers. I demonstrated that a VUV or EUV laser is useful for pump–probe photoelectron spectroscopy to observe ultrafast electronic dynamics. Time-resolved photoelectron imaging using a tunable femtosecond ultraviolet laser and a vacuum UV free-electron laser is performed. Ultrafast intersystem crossing on S_1 to T_1 and internal conversion from S_1 to S_0 in pyrazine in a supersonic molecular beam were clearly observed in the temporal profiles of photoelectron intensity and photoelectron images. The VUV radiation allowed us to observe the entire Franck-Condon envelope in photoionization from a transient electronic state; this was not possible with UV-UV two-color experiment in the laboratory. This study clearly demonstrated exciting opportunities made possible with a SASE FEL and a tunable UV femtosecond laser for picosecond TR-PEI experiment on photoinduced chemical dynamics of large polyatomic molecules. On the other hand, the energy resolution of PEI was higher with He(I) radiation than VUV-FEL radiation at 58.4 nm, which is ascribed to large effective bandwidth (0.1 eV) of the laser radiation from SASE FEL.